MEASUREMENTS OF DYNAMIC PROPERTIES OF MATERIALS

Volume III

6061-T6 ALUMINUM

FINAL REPORT

by

D. R. Christman
W. M. Isbell
S. G. Babcock
A. R. McMillan
S. J. Green

Materials and Structures Laboratory
Manufacturing Development, General Motors Corporation
General Motors Technical Center, Warren, Michigan 48090

UNCLASSIFIED
Security Classification

DOCUMENT CONTROL DATA - R & D

(Security classification of title, body of abstract and indexing annotation must be entered when the overall report is classified)

1. ORIGINATING ACTIVITY *(Corporate author)*: Manufacturing Development, General Motors Corporation, General Motors Technical Center, Warren, Michigan 48093

2a. REPORT SECURITY CLASSIFICATION: UNCLASSIFIED

2b. GROUP:

3. REPORT TITLE

Final Report Measurements of Dynamic Properties of Materials Volume III: 6061-T6 Aluminum

4. DESCRIPTIVE NOTES *(Type of report and inclusive dates)*

Final Report (in Six Volumes)

5. AUTHOR(S) *(First name, middle initial, last name)*

Douglas R. Christman, William M. Isbell, Stephen G. Babcock, Allen R. McMillan, Sidney J. Green

6. REPORT DATE	7a. TOTAL NO. OF PAGES	7b. NO. OF REFS
1971 November	156	98

8a. CONTRACT OR GRANT NO.	9a. ORIGINATOR'S REPORT NUMBER(S)
DASA-01-68-C-0114	
b. PROJECT NO. NWER XAXA	MSL-70-23, Vol. III
c. Task & Subtask-A106	9b. OTHER REPORT NO(S) *(Any other numbers that may be assigned this report)*
d. Work Unit-07	DASA-2501-3

10. DISTRIBUTION STATEMENT

Approved for public release; distribution unlimited.

11. SUPPLEMENTARY NOTES	12. SPONSORING MILITARY ACTIVITY
	Director Defense Nuclear Agency Washington, D. C. 20305

13. ABSTRACT

Results of an experimental study on the dynamic properties of 6061-T6 aluminum are presented. Areas studied included stress-strain-strain rate and reverse loading behavior, elastic constants, equation of state, compressive and release wave characteristics, and spall fracture. The material showed approximately elastic-perfectly plastic behavior under uniaxial stress compression (0.005 to 1000/sec strain rates). Strain-rate sensitivity was very low at 20°C, but increased at temperatures of 150, 204, and 288°C. Longitudinal and shear wave velocities at 20°C were 6.368 and 3.197 mm/μsec, and temperature and pressure dependence was also measured and various elastic constants were calculated. The shock wave equation of state (EOS) up to 200 kbar was determined as $\sigma_H = 1.0 + 140.4u_p + 37.7u_p^2$. The EOS was also calculated from the elastic constants and comparisons made with the shock wave EOS. Compressive wave tests showed a well-defined elastic precursor with a steady-state value of ~5 kbar. The yield level from shock wave profile measurements was approximately the same as that determined from uniaxial stress and EOS tests. The impact velocity required for spall fracture was found to increase with decreasing pulse width, and to decrease with increasing temperature.

DD FORM 1 NOV 65 1473

UNCLASSIFIED
Security Classification

14. KEY WORDS	LINK A		LINK B		LINK C	
	ROLE	WT	ROLE	WT	ROLE	WT
Stress-strain-strain rate Reverse loading behavior Elastic constants Equation of state Compressive and release wave characteristics Spall fracture						

DASA 2501 -3
MSL-70-23 Vol.III
1971, NOVEMBER

MEASUREMENTS OF DYNAMIC PROPERTIES OF MATERIALS

Volume III

6061-T6 ALUMINUM

FINAL REPORT

" This work was supported by the Defense Nuclear Agency under NWER Subtask AA 106-07"

by

D. R. Christman
W. M. Isbell *
S. G. Babcock
A. R. McMillan
S. J. Green†

Materials and Structures Laboratory
Manufacturing Development, General Motors Corporation
General Motors Technical Center, Warren, Michigan 48090

* Presently with Lawrence Livermore Laboratory, Livermore, California
† Presently with Terra Tek. Inc. 815 East 4th. South, Salt Lake City, Utah 48102

Prepared For

HEADQUARTERS
Defense Nuclear Agency
Washington, D.C. 20305

Under Contract DASA01-68-C-0114

COPY No.____

ABSTRACT

Results of an experimental study on the dynamic properties of 6061-T6 aluminum are presented. Areas studied included stress-strain-strain rate and reverse loading behavior, elastic constants, equation of state, compressive and release wave characteristics, and spall fracture. The material showed approximately elastic-perfectly plastic behavior under uniaxial stress compression (0.005 to 1000/sec strain rates). Strain-rate sensitivity was very low at 20°C, but increased at temperatures of 150, 204, and 288°C. Longitudinal and shear wave velocities at 20°C were 6.368 and 3.197 mm/μsec, and temperature and pressure dependence was also measured and various elastic constants were calculated. The shock wave equation of state (EOS) up to 200 kbar was determined as $\sigma_H = 1.0 + 140.4\ u_p + 37.7\ u_p^2$. The EOS was also calculated from the elastic constants and comparisons made with the shock wave EOS. Compressive wave tests showed a well-defined elastic precursor with a steady-state value of $\sim$ 5 kbar. The yield level from shock wave profile measurements was approximately the same as that determined from uniaxial stress and EOS tests. The impact velocity required for spall fracture was found to increase with decreasing pulse width, and to decrease with increasing temperature.

FOREWORD

The prediction of reentry vehicle response to impulsive loading resulting from energy deposition has been studied extensively during the last decade. Analytical models and computer routines have been developed to assess the vulnerability of such vehicles to the initial loading phase, in which stress waves are generated and propagated through the structure, and to subsequent phases, where elastic vibration, plastic deformation and/or fracture may occur.

A Defense Atomic Support Agency (DASA) program was initiated with the objective of improving computer codes for the prediction of damage induced by X-rays (PREDIX). The PREDIX metals program has combined the efforts of several contractors under the direction of DASA. The primary contributions of each contractor can be summarized as follows:

General Motors Corporation--Measurement of material properties, including stress-strain-strain rate behavior, elastic constants, equations of state, shock wave profiles and spall fracture.

Effects Technology Inc.--Spall fracture tests and analysis (exploding foil) and underground testing.

KMS Technology Center--Constitutive modeling.

Physics International Company--Energy deposition and spall fracture studies (electron beam).

Systems, Science and Software--Energy deposition and front surface phenomena, constitutive modeling and code development, and underground testing.

TABLE OF CONTENTS

TABLE OF CONTENTS (Continued)

LIST OF ILLUSTRATIONS

LIST OF ILLUSTRATIONS (Continued)

LIST OF ILLUSTRATIONS (Continued)

LIST OF TABLES

LIST OF SYMBOLS

C_B	Bulk Wave Velocity, mm/μsec
C_L	Longitudinal Wave Velocity, mm/μsec
C_S	Shear Wave Velocity, mm/μsec
c_p	Specific Heat, cal/g
G	Shear Modulus, kbar
K	Bulk Modulus, kbar
P_H	Mean Pressure, Hydrostat, kbar
P_S	Mean Pressure, Adiabat, kbar
P_T	Mean Pressure, Isotherm, kbar
T	Temperature, °C
U_S	Shock Wave Velocity, mm/μsec
u_p	Particle Velocity, mm/μsec
v	Specific Volume, cc/g
V_I	Impact Velocity, mm/μsec
X	Target Thickness, mm
X_O	Impactor Thickness, mm
X^S	Adiabatic Modulus, kbar
X^T	Isothermal Modulus, kbar
$X_{OS}^{S'}$, $X_{OS}^{T'}$	Adiabatic Pressure Derivative @ Zero Pressure $\left(= \left(\frac{\partial X^S}{\partial P}\right)_S \Big|_{P=O} \right)$
$X_{OT}^{T'}$, $X_{OT}^{S'}$	Isothermal Pressure Derivative @ Zero Pressure $\left(= \left(\frac{\partial X^T}{\partial P}\right)_T \Big|_{P=O} \right)$
β	Volume Coefficient of Expansion, /°C $= -\frac{1}{\rho}\left(\frac{\partial \rho}{\partial T}\right)_{P=O}$
γ	Gruneisen Parameter
μ	Compression $(= v_o/v - 1)$
ν	Poisson's Ratio
ρ	Density, g/cc
σ_H	Stress, Hugoniot, kbar

(Page xii is Blank)

MSL-70-23, Vol. III

INTRODUCTION

This report is one of a series of six giving results of a study of dynamic properties of four metals. The principle objectives of this study were:

- Provide measurements of dynamic properties of materials to be used as inputs to model development for shock wave propagation and dynamic fracture.
- Provide data to establish accuracy of computer code predictions.
- Provide physical interpretation of experimentally observed material response to dynamic test conditions.

The primary areas studied included: (1) Stress-strain-strain rate behavior in uniaxial stress, including Bauschinger effect; (2) Elastic constants, including temperature and pressure dependence; (3) Hugoniot equation of state; (4) Compressive and release wave profiles, including elastic precursor decay and wave attenuation; and (5) Spall fracture studies, including pulse width dependence. The six reports in this series are:

Vol. I: Summary of Results, DASA 2501-1 (AD712847)
Vol. II: Experimental Methods and Techniques, DASA 2501-2
Vol. III: 6061-T6 Aluminum, DASA 2501-3
Vol. IV: Alpha Titanium, DASA 2501-4
Vol. V: OFHC Copper, DASA 2501-5
Vol. VI: Tantalum, DASA 2501-6

The experimental techniques utilized in this study are reviewed in Vol. II (DASA 2501-2). Briefly, the principal techniques applied were:

Stress-strain Studies--A laboratory-type universal testing machine was used for rates < 0.1/sec, a medium strain rate machine for rates of 10^{-3}/sec to 10^{2}/sec, and a Hopkinson bar device for rates of about 10^{2} to 5 X 10^{3}/sec.

Elastic Constants--The pulse superposition method was used for measuring longitudinal and shear wave velocities as functions of temperature and hydrostatic pressure.

Equation of State--Gun-launched, flat-plate impact techniques were used to generate uniaxial strain conditions. Velocities up to 0.6 mm/μsec were achieved with 63.5 mm and 102 mm single-stage compressed-gas guns, and velocities of 0.3 to 2 mm/μsec were achieved with a 64 mm single-stage powder gun. Hugoniot data were obtained with x-cut quartz gage and streak camera techniques.

Wave Propagation and Spall Fracture--Flat-plate impact techniques were also used. Wave profiles were measured with x-cut quartz gages and a laser velocity interferometer.

A literature search on dynamic properties of materials was carried out under the PREDIX program and a listing of recent publications (including abstracts) on dynamic properties of materials is given in Reference 1.

SECTION I

MATERIAL PROPERTIES

Aluminum has a face-centered-cubic structure and the 6061 type on which the tests discussed in this report were carried out is a heat-treatable wrought alloy. This material has nominally 3% alloying constituents (primarily magnesium, silicon and iron) and results of chemical analysis are given in Table I. The alloy is solution-heat-treated and precipitation-hardened to the '-T6' temper, as outlined in Table I. The material was purchased as sheet and plate stock in thicknesses of 1.6, 3.2, 6.4, 12.7 and 50.8 mm. Although all material was ordered to the same specifications, there were slight differences in yield and flow stress behavior for the different thicknesses. Hardness of the various thicknesses was:

Thickness (mm)	Measured R_B	Estimated Bhn (500 kg)
1.6	∿ 50	83
3.2	51	84
6.4	57	91
12.7	59	94
50.8	59	94

All stock thicknesses showed the same degree of grain structuring, although there was some variation in grain size with the thinner stock having smaller grains. Photomicrographs showing the grain structure in the 3.2 mm and 12.7 mm stock are shown in Figure 1.

TABLE I

6061 ALUMINUM CHARACTERISTICS

COMPOSITION (WEIGHT %):

Element	Maximum (Ref. 2)	Measured (12.7 mm Plate)
Silicon	0.80	0.63
Iron	0.70	0.41
Copper	0.40	0.20
Manganese	0.15	0.06
Magnesium	1.20	0.84
Zinc	0.25	0.09
Chromium	0.35	0.20
Titanium	0.15	0.06

PROCESSING (REF. 2):

A. SOLUTION HEAT TREATMENT, -T4 TEMPER

1. 970°F for 0.2-1 hours in molten salt.

2. Quench in cold water with minimum delay.

B. PRECIPITATION HEAT TREATMENT, -T6 TEMPER

1. 350°F for 6-10 hours.

2. Cooling rate unimportant (not too slow).

C. STRESS-RELIEVED BY STRETCHING, -T651 TEMPER (OPTIONAL)

1. 1 1/2-3% permanent set after B.

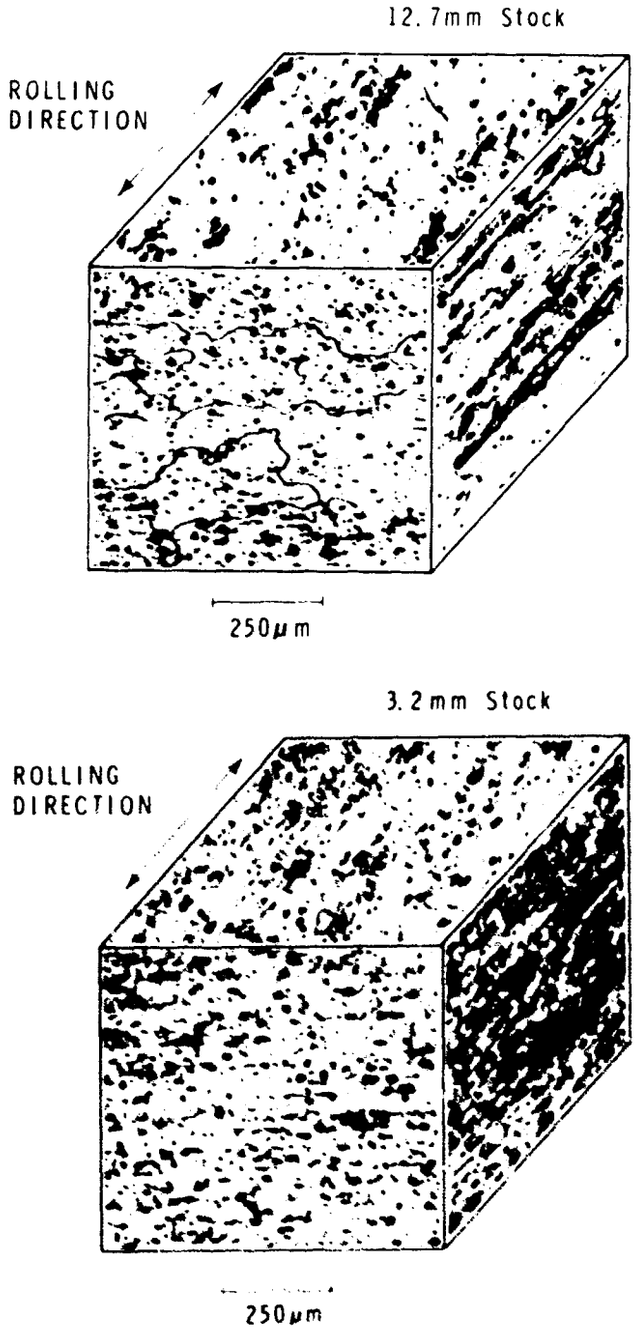

Figure 1 6061-T6 Aluminum, As-Received Material

The average measured density was 2.703 g/cc (0.0976 lb/in^3). For use in equation of state and energy deposition calculations, several physical constants were compiled from the literature[3-7] and are listed below:

Volume coefficient of thermal expansion, β:

$$67.0 \times 10^{-6} + 0.06 \times 10^{-6} \; T \; /°C$$

Specific heat, c_p:

$$0.220 + 0.00015 \times T \; cal/g-°C$$

Solidus temperature: 616°C

Liquidus temperature: 651°C

Boiling temperature: ∿ 2450°C

Latent heat of fusion: ∿ 93 cal/g

Latent heat of vaporization: ∿ 2510 cal/g

(T in °C)

No change in the microstructure of 6061-T6 aluminum was observed for shock stresses up to 30 kbar, i.e., there was no visual evidence of twinning or grain deformation. Photomicrographs of as-received and shocked material are compared in Figure 2.

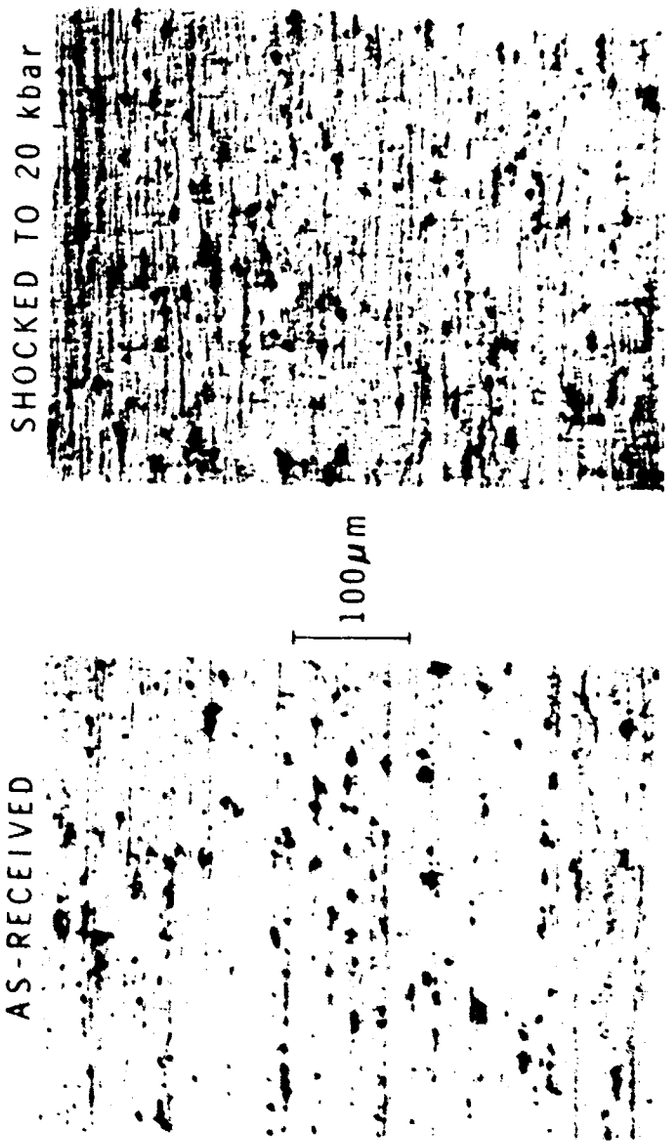

Figure 2 6061-T6 Aluminum, As-Received and Shocked Material

SECTION II

STRESS-STRAIN STUDIES

Shock wave and structural response code input requirements include constitutive equations relating stress to strain, strain rate and temperature. To obtain these, measurements are made of uniaxial compressive stress vs. strain at various strain rates and temperatures. These tests give yield and flow stress behavior, strain rate sensitivity and work hardening characteristics. Although it is recognized that heating rate and time-at-temperature, as well as final temperature, are important in assessing material properties under short-time ($< 10^{-6}$ sec) energy deposition conditions, most stress-strain data reported here are for relatively long heating times only. Bauchinger effect tests were conducted to provide information on unloading and subsequent yield.

UNIAXIAL STRESS TESTS

Results of compressive stress-strain tests on 6061-T6 are shown in Figures 3 and 4 for strain rates of 0.005/sec to 10^3/sec and test temperatures of 20° to 288°C, with each curve the average of several tests. At 20°C, strain rate sensitivity is negligible (within normal material scatter and test errors), but increasing the temperature above 150°C results in an increase in rate sensitivity. Yield stress and work hardening decrease with increasing temperature.

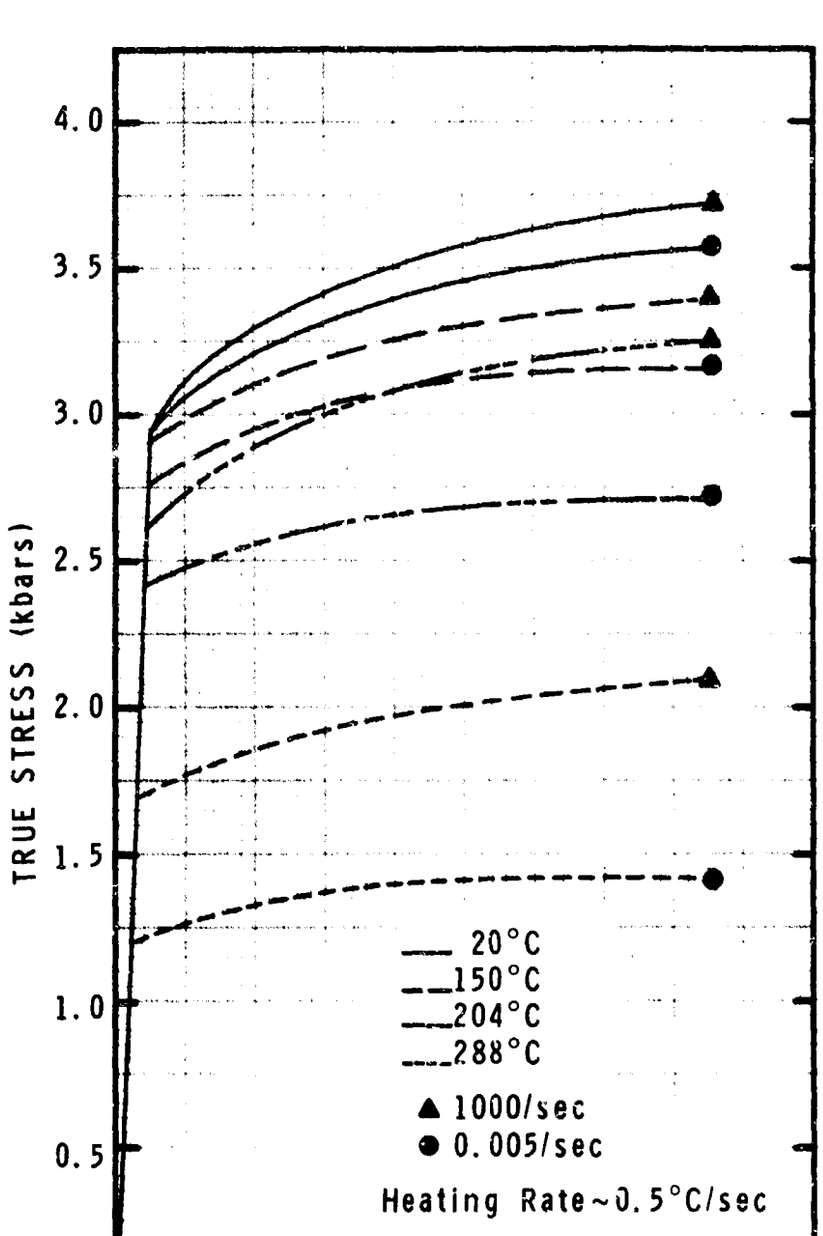

Figure 3 Compressive Stress vs. Strain, 6061

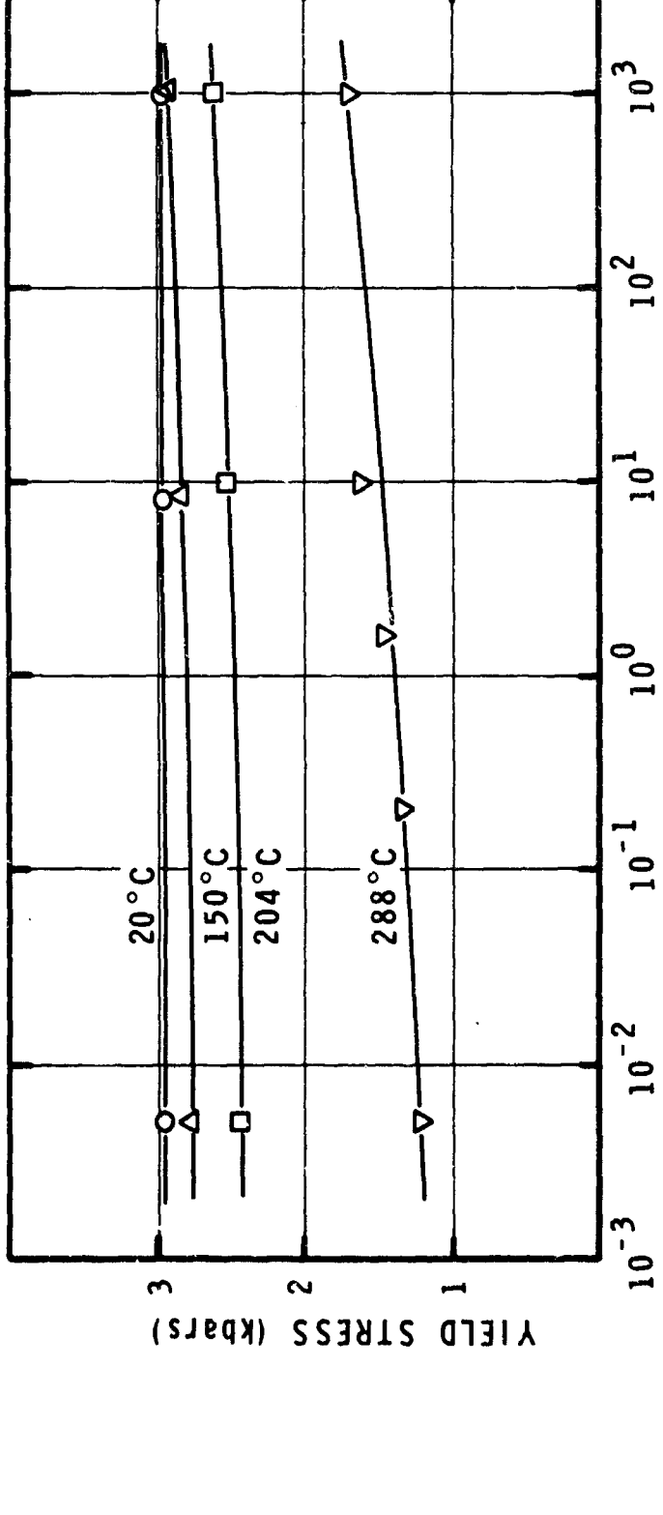

Figure 4 Compressive Yield Stress vs. Log Strain Rate, 6061

The temperature data in Figures 3 and 4 were obtained for a heating rate of ~ 0.5°C/sec and it has been found that yield and flow stress at elevated temperatures are a function of heating rate and time-at-temperature.[8] For example, the tensile yield stress in 6061-T651 is shown in Figure 5 as a function of heating rate for two final temperatures. The data indicate that degradation of yield at elevated temperature has three distinct regimes. At high heating rates (> 1°C/sec for 260°C) the yield shows little dependence on heating rate, suggesting an almost instantaneous decrease in yield as temperature increases. At intermediate rates (10^{-4} to 1°C/sec) a time-dependent softening occurs and the yield decreases with decreasing heating rate due to overageing or precipitate coarsening. At low heating rates (< 10^{-4}°C/sec) the yield reaches a constant value. Although the data in Figure 5 are presented in terms of heating rate, the conclusions would be qualitatively the same if discussed as a function of time-at-temperature. All tests were performed at constant strain rate and the observed response may be rate dependent.

There was a slight variation in yield and flow stress for test specimens taken from stock of different thicknesses, as shown in Figure 6. This variation is comparable to that due to scatter from one plate alone and to rate sensitivity at 20°C.

REVERSE LOADING TESTS

The reverse loading behavior or Bauschinger effect* was studied by performing uniaxial tensile stress tests after the material had been prestrained in the opposite (compressive) sense.

* The Bauschinger effect can be defined as the reduction in stress at a given strain in the reverse direction compared to that in the original loading direction.

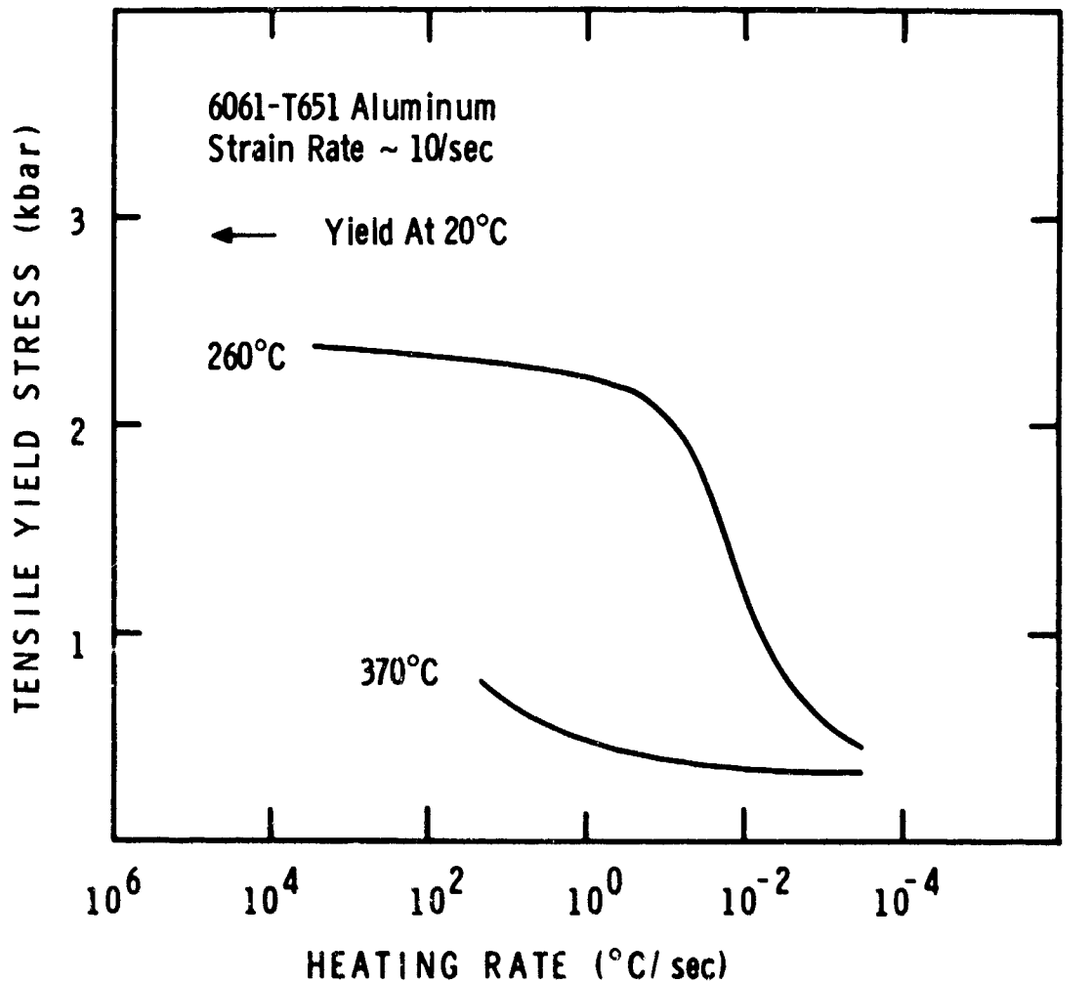

Figure 5 Tensile Yield Stress vs. Log Heating Rate, 6061

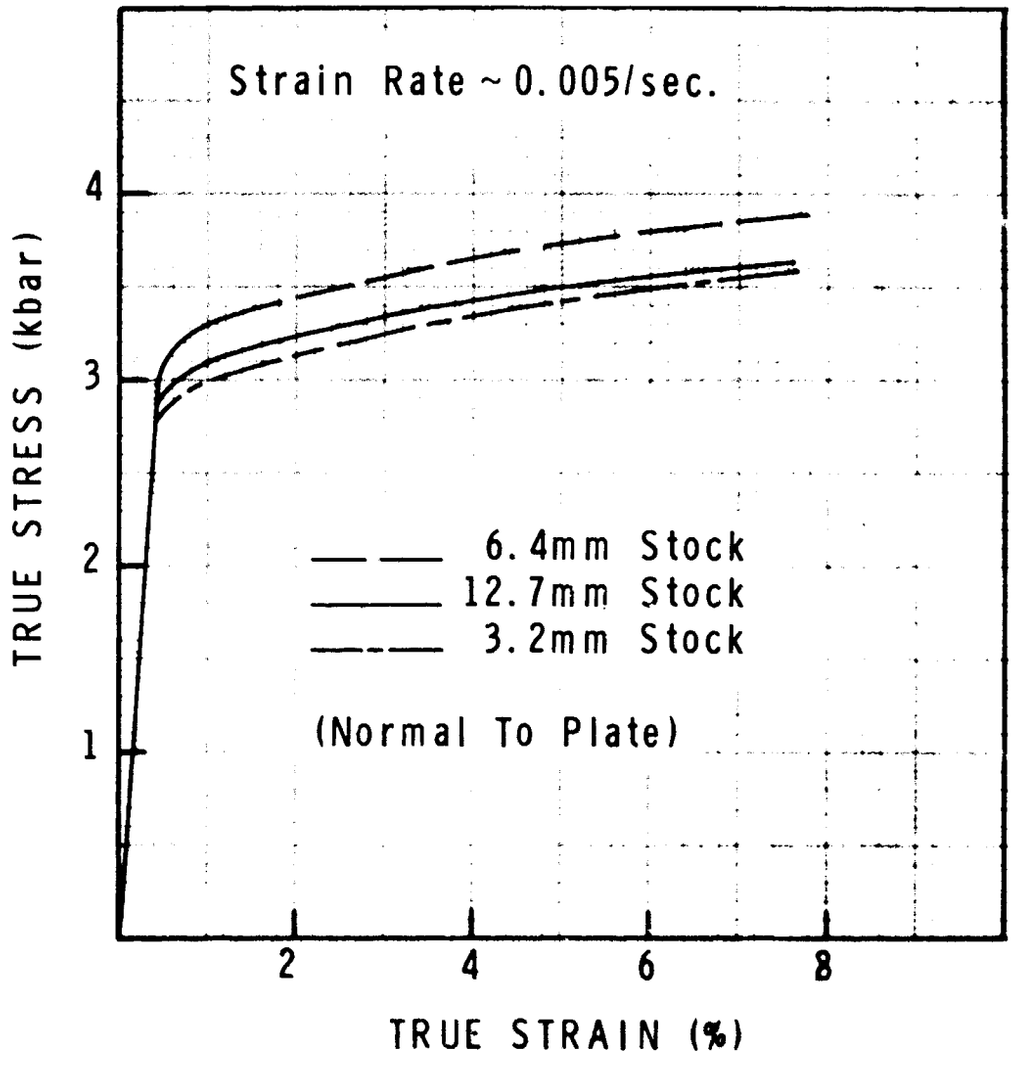

Figure 6 Compressive Stress vs. Strain, Material Effect, 6061-T6

Specimens were loaded in compression to strains of 0.5 to 3.0%, unloaded to zero stress, and then immediately loaded in tension. The Bauschinger effect can be evaluated in terms of the ratio of yield stress in tension (reload) to the yield stress in compression or to the maximum preload stress. Care must be taken in interpreting data from tests where small (< 0.2%) values of strain are measured. Choosing a definition such as the first deviation from a linear elastic behavior, or stress at a given offset strain, will result in various interpretations of the Bauschinger effect. Reverse loading test results are shown in Figure 7 and the data is cross-plotted in Figure 8 where two definitions of the Bauschinger effect are plotted against plastic prestrain.

Following Milligan, Koo and Davidson[9], a Bauschinger effect factor (BEF) can be defined in two ways:

(1) The ratio of yield stress upon reverse loading to the initial yield stress (see Figure 8 for symbol definition)

$$BEF = \frac{\sigma_C}{\sigma_A}$$

(2) The ratio of yield stress during reloading to the maximum stress upon loading

$$BEF = \frac{\sigma_C}{\sigma_B}$$

This latter definition takes into account strain hardening. All stresses were defined at a 0.1% offset strain. From Figure 8 it appears that the Bauschinger effect factor decreases (Bauschinger effect increases) up to about

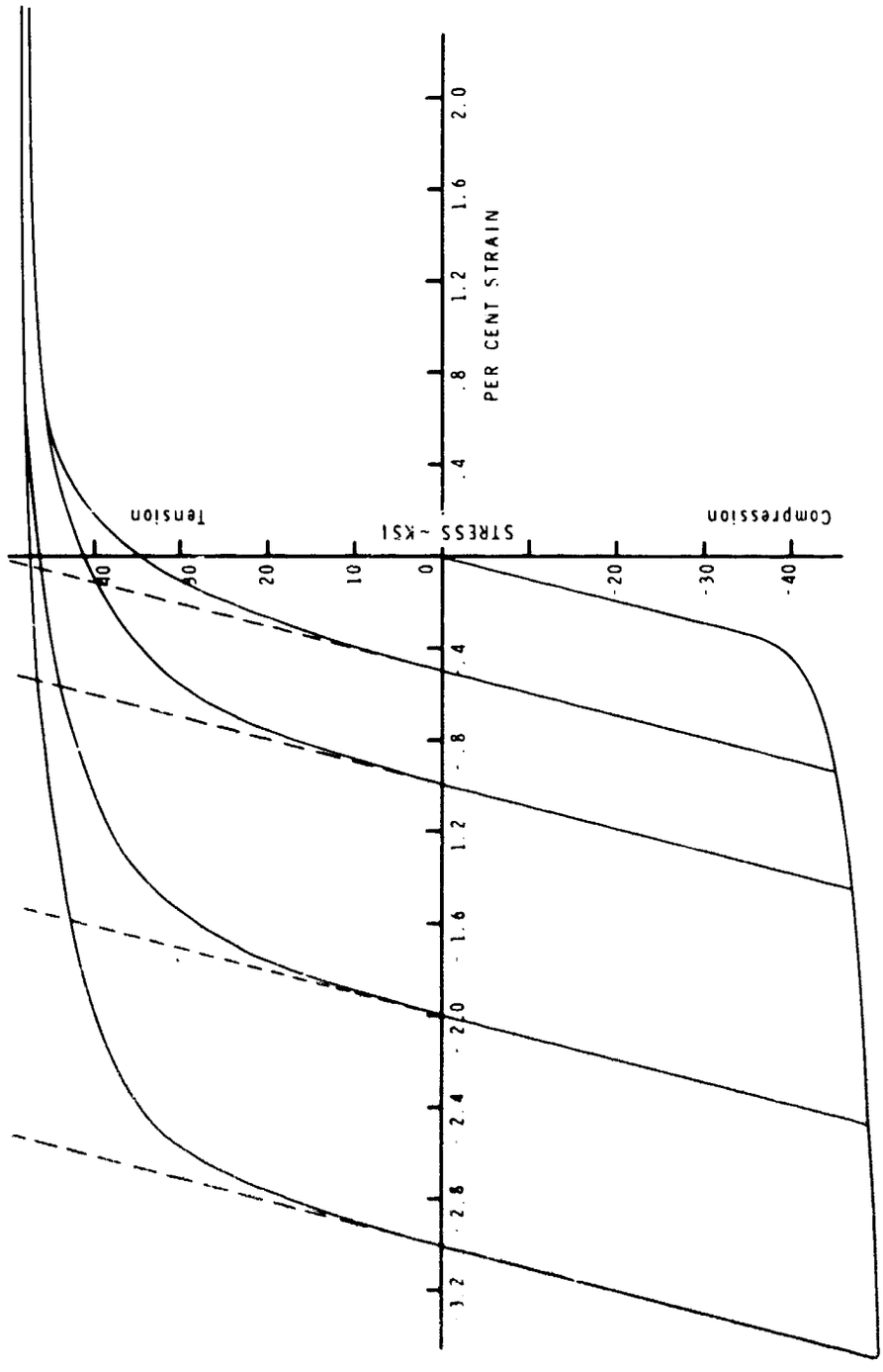

Figure 7 Reverse Loading Behavior, 6061-T6

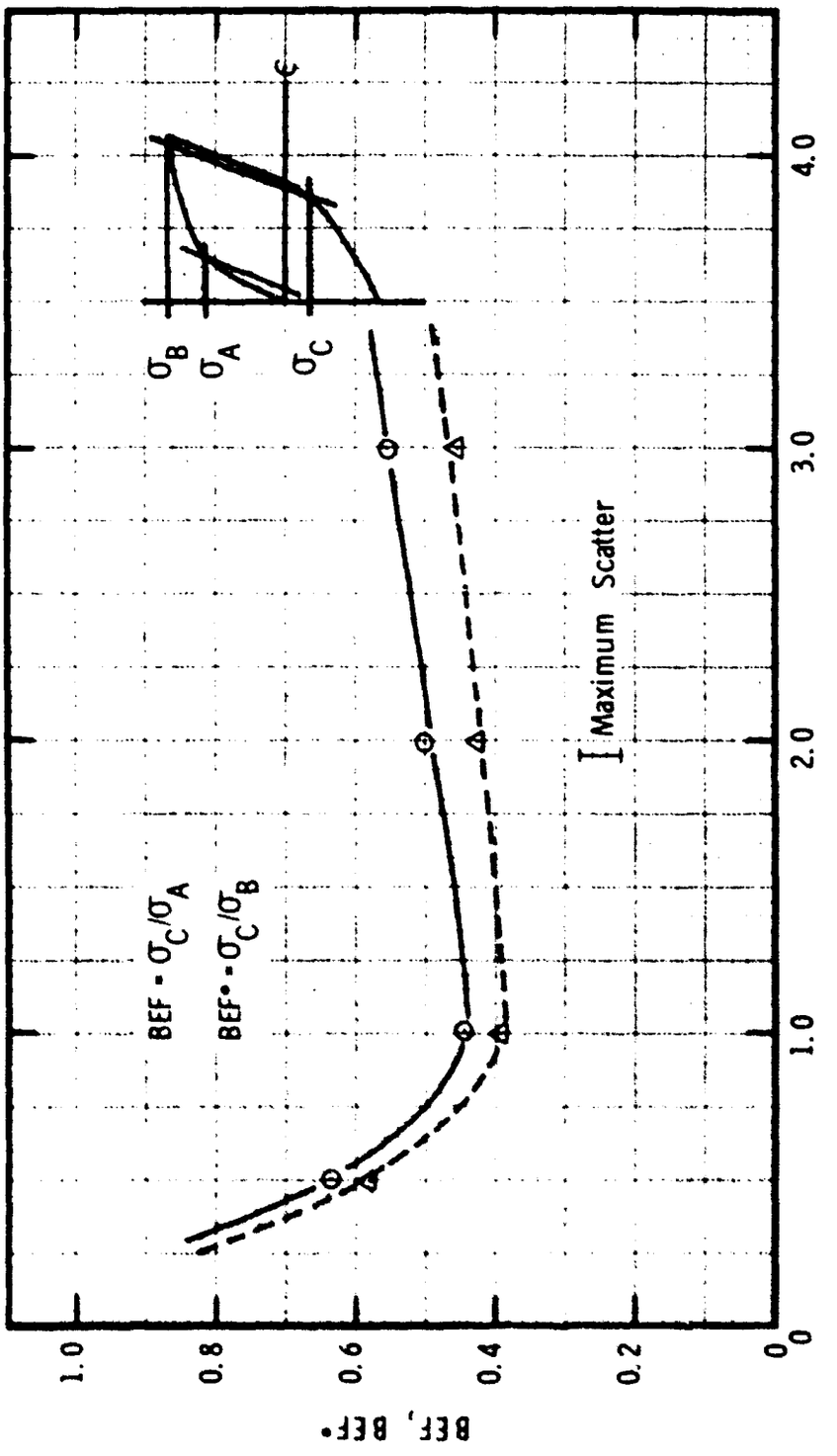

Figure 8 Bauschinger Effect Data, 6061-T6

1.0 - 1.5% plastic strain. Then, with increasing prestrain, the BEF from both definitions appears to increase in magnitude. These results are quantitatively similar to the results on 6061-T6 plate-stock aluminum[10] and modified high-strength steel[9] reported by Milligan, et al., although the preload was in tension rather than compression. The probable cause for the increase in BEF after reaching a minimum at low strains has been attributed to strain-hardening effects.[10,11] Figure 9 shows results from a set of cyclic compression-tension tests on 6061-T6 aluminum. The primary conclusion to be drawn from this data is the type of hardening mechanism for this material. At a strain of approximately 0.5%, kinematic hardening predominates.[8]

BIAXIAL STRESS TESTS

Tubular specimens machined from 6061-T6 bar stock were tested under biaxial stress conditions to determine the yield locus (or surface). A 0.25% strain offset technique in the octahedral shear stress-strain plane was used to determine yield. Results are given in Figure 10 and show that both the von Mises and the Tresca yield theories provide reasonable fits to the data.

(Stress-strain tests of 6061-T6 have been conducted under a number of other programs at General Motors Corporation. The reader is referred to previously published reports and papers for additional details in such areas as uniaxial stress testing[12-14], biaxial stress testing[8,15,16], heating rate effects[8,17,18], and preshocking and prestraining effects[19].)

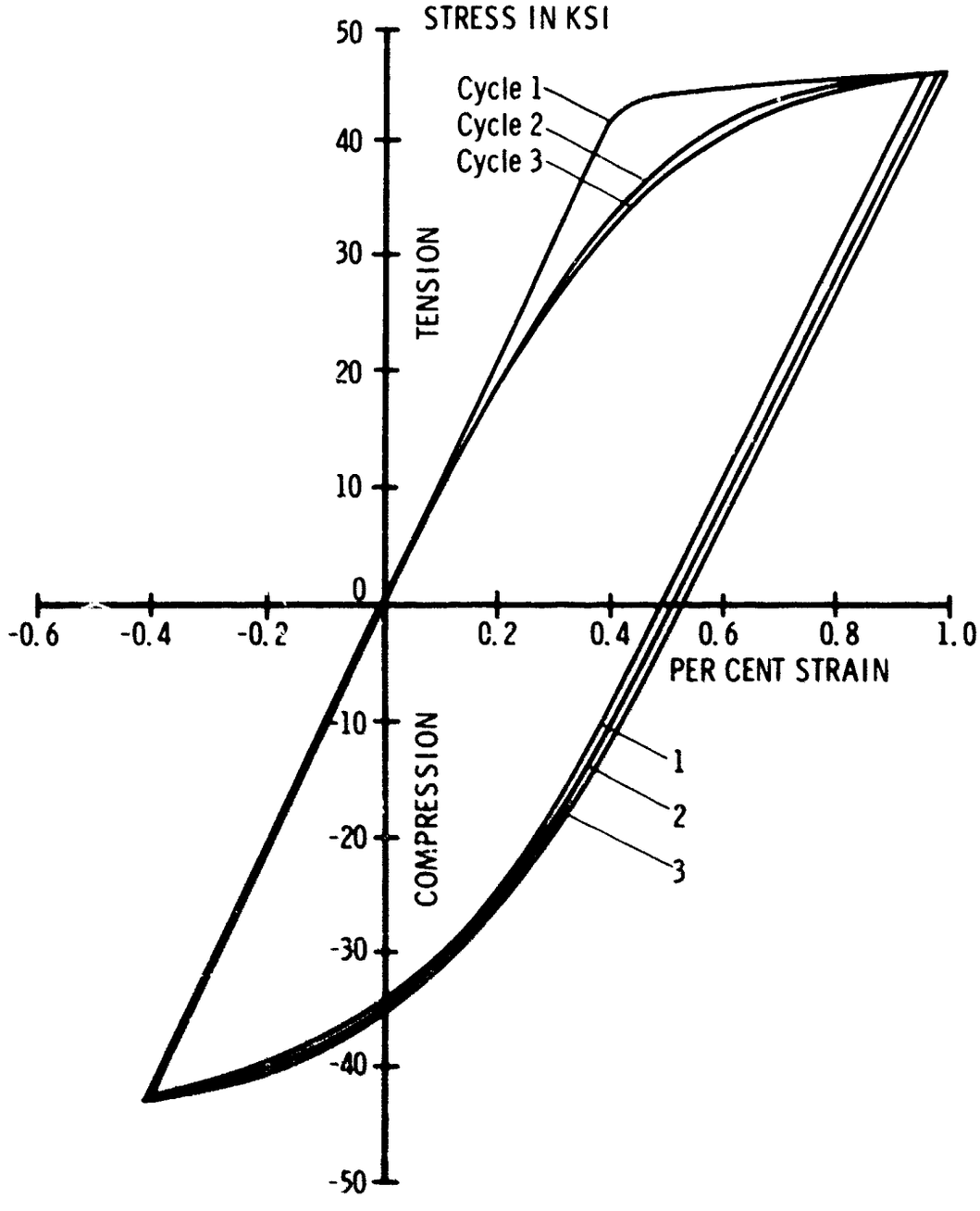

Figure 9 Cyclic Loading Behavior, 6061-T6

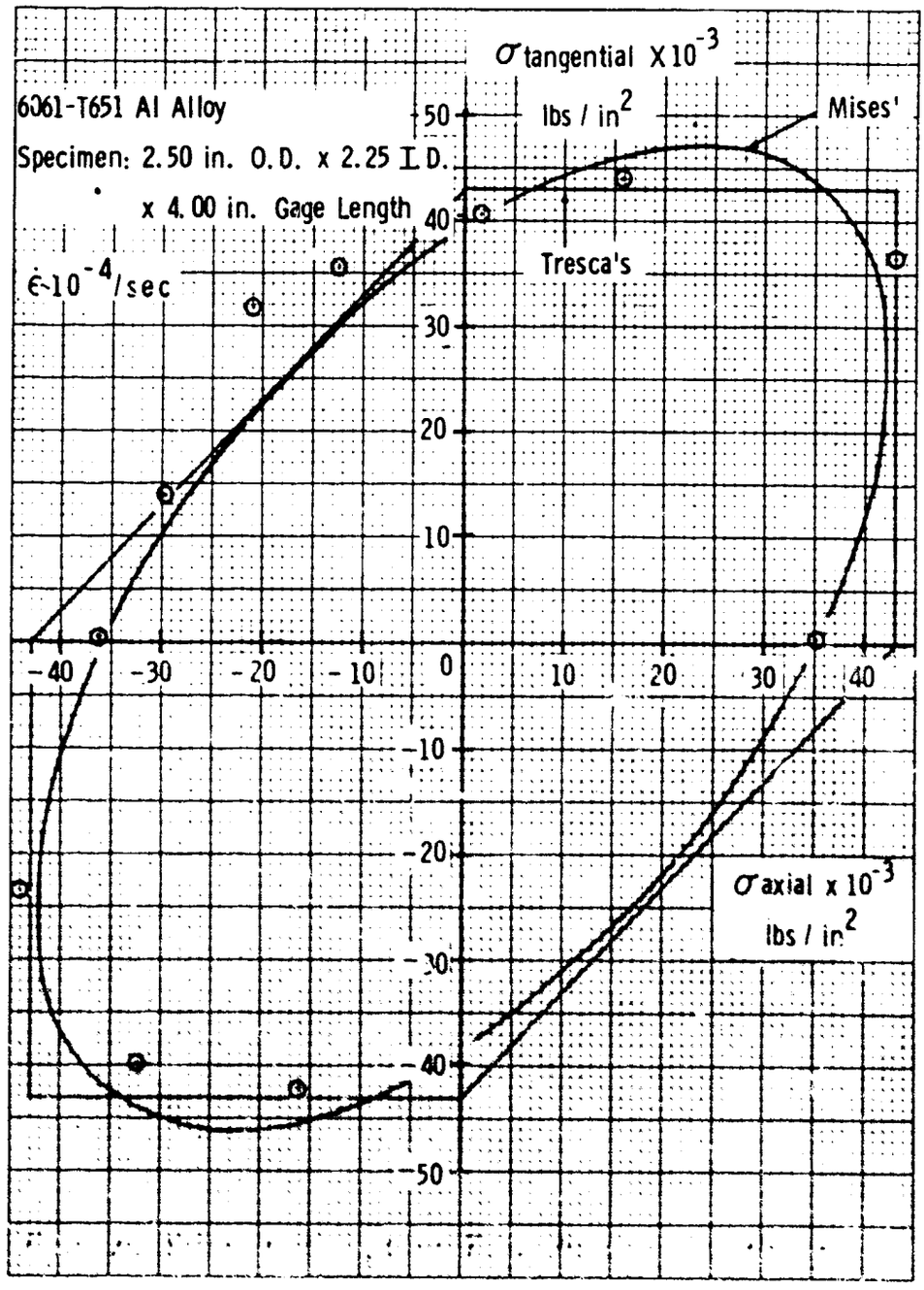

Figure 10 Biaxial Stress Behavior

SECTION III

ELASTIC BEHAVIOR

Measurement of elastic constants provides additional inputs to the study of material response. The three basic measurements are density, longitudinal (dilatational) wave velocity and shear (transverse) wave velocity. Values obtained at standard temperature and pressure (20°C and atmospheric pressure) establish the parameters used in first-order (temperature and pressure independent) calculations of material response. Measurements of temperature and pressure dependence permit more exact calculations to be made and, in particular, lead to prediction of pressure-compression isotherms, adiabats and hydrostats. If these measurements are made with sufficient accuracy (< 0.1%), the calculated pressure-compression behavior can frequently be extrapolated with reasonable confidence to higher pressures than covered in the actual measurements.

WAVE VELOCITY MEASUREMENTS

Initial measurements of longitudinal and shear wave velocities were made at 20°C and atmospheric pressure (i.e., P = 0). Values obtained were:

$$C_L = 6.368 \pm 0.006 \text{ mm/}\mu\text{sec}$$

$$C_S = 3.197 \pm 0.003 \text{ mm/}\mu\text{sec}$$

Although the accuracy of these measurements is estimated to be about ± 0.1%, it should be noted that C_L and C_S may vary significantly depending on the structural form of the material (i.e., plate, bar, etc.), thermal and mechanical history, and the measurement direction relative to any structural anisotropy. A review of the literature on elastic wave velocities in 6061-T6 gave values of C_L ranging from 6.34 to 6.48 mm/μsec and C_S ranging from 3.04 to 3.26 mm/μsec.[20-23] These variations may be partly due to differences in experimental technique but seem to be primarily the result of differences in composition, structure, texture, and orientation. For example, with 50.8 mm plate stock, C_L normal to the plate was about 0.5% less than C_L in the plane of the plate.

Measurements were also made of the temperature and hydrostatic pressure dependence of the wave velocities. Correction of the data for thermal expansion and hydrostatic compression gave the following:

Temperature Dependence, 0-100°C, P = 0

$$C_L = 6.387 - (0.00093\ T) \text{ mm/μsec}$$

$$C_S = 3.214 - (0.00084\ T) \text{ mm/μsec}$$

(T in °C)

Pressure Dependence, 0-9 kbar, T = 20°C

$$C_L = 6.368 + (0.0180\ P) - (0.0001\ P^2) \text{ mm/μsec}$$

$$C_S = 3.197 + (0.0108\ P) - (0.00005\ P^2) \text{ mm/μsec}$$

(P in kbar)

For comparison, Asay, et al.[21], reported the temperature dependence of C_L and C_S in 6061-T6 as $C_L = 6.428 - 0.00091 \times T$ and $C_S = 3.199 - 0.00086 \times T$. They also determined the third-order elastic constants at 25°C using a uniaxial stress technique and obtained $\nu_1 = -3010$ kbar, $\nu_2 = -1310$ kbars and $\nu_3 = 1410$ kbar, where ν_1, ν_2, and ν_3 are the third-order Lamé constants for an isotropic elastic body.[24]

ELASTIC CONSTANTS

Assuming the material is isotropic* (C_L and C_S are independent of direction of measurement in a polycrystalline specimen), wave velocity data are used to calculate various elastic constants (see, e.g., Refs. 28-31). At 20°C and zero pressure, the following adiabatic constants were obtained (see Appendix A):

Bulk wave velocity, $C_B = 5.19$ mm/μsec
Sound wave velocity, $C_E = 5.22$ mm/μsec
Rayleigh wave velocity, $C_R = 2.99$ mm/μsec
Poisson's ratio, $\nu = 0.331$
Bulk modulus, $K = 728$ kbar
Shear modulus, $G = 276$ kbar
Elastic modulus, $E = 735$ kbar
Lamé's parameter, $\lambda = 544$ kbar

* A cubic material is elastically isotropic when $\frac{2C_{44}}{C_{11} - C_{12}} = 1$, where C_{44}, C_{11} and C_{12} are elastic stiffness constants. Single-crystal aluminum (99.95%) is only slightly anisotropic with $\frac{2C_{44}}{C_{11} - C_{12}} \simeq 1.2$ at 20°C.[25-27]

The bulk and shear moduli are used in the development of the ultrasonic equation of state. They were obtained first as functions of T and P from the following:

$$K = \rho \left(C_L^2 - \frac{4}{3} C_S^2 \right) \quad (1)$$

$$G = \rho C_S^2 \quad (2)$$

This gave:

Temperature dependence, P = 0

$$K = 732 - (0.176\ T) \text{ kbar}$$

$$G_S = 279 - (0.165\ T) \text{ kbar}$$

Pressure dependence, T = 20°C

$$K_S = 728 + (4.75\ P) - (0.01\ P^2) \text{ kbar}$$

$$G_S = 276 + (2.25\ P) - (0.006\ P^2) \text{ kbar}$$

where the superscript S indicates adiabatic.

Finally, isothermal values of K and G as well as adiabatic and isothermal pressure and temperature derivatives at 20°C and zero pressure were calculated using the equations given in Appendix A. Results are given in Table II. Use of these constants in calculating the isotherm, adiabat and hydrostat is discussed in the section on Ultrasonic Equation of State.

GRUNEISEN PARAMETER

The Gruneisen ratio γ is a parameter originally given by Gruneisen in a solid equation of state relating pressure to

TABLE II

ELASTIC CONSTANTS FOR 6061-T6 ALUMINUM

(P = 0, T = 20°C)

PARAMETER	VALUE
K^S	728 kbar
$(\frac{\partial K^S}{\partial P})_T = K^{S'}_{0T}$	4.75
$(\frac{\partial K^S}{\partial T})_P$	-0.175 kbar/°C
$(\frac{\partial K^S}{\partial P})_S = K^{S'}_{0S}$	4.60
$(\frac{\partial K^S}{\partial T})_S$	5.71 kbar/°C
K^T	700 kbar
$(\frac{\partial K^T}{\partial P})_T = K^{T'}_{0T}$	4.87
$(\frac{\partial K^T}{\partial T})_P$	-0.281 kbar/°C
$(\frac{\partial K^T}{\partial P})_S = K^{T'}_{0S}$	4.64
$(\frac{\partial K^T}{\partial T})_S$	5.75 kbar/°C
$G^S = G^T$	276 kbar
$(\frac{\partial G}{\partial P})_T = G'_{0T}$	2.25
$(\frac{\partial G}{\partial T})_P$	-0.164 kbar/°C
$(\frac{\partial G}{\partial P})_S = G'_{0S}$	2.12
$(\frac{\partial G}{\partial T})_S$	2.64 kbar/°C

volume and energy, $\gamma = V\,(\partial P/\partial E)_V$ (see, e.g., Refs. 32-34). This parameter can be defined thermodynamically as:

$$\gamma = -\frac{1}{\rho c_p}\left(\frac{\partial V}{\partial T}\right)_P\left(\frac{\partial P}{\partial V}\right)_S = \frac{\beta K^S}{\rho c_p} \tag{3}$$

For an isotropic elastic solid, this can be expressed as

$$\gamma = \frac{\beta}{c_p}\left(C_L^2 - \frac{4}{3}C_S^2\right) \tag{4}$$

where C_L and C_S are measured under adiabatic conditions.

At 20°C and zero pressure this gave

$$\gamma_0 = 1.97$$

The zero-pressure Gruneisen parameter can also be estimated by several other methods, including those of Slater[35], Dugdale and MacDonald[36], Anderson and Dienes[37,38] and Schuele and Smith[37,39]. These methods are discussed in Appendix B.

An estimate of the temperature dependence of the Gruneisen parameter can be obtained by differentiating Equation 3 with respect to temperature. At constant pressure (P = 0, T = 20°C):

$$\left(\frac{\partial \gamma}{\partial T}\right)_P = \gamma_0\left[\frac{1}{\beta}\left(\frac{\partial \beta}{\partial T}\right)_P + \frac{1}{K^S}\left(\frac{\partial K^S}{\partial T}\right)_P - \frac{1}{\rho}\left(\frac{\partial \rho}{\partial T}\right)_P - \frac{1}{c_p}\left(\frac{\partial c_p}{\partial T}\right)_P\right] = -0.000051/°C \tag{5}$$

The pressure dependence can be estimated by differentiating with respect to pressure (see Appendix C). At constant temperature (T = 20°C, P = 0):

$$\left(\frac{\partial\gamma}{\partial P}\right)_T = \frac{\gamma_0}{K^S}\left[\left(\frac{\partial K^S}{\partial P}\right)_T + \frac{1}{\beta K^T}\left(\frac{\partial K^S}{\partial T}\right)_P - 1 - \gamma - T\left(\frac{\partial\gamma}{\partial T}\right)_P\right] = -0.0051/\text{kbar} \qquad (6)$$

Another approach is to assume γ/V constant, which permits $(\partial\gamma/\partial P)_T$ to be estimated directly from the bulk modulus data (see Appendix C). At constant temperature (20°C):

$$\left(\frac{\partial\gamma}{\partial P}\right)_T = \frac{-\gamma_0}{\left(\frac{1}{K_0^T}\right)^{\left(1/K_{0T}^{T'}\right)}\left(K_0^T + K_{0T}^{T'}P\right)^{\left(1+K_{0T}^{T'}\right)/K_{0T}^{T'}}} \qquad (7)$$

$$= \frac{-7.57}{(700 + 4.87P)^{1.205}}$$

$$= -0.0028/\text{kbar} \text{ @ } P = 0$$

$$= -0.0015/\text{kbar} \text{ @ } P = 100 \text{ kbar}$$

DEBYE TEMPERATURE

The Debye temperature θ is a parameter related to the maximum oscillation frequency a system assumed to be an elastic continuum can support. It is an important parameter in thermal energy calculations and indicates the temperature above which variations due to temperature for some thermodynamic

parameters such as specific heat, thermal expansion and Grueisen ratio become small. There are a number of methods for calculating the Debye temperature[33,40-42], and one approximation suitable for use with elastic wave velocity data for polycrystalline metals is:

$$\theta = \frac{h}{k}\left(\frac{9N}{4\pi V}\right)^{1/3}\left(\frac{1}{C_L^3}+\frac{2}{C_S^3}\right)^{-1/3}$$

where h is Planck's constant, k is Boltzmann's constant, N is number of mass points and V is sample volume.

At 20°C, the elastically-determined Debye temperature for 6061-T6 is:

$$\theta = 4.3 \times 10^{-5}\left(\frac{N}{V}\right)^{1/3}\left(\frac{1}{C_L^3}+\frac{2}{C_S^3}\right)^{-1/3} \qquad (8)$$

$$\theta = 420°K$$

for N = 4 (atoms per unit cell), V = $(4.04 \times 10^{-7}$ mm$)^3$ (lattice constant), C_L = 6.368 mm/μsec and C_S = 3.197 mm/μsec.

Sutton[43] reported a Debye temperature for single-crystal aluminum (99.93%) of 407°K at 20°C.

SECTION IV

EQUATION OF STATE

The development of material response models and computational codes requires extensive data on material behavior under uniaxial strain conditions, including equation of state, wave propagation and spall fracture. Most data are used directly in developing models of material behavior, although independent check data (attenuated wave shapes and spall wave profiles) are necessary to determine accuracy of the calculations. This section presents the equation of state analysis, and the following two sections cover wave propagation and spall fracture.

SHOCK WAVE EQUATION OF STATE

The hugoniot equation of state is the locus of equilibrium states reached after shocking of a material, and data are usually obtained either as stress-particle velocity points or as shock velocity-particle velocity points (see, e.g., Refs. 44-49). The shock wave hugoniot data for 6061-T6 presented in this report were obtained with x-cut quartz gages and optical techniques. Representative quartz gage records for direct impact and transmitted wave tests are shown in Figure 11. The buffered direct impact method (tungsten carbide buffer plate on front of the quartz) permitted stresses up to 65 kbar in the aluminum while keeping the stress in the quartz at an acceptable level. The use of quartz gages for transmitted wave tests was primarily for the study of compressive wave development and elastic precursor decay, and results are discussed in the Wave

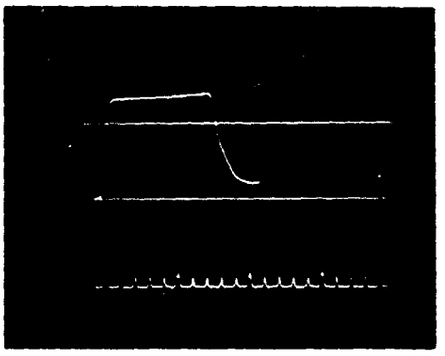

DIRECT IMPACT

Al → Q

V_I = 0.139 mm/μs

σ_H = 10.8 kbar

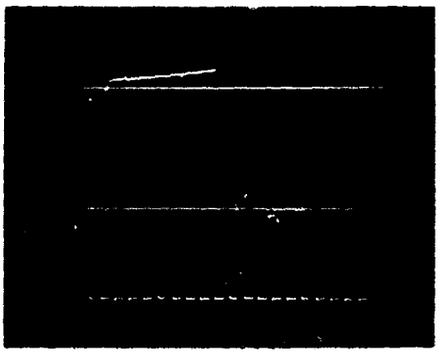

DIRECT IMPACT, BUFFERED

Al → WC/Q

V_I = 0.460 mm/μs

σ_H = 64.0 kbar

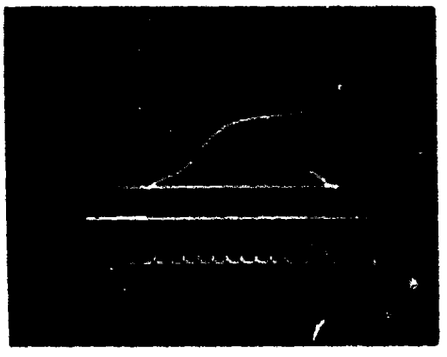

TRANSMITTED WAVE

Al → Al/Q

V_I = 0.173 mm/μs

σ_H = 13.4 kbar

Figure 11 Quartz Gage Records

Propagation section. The direct impact records, which gave a stress-particle velocity point since the hugoniot of quartz is known, showed a rise-time of less than 10 nsec. The slight rounding at the front of the direct impact records in Figure 11 is due to impact tilt, and the ramped peak stress region results from finite-strain effects in the quartz which are corrected in the data analysis.(50)

Hugoniot data at stresses of 70 to 160 kbar were obtained by using a steak camera and a target in the form of a two-step cylinder ("hat" configuration). A schematic of the technique and a sample record are shown in Figure 12. The two surfaces of the target are viewed through the camera slit and shock arrival is observed as a change in surface reflectance. The average shock velocity is obtained from the record, and particle velocity is assumed to be 1/2 V_I (impact velocity) since impactor and target are the same material.

The hugoniot may be expressed in several forms. A convenient form for experimental work is that established by a least-squares stress and particle velocity, as established by a least-squares fit to the data in the stress-particle velocity (σ_H - u_p) plane. Transformation of the hugoniot into various planes, such as shock velocity-particle velocity (U_S - u_p) and stress-volume (σ_H - v), is performed by assuming a material model. This was done by assuming an ideal elastic-plastic wave structure with equilibrium initial and final states and applying the mass and momentum conservation equations. This leads to:

$$\sigma_H = \sigma_e + \rho_e (U_S - u_e) (u_p - u_e) \qquad (9)$$

and

$$v = v_o \left(1 - \frac{u_e}{C_L}\right) \left(\frac{U_S - u_p}{U_S - u_e}\right) \qquad (10)$$

where ρ_e and u_e are density and particle velocity at the elastic limit σ_e.

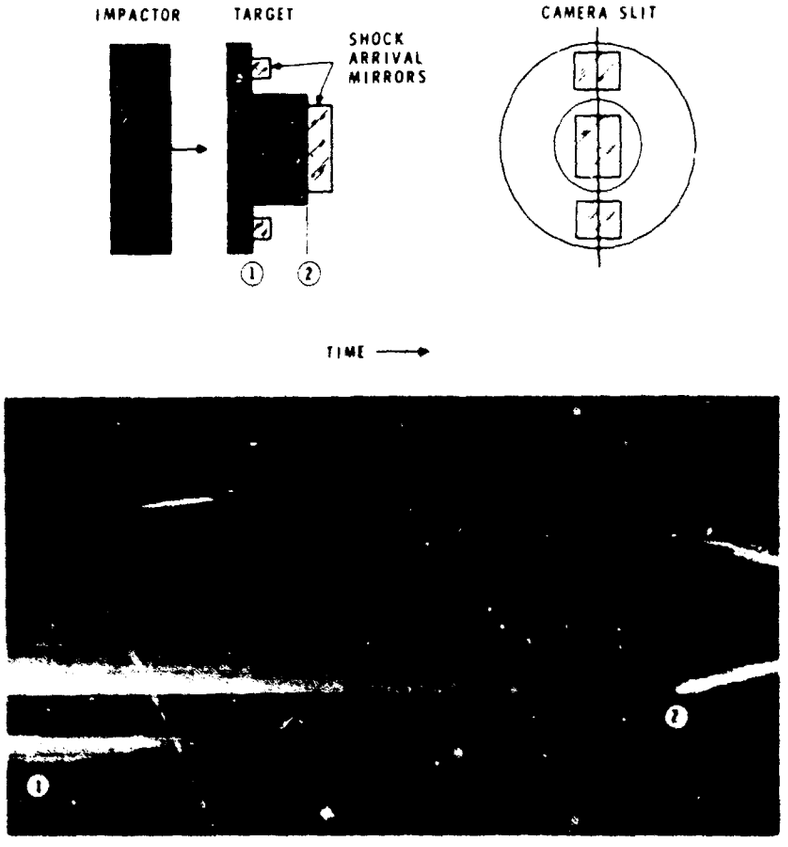

Figure 12 Streak Camera Record, "Hat" Target

Therefore, when either $\sigma_H - u_p$ or $U_S - u_p$ relations are established and σ_e, ρ_e, u_e and C_L are known, σ_H, U_S, u_p and v are uniquely determined. The resulting equations of state for aluminum at 20°C are given in Figures 13, 14 and 15 and are listed below:

$$\left.\begin{aligned} \sigma_H &= 1.0 + 140.4\ u_p + 37.7\ u_p^2 \text{ (Std. Error 0.2 kbar)} \\ \sigma_H &= 2.3 + 708\ \mu + 1607\ \mu^2 \\ P_H &= 708\ \mu + 1607\ \mu^2 \text{ (Hydrostat)} \\ U_S &= 5.24 + 1.40\ u_p \end{aligned}\right\} \quad (11)$$

where $\mu = (v_o/v$

These equations of state are based on the measurements indicated by the symbols in Figure 13 and on σ_e = 5.7 kbar, and are considered to be valid over the stress range of 8 to 200 kbar. Accuracy of the data points is estimated to be ± 2% for σ_H and ± 1% for u_p.

The hydrostat (P_H-μ) was obtained by subtracting the stress-axis intercept value from the σ_H-μ equation. This approach satisfies the requirement that the P_H-μ function pass through the origin and assumes the deviatoric stress (σ_D) is constant at 2.3 kbar (no strain hardening). Alternative ways of estimating σ_D are discussed in Appendix D.

The low-pressure hugoniot of 6061-T6 was reported previously by Lundergan and Herrmann[51], who used the flat-plate impact technique and free-surface velocity measurements to determine the

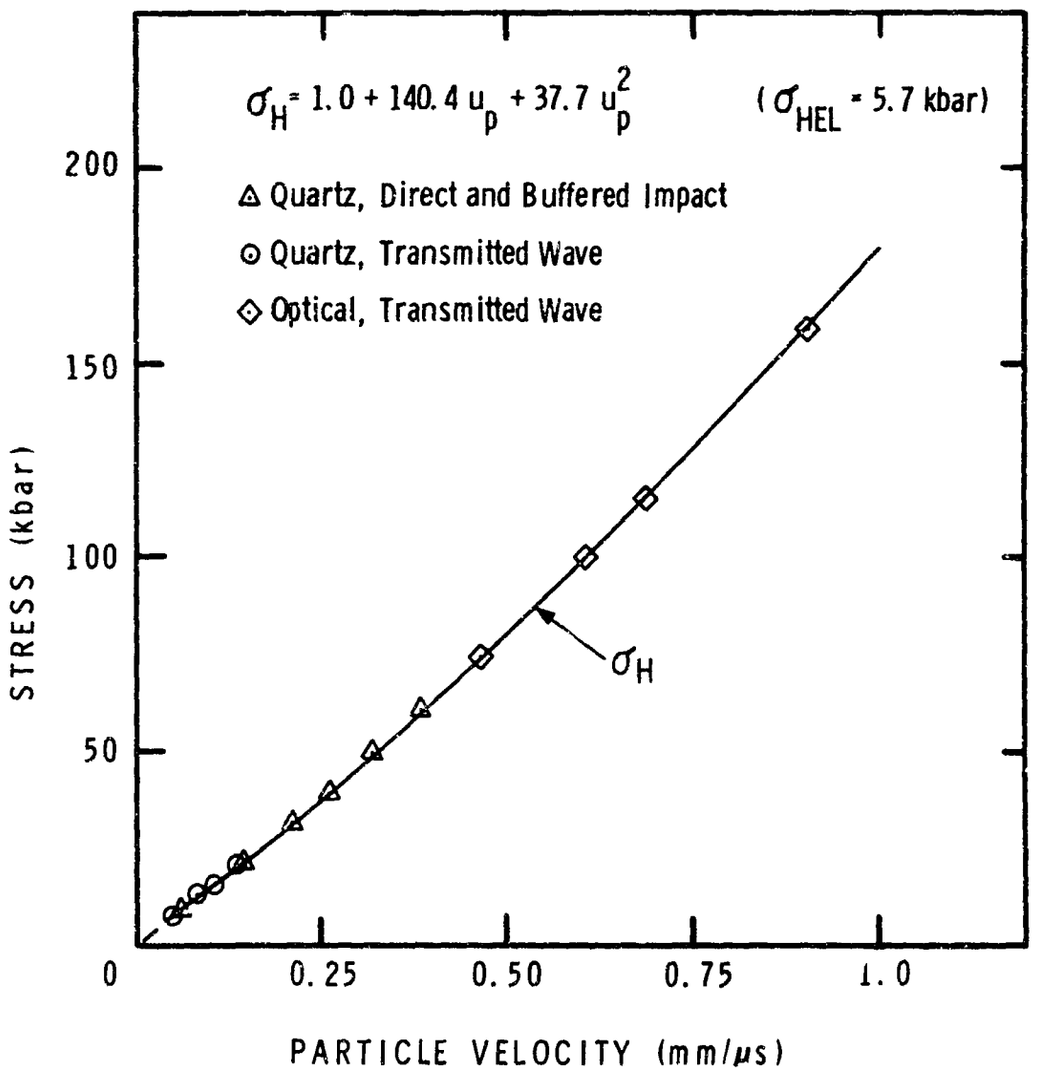

Figure 13 Stress-Particle Velocity Hugoniot, 6061-T6

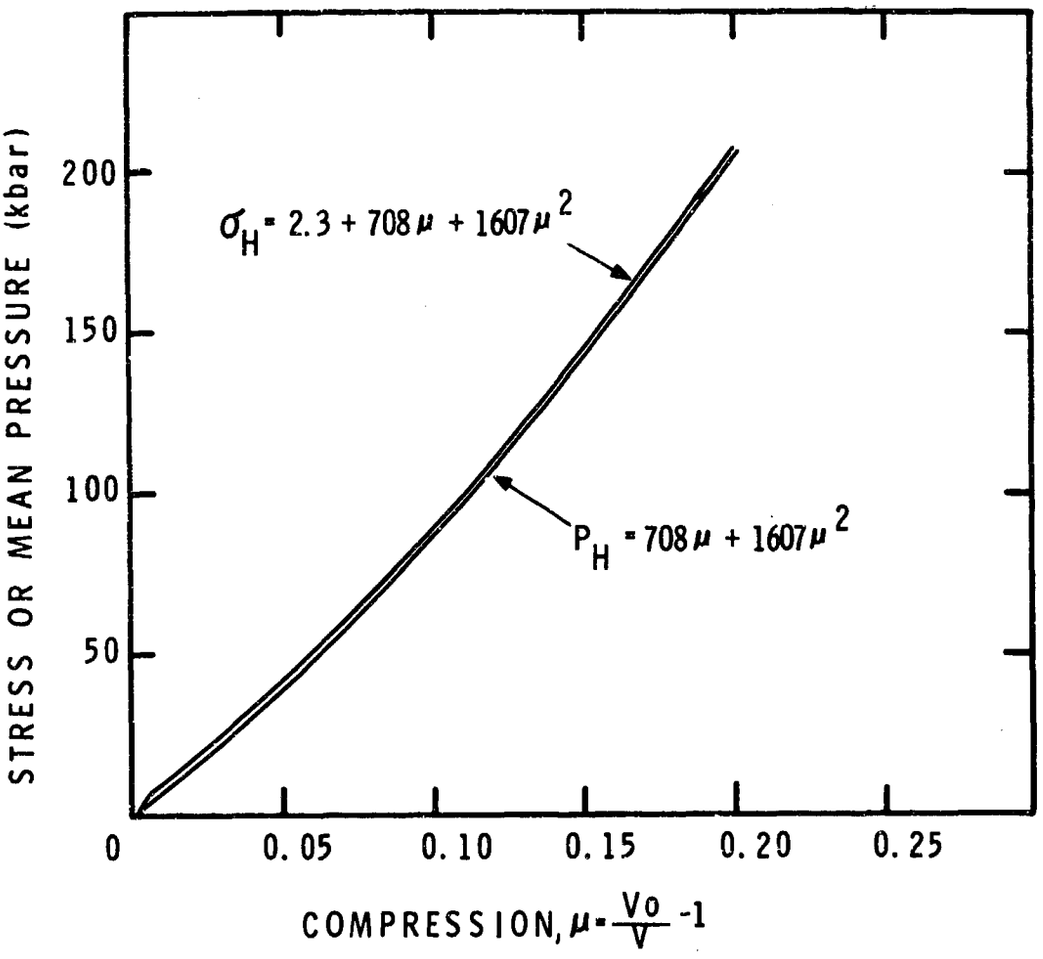

Figure 14 Stress or Mean Pressure-Compression Hugoniot, 6061-T6

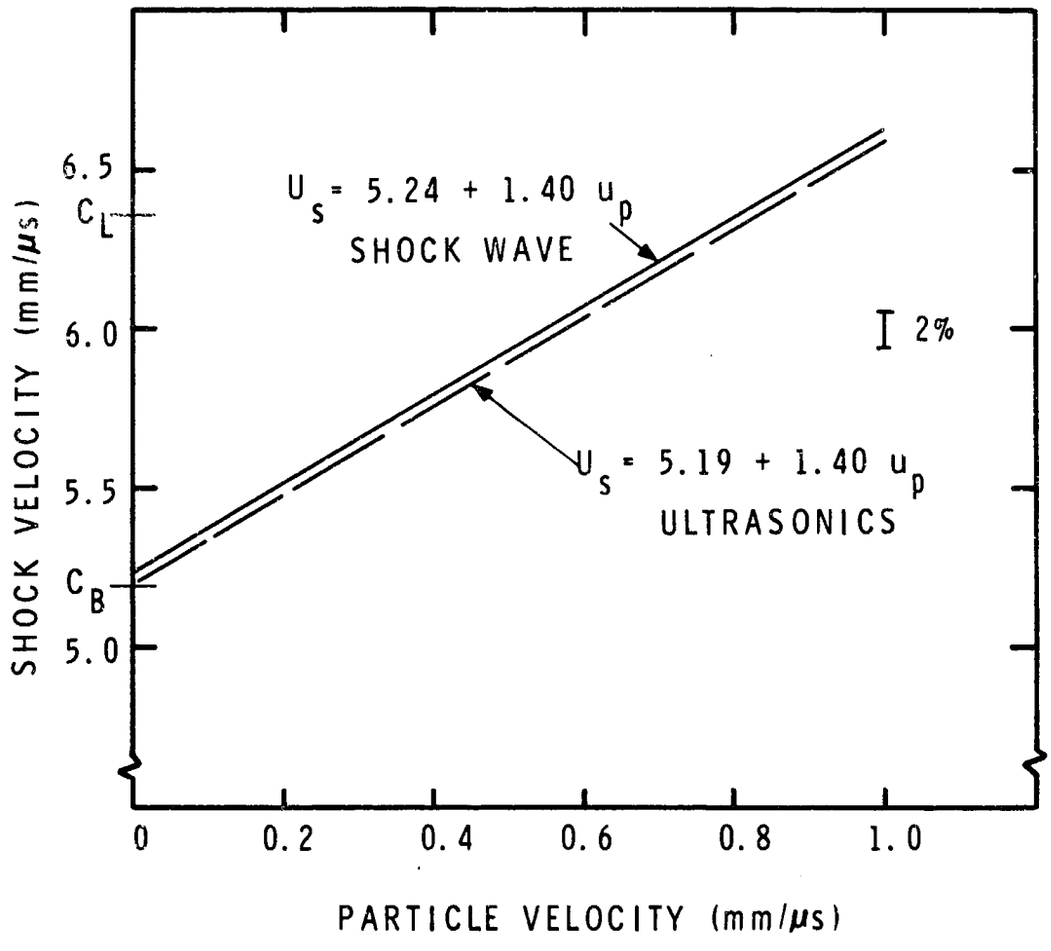

Figure 15 Shock Velocity-Particle Velocity Hugoniot, 6061-T6

equation of state up to 31 kbars. Results were given as a linear elastic portion ($\sigma_H = 1044\ (\mu/1+\mu)$) up to 6.4 kbar and a linear plastic portion from 6.4 to 31 kbar represented by:

$$\sigma_H = 1.6 + 794\ (\mu/1+\mu) \qquad (12)$$

Comparing this with the hugoniot obtained in the present study gives:

μ	σ_H (Eq. 11) kbar	σ_H (Eq. 12) kbar
0.01	9.5	9.5
0.02	17.1	17.2
0.03	25.0	24.7
0.04	33.2	32.1

The agreement is good over the stress range reported by Lundergan and Herrmann.

The temperature dependence of the hugoniot for 6061* was determined using x-cut quartz gages[52]. Measurements were made at 300° and 550°C and results are given in Figure 16. The stress-particle velocity hugoniots are given by:

* Although the starting material was 6061-T6, the heating times were long enough such that diffusion processes were irreversibly changing material properties and the "-T6" designation is no longer applicable.

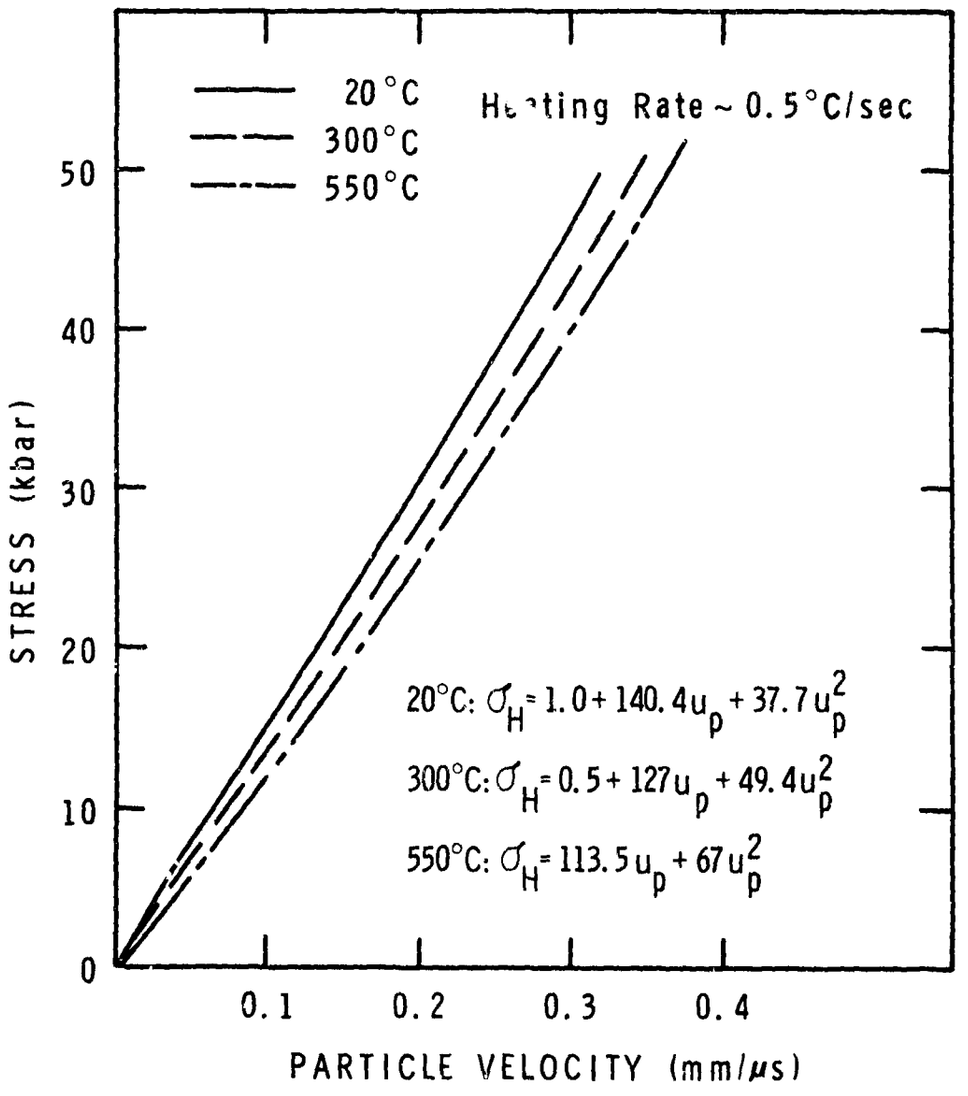

Figure 16 Stress-Particle Velocity Hugoniot, Temperature Dependence, 6061

300°C: $\sigma_H = 0.5 + 127\ u_p + 49.4\ u_p^2$

(Six data points)

550°C: $\sigma_H = 113.5\ u_p + 67\ u_p^2$

(Five data points)

(σ_H < 50 kbar)

ULTRASONIC EQUATIONS OF STATE

The equation of state can also be determined from ultrasonics measurements (see, e.g., Refs. 53-57). The very accurate measurement of elastic wave velocities (and, therefore, bulk modulus) as a function of hydrostatic pressure makes it possible to directly estimate shock wave compression behavior or to combine ultrasonics data with shock wave data to predict very high pressure response. Numerous analytical and empirical relations have been developed for relating pressure, volume and bulk modulus, including those of Birch[58,59], Murnaghan[60] and Keane[61,62]. The use of these relations is discussed in Appendix E and results are summarized below:

Birch EOS

$$P_T = 1050 \left[(1+\mu)^{7/3} - (1+\mu)^{5/3} \right] \left[1+0.653 \left\{ (1+\mu)^{2/3} - 1 \right\} \right] \quad (13)$$

Murnaghan EOS, Isotherm

$$P_T = 143.7 \left[(1+\mu)^{4.87} - 1 \right] \quad (14)$$

Murnaghan EOS, Adiabat

$$P_S = 158.3 \left[(1+\mu)^{4.60} - 1 \right] \tag{15}$$

Keane EOS, $K_\infty^{S'} = 1.93$

$$P_S = 896 \left[(1+\mu)^{1.93} - 1 \right] - 1004 \ln(1+\mu) \tag{16}$$

In the above equations, subscripts T and S indicate isothermal and isentropic, respectively.

Duvall gives a correction for the change in entropy across a shock front based on the Murnaghan equation of state:[56,63]

$$P_H = P_S + \frac{\gamma_0 K_0^S}{12} \left(K_{0S}^{S'} + 1 \right) \left(\frac{\mu}{1+\mu} \right)^3$$

$$P_H = P_S + 676 \left(\frac{\mu}{1+\mu} \right)^3 \tag{17}$$

Zel'dovich gives an expression relating P_S and P_T, assuming γ/v is constant:[56,64]

$$P_S = P_T + \beta T_0 K_0^T \left[\exp \left\{ \gamma_0 \left(\frac{\mu}{1+\mu} \right) \right\} - (1+\mu) \right]$$

$$P_S = P_T + 14.2 \left[\exp \left\{ 1.97 \left(\frac{\mu}{1+\mu} \right) \right\} - (1+\mu) \right] \tag{18}$$

The above equations of state are compared to the shock wave EOS in Table III. The entropy correction based on the Murnaghan equation has been applied to the Birch and Keane equations as well. The ultrasonic equations of state show good agreement with each other and with the shock wave hydrostat, with the maximum deviation being less than ± 2% up to 115 kbars.

The shock velocity-particle velocity relationship can also be determined from ultrasonic data. Following the method of Ruoff[65] one obtains:

$$U_S = C_B + Su_p + Au_p^2 \tag{19}$$

where $C_B = \left(\frac{K_0^S}{10\rho_0}\right)^{1/2}$

$$S = 1/4\left(K_{0S}^{S'} + 1\right) \tag{20}$$

$$A = \frac{1}{24\,C_B}\left[S\left(7 - K_{0S}^{S'} + 4\gamma_0\right) + 2K_0^S K_{0S}^{S''}\right]$$

For aluminum:

$$U_S = 5.19 + 1.40\,u_p - 0.12\,u_p^2$$

The u_p^2 coefficient (A = -0.12) was calculated for $K_{0S}^{S''} = -0.02$. If one assumed $K_{0S}^{S''} = 0$, then A = + 0.12. Since the uncertainty in $K_{0S}^{S''}$ is $\sim \pm 0.02$, the 'A' coefficient will be taken as zero, which gives:

$$U_S = 5.19 + 1.40\,u_p \tag{21}$$

TABLE III

EQUATIONS OF STATE COMPARISON-HYDROSTAT, 6061-T6 ALUMINUM

$\mu = \frac{V_o}{V} - 1$	P_H, HUGONIOT MEAN PRESSURE (kbar)				
	BIRCH EQ. 13	MURNAGHAN EQ. 14	MURNAGHAN EQ. 15	KEANE EQ. 16	SHOCK WAVE EQ. 11
0.025	18.7	18.7	19.0	18.9	18.7
0.050	39.3	39.3	39.9	39.6	39.4
0.075	61.6	61.9	62.7	61.8	62.1
0.100	86.1	86.8	87.6	85.7	86.9
0.125	112.5	113.9	114.7	111.3	113.6

This is compared with the linear $U_S - u_p$ relation obtained from low-pressure shock wave data in Figure 15.

Vaidya and Kennedy measured the hydrostatic compressibility of 6061-T6 aluminum up to 45 kbar.[66] Results were given as:

$$-\frac{\Delta V}{V_o} = \frac{\mu}{1+\mu} = 1.2281 \times 10^{-3} P_T - 8.793 \times 10^{-6} P_T^2 + 0.10266 \times 10^{-6} P_T^3 \qquad (22)$$

Comparing this with the shock wave and ultrasonic results presented in this report gives:

μ	P_T(Eq. 11)* kbar	P_T(Eq. 14) kbar	P_T(Eq. 22) kbar
0.0125	8.9	9.0	10.8
0.0250	18.4	18.4	22.5
0.0375	28.2	28.2	34.5
0.0500	38.6	38.5	45.7

* Corrected for isothermal conditions.

The hydrostatic data of Vaidya and Kennedy are ∿ 20% above ($P_T - \mu$ plane) the shock wave and ultrasonic data. The reason for this large difference is not known.

YIELD BEHAVIOR

A complete description of the low-pressure equation of state requires consideration of yield behavior or the hugoniot elastic limit. Values of compressive yield were obtained by three independent methods.

A. Uniaxial Stress

The yield level was determined in uniaxial stress (σ_σ) as a function of strain rate and then converted to uniaxial strain using:

$$\sigma_e = \sigma_\sigma \left(\frac{1-\nu}{1-2\nu} \right) \tag{23}$$

Strain Rate sec^{-1}	σ_e kbar
10^3	5.8
10^{-3}	5.7

B. Wave Profiles

The elastic precursor level was measured as a function of propagation distance using quartz gages. These profiles are discussed in the section on Wave Propagation.

Propagation Distance mm	(12.7 mm Stock) σ_e kbar
2	7.5
12	5.5

C. Hugoniots

The yield level in uniaxial strain was inferred by comparison of the elastic ($\rho_0 C_L$) and plastic (σ_H vs. u_p) hugoniots, i.e., by defining the elastic

limit as the intersection of the elastic response line and the curve-fit to the stress-particle velocity data

$$10\ \rho_0 C_L u_e = A + Bu_e + Cu_e^2 \left(= \sigma_e\right) \qquad (24)$$

Solving for u_e gives

$$u_e = 0.033 \text{ mm/}\mu\text{sec}$$

$$\therefore \sigma_e = 5.7 \text{ kbar}$$

For an isotropic, polycrystalline metal with elastic-perfectly plastic behavior and no strain-rate or time-dependent effects, one would expect the same yield to be obtained by each method. Although not strain-rate sensitive in the uniaxial stress tests, 6061-T6 does show relaxation of the elastic wave in uniaxial strain. However, the elastic wave approaches an "equilibrium" yield of 5-6 kbar which is essentially the same as the yield obtained from uniaxial stress or hugoniot data. An average value of 5.7 kbar was used in determining the $\sigma_H - \mu$ and $U_S - u_p$ equations given above (Equation 11) for 6061-T6 in the low-pressure region.

SECTION V

WAVE PROPAGATION

Compressive wave development and elastic precursor decay are used as basic input data for material response models, while a complete understanding of shock wave propagation requires inclusion of release wave behavior (see, e.g., Refs. 23, 67-70). Profiles of shock waves propagated through a specimen are obtained as stress-time or velocity-time histories. Profiles may be used in this form directly for comparison with calculated or predicted material response. When it is necessary to transform the data to obtain material stress from transducer stress or particle velocity from interface velocity, an impedance matching technique is applied, utilizing the conservation relations and assuming time-independent behavior. The implications of this assumption must be considered when utilizing the transformed data. All wave profiles obtained (quartz gage and velocity interferometer) are given in Appendix F for reference.

COMPRESSIVE WAVE BEHAVIOR

Structure in the compressive wave in 6061-T6 is shown in the quartz gage data in Figure 17.* The wave front is characterized by an elastic portion and a transition to a spreading

* In this and subsequent figures containing quartz gage data, tilt refers to the time required for a step-input to sweep across the gage electrode diameter.

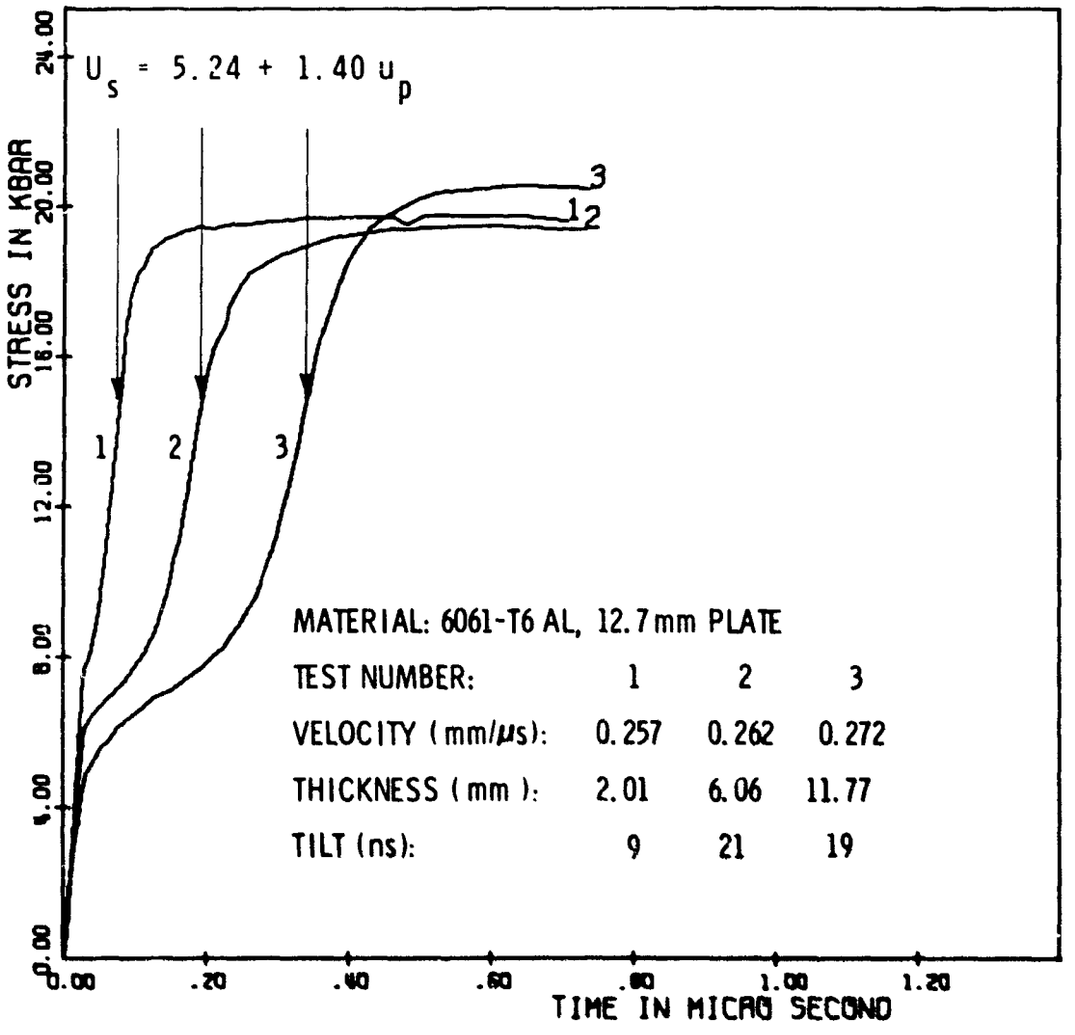

Figure 17 Compressive Waves, Propagation Distance Dependence

plastic wave (nominal final stress of 20 kbar). (The elastic wave would be overdriven by the plastic wave at ∿ 140 kbar.) The elastic portion is not appreciably influenced by peak stress, at least for stresses up to 4 times the elastic limit, as shown in Figure 18. Also shown in Figures 17 and 18 are shock velocities as calculated from the shock wave hugoniot (Equation 11). Although there is qualitative agreement in that the predicted plastic wave velocity lies within the rise-time of the measured wave, the plastic wave cannot be considered to have a unique velocity for a given stress level, at least for stresses below ∿ 25 kbar. This means that transformation of the hugoniot from the $\sigma_H - u_p$ plane to $\sigma_H - u$ or $U_S - u_p$ by assuming ideal elastic-plastic wave structure and steady-state conditions may lead to some uncertainty at lower stresses.

Stress-particle velocity paths were calculated from quartz gage transmitted wave profiles and are compared to the hugoniot in Figure 19. The calculations were made using QZ, a program which assumes steady-state behavior and applies the hugoniot jump conditions incrementally to the wave profile by an impedance matching technique.[50] The dynamic paths generally lie above the equilibrium hugoniot with only the end points or final states approaching the equilibrium values. This deviation is due to time-dependent effects.

The conditions for development of steady-state plastic waves in 6061-T6 were studied by conducting a series of velocity interferometer tests and combining the results with similar data reported by Johnson and Barker.[33] In an elastic-plastic wave system, the effects of time-dependency and non-linearity initially can cause the plastic portion to spread as it propagates. Eventually, however, the plastic portion may achieve a stable condition and propagate relatively unchanged (provided conditions of uniaxial strain are maintained and the wave front is not overtaken by a release wave).

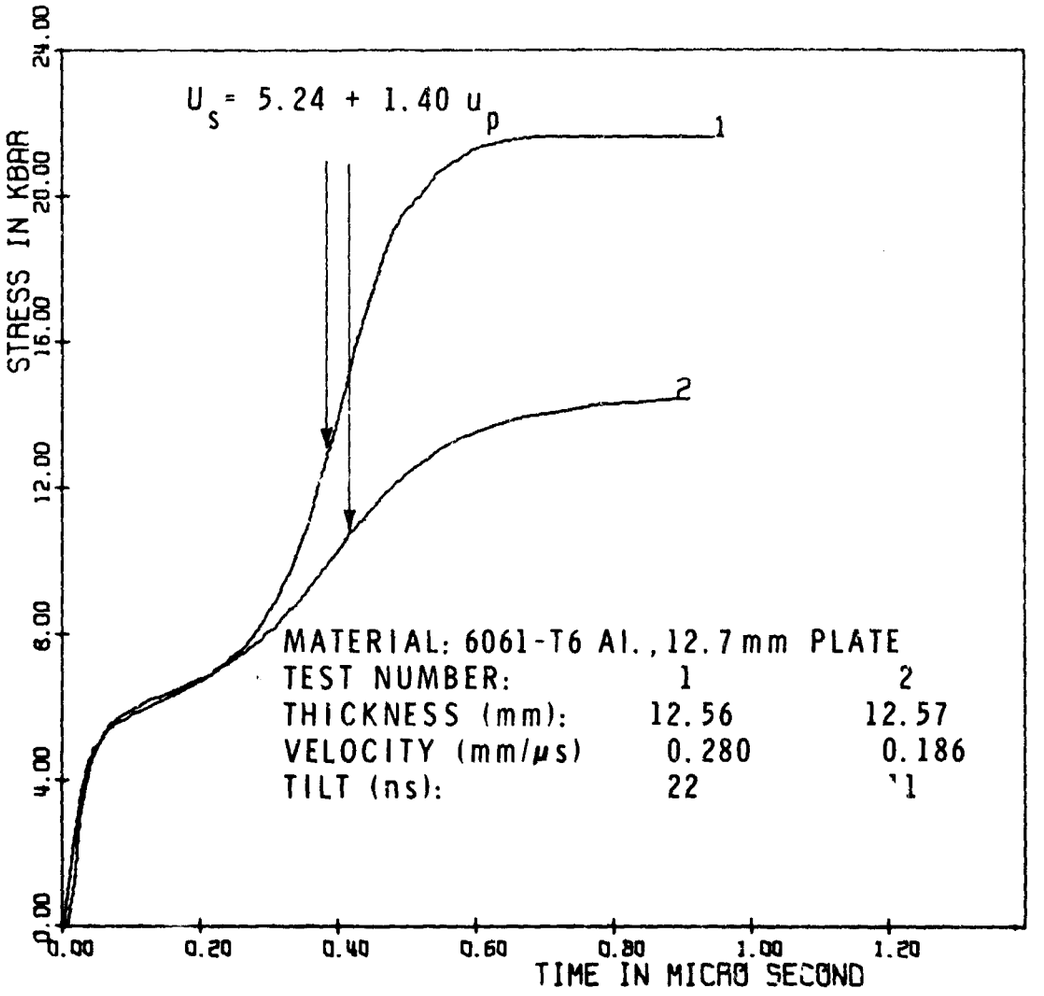

Figure 18 Compressive Waves, Peak Stress Dependence

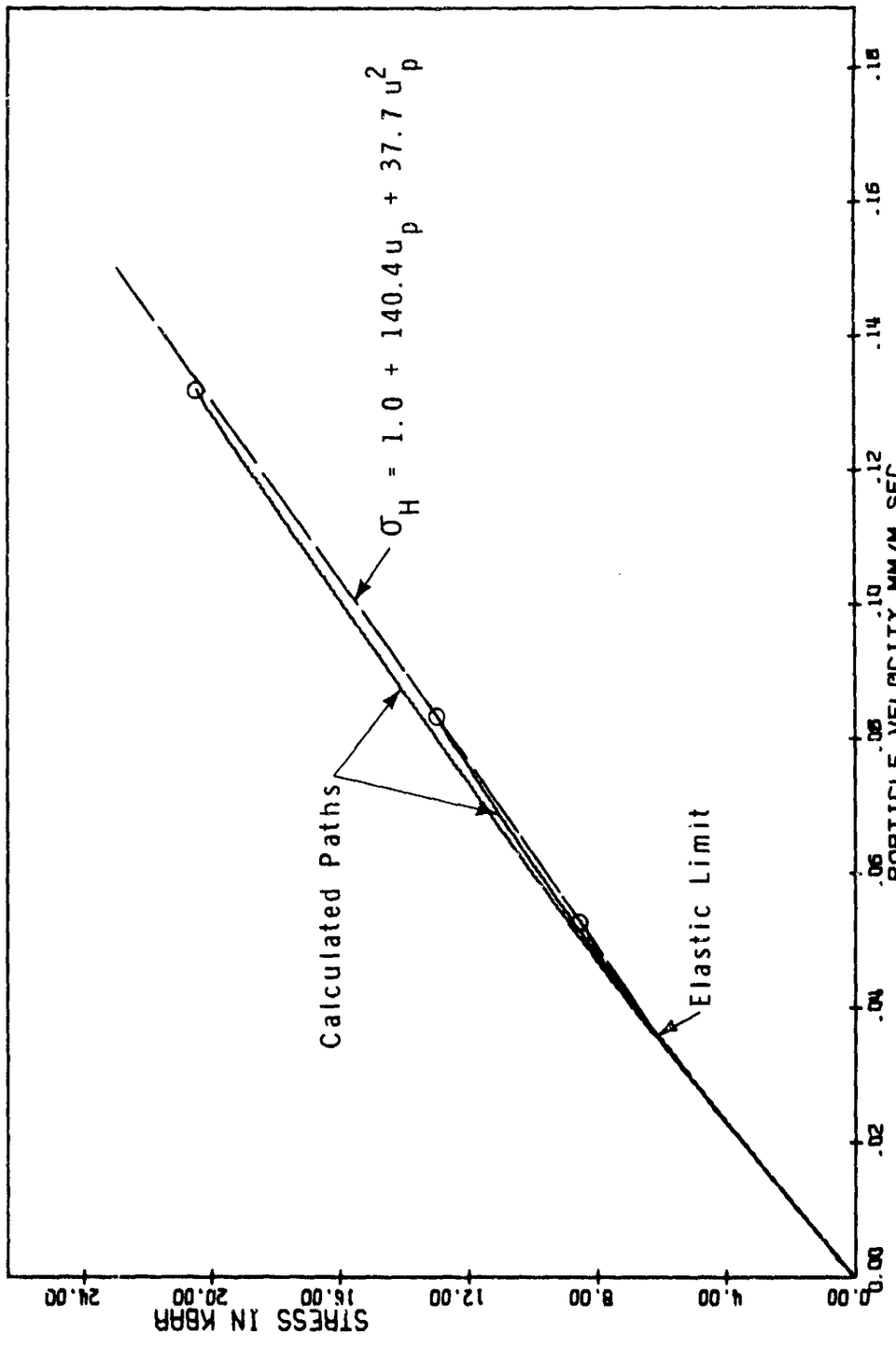

Figure 19 Calculated Stress-Particle Velocity Paths, 6061-T6

Compressive wave profiles are shown in Figure 20 for two series of tests using the velocity interferometer: varying peak stress at constant propagation distance, and varying propagation distance at constant peak stress. (Test conditions for velocity interferometer data discussed in this report are listed in Table IV. The test numbers correspond to those listed next to each wave profile in subsequent figures.) At ∿ 26 kbar the rise-time in the plastic wave increases between 3 and 12 mm, but wave stability is achieved by 20 mm. The series at 3 mm thickness shows a steepening plastic wave with increasing peak stress. A more complete mapping of the formation of steady-state waves is given in Figure 21.* Tests at a given stress which showed steady-state behavior in the plastic wave are shown by solid symbols. The shaded area shows the indistinct border between non-steady-state and steady-state behavior.

Dislocation models for predicting compressive wave development utilize measurements of elastic precursor decay to evaluate various constants related to dislocation density and multiplication.[69-72] Unfortunately, it is very difficult to obtain accurate elastic precursor level data at propagation distances less than ∿ 2 mm and it is in this region (0 to 2 mm) that most of the precursor decay occurs for many metals of interest. Also, even at larger distances there is always some uncertainty in the precursor level due to both material scatter and dispersion characteristics and to experimental errors (particularly tilt). The result is that much of the data presently available, when given realistic uncertainty bars, can be used to support a number of different models of precursor attenuation. The

* Steady-state conditions were studied by comparing rise-times in the plastic wave at approximately 20 to 80% stress levels above the elastic limit.

precursor decay data for 6061-T6 is summarized in Figure 22. The calculated initial elastic impact stress was 23 kbar for these tests and the precursor level has dropped ∿ 70% in 2 mm of travel. Over the range of propagation distance studied, the precursor level in 12.7 mm stock was ∿ 1 kbar greater than in the 3.2 or 6.4 mm stock.

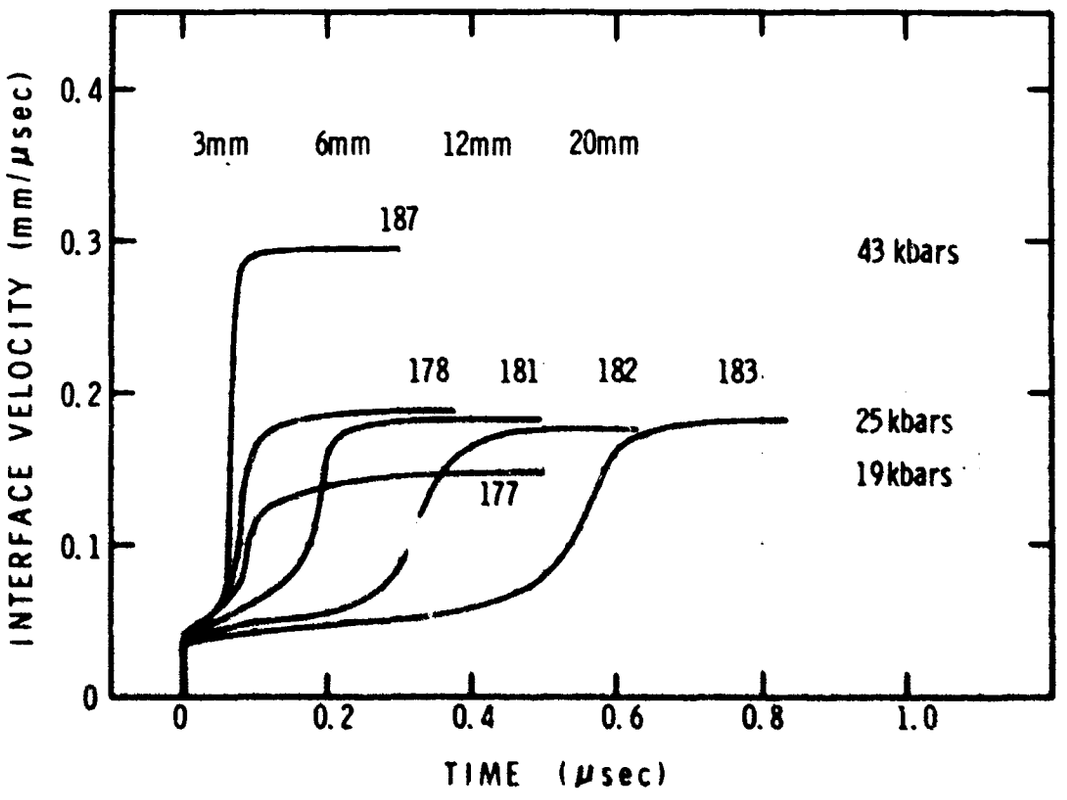

Figure 20 Compressive Wave Development, 6061-T6

TABLE IV

VELOCITY INTERFEROMETER TEST DATA, 6061-T6 ALUMINUM

Test No.	V_I Impact Velocity (mm/μs)	σ Max. Stress (kbar)	X_0 Impactor Thickness (mm)	X Target Thickness (mm)	X/X_0	Stock (mm)	Config.[1]
15	0.269	21	1.879	3.124	1.66	3.2	Al-Al
50	0.222	17	1.552	3.081	1.99	3.2	Al-Al
52	0.252	19	1.587	12.220	7.70	12.7	Al-Al
53	0.284	22	1.440	18.192	12.63	50.8	Al-Al
61[2]	0.510	39	1.580	3.106	1.97	3.2	Al-Al/FQ
63	0.193	15	1.570	3.058	1.95	3 2	Al-Al
73[2]	1.242	103	0.269	2.520	9.37	3.2	Al-Al/FQ
74[2]	1.238	102	0.252	5.067	20.15	6.4	Al-Al/FQ
79[2]	1.235	102	0.252	1.029	4.09	1.6	Al-Al/FQ
83	0.261	20	0.475	1.181	2.49	3.2	Al-Al
104	0.255	19	.590	3.080	1.94	3.2	Al-Al
108	0.263	20	1.562	2.776	1.78	3.2	Al-Al
109	0.340	26	0.431	3.985	9.23	6.4	Al-Al
110	0.418	32	0.419	3.970	9.47	6.4	Al-Al
133	0.265	20	1.600	3.073	1.92	3.2	Al-Al
135	0.247	19	1.598	3.178[3]	1.99	1.6	Al-Al
143	0.306	23	0.904	3.061	3.39	3.2	Al-Al
177	0.275	19	2.982	3.249	1.09	50.8	FQ-Al/FQ
178	0.373	25	3.058	2.972	0.97	50.8	FQ-Al/FQ
181	0.358	24	3.018	6.033	2.00	50.8	FQ-Al/FQ
182	0.354	24	3.061	12.141	3.97	50.8	FQ-Al/FQ
183	0.329	25	12.649	20.259	1.60	50.8	Al-Al/FQ
187	0.489	43	3.157	2.977	0.94	50.8	FQ-Al/FQ

1. e.g., Al-Al is aluminum impactor into aluminum target with free rear surface (FQ is fused quartz window).
2. Plexiglas - backed impactor.
3. Artificial spall plane at X/2.

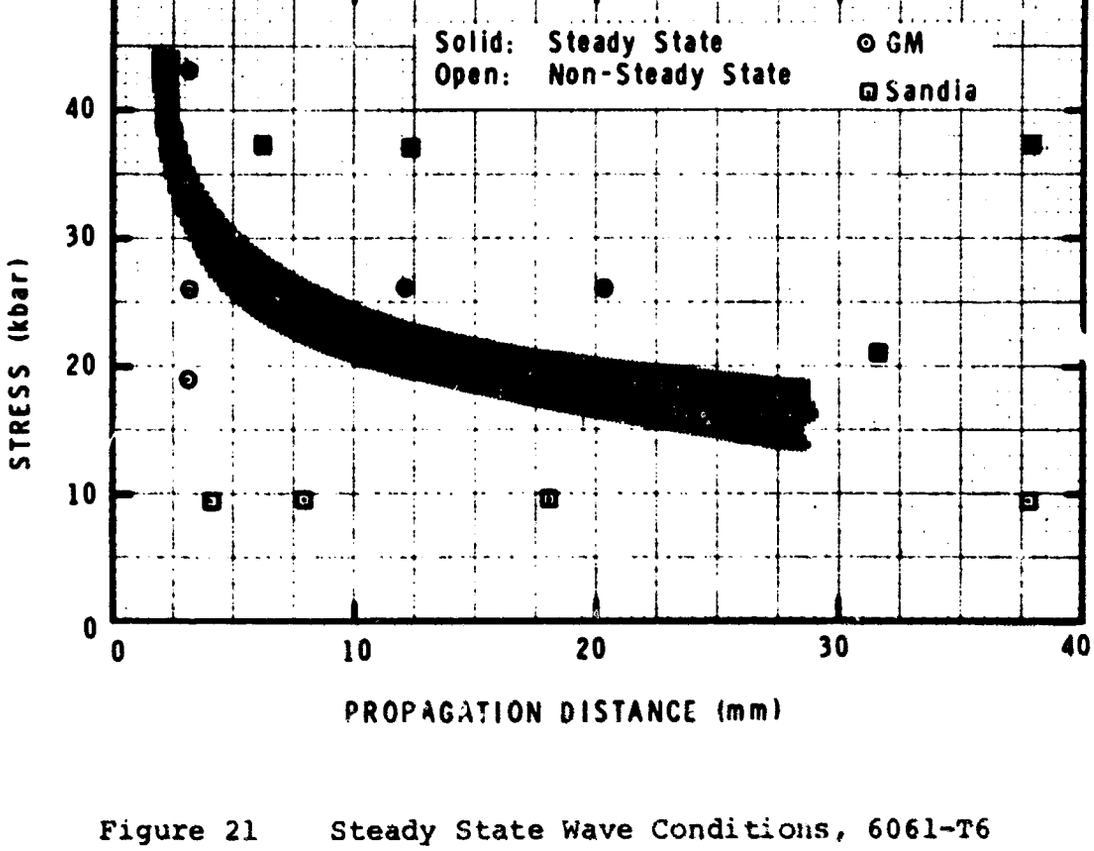

Figure 21 Steady State Wave Conditions, 6061-T6

The uncertainty bars in Figure 22 reflect the dispersion and rounding at the elastic front. This spreading is due to at least two factors. First, since the quartz gage averages stress over the electrode area, small differences in wave front arrival times at the specimen/gage interface would give a finite rise-time rather than an instantaneous stress jump. These small differences in arrival times may be due to wave reflections and dispersion at grain boundaries and to slight differences in local wave velocity arising from grain anisotropy. Second, the influence of shock wave tilt on a finite-area gage is to smooth

out abrupt changes in stress level as well as to increase recording rise-time in the wave front. This becomes particularly severe at short propagation distances where separation of the elastic and plastic waves is only on the order of tens of nanoseconds.

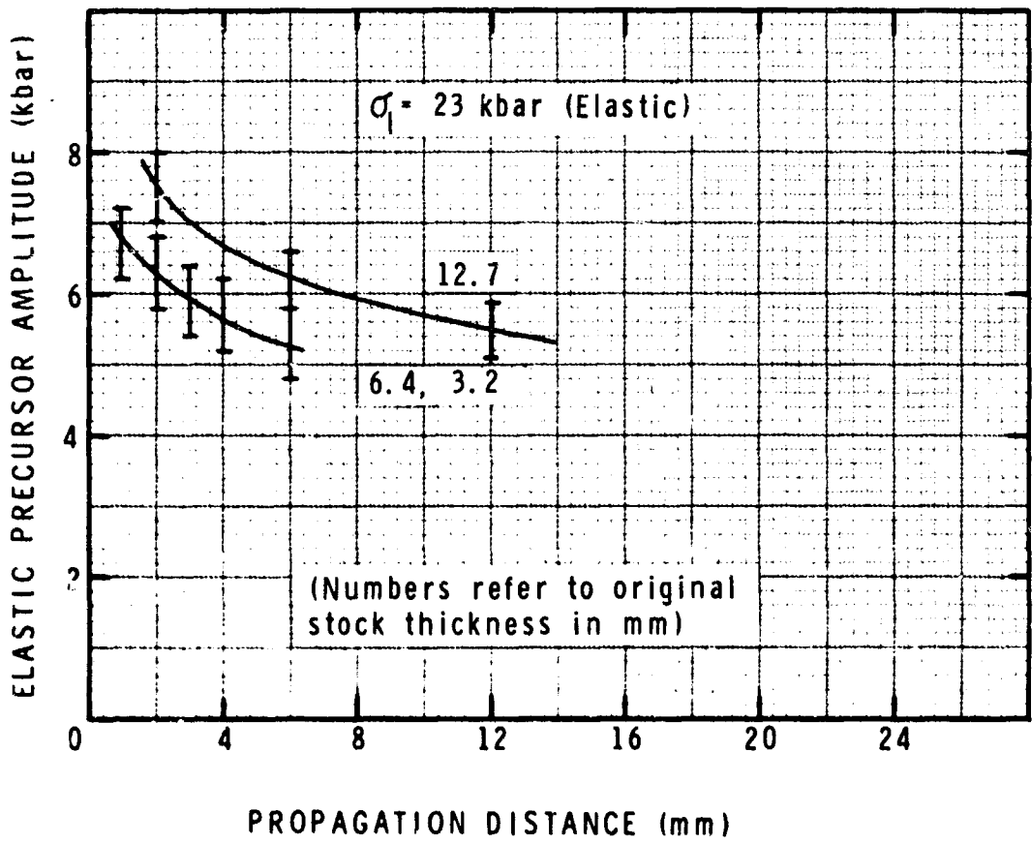

Figure 22 Elastic Precursor Decay, 6061-T6

Of about 15 quartz gage transmitted wave tests conducted with 6061-T6, only one showed relaxation behind the elastic precursor, as shown in Figures 23 and 24. This relaxation was observed for a propagation distance of 11.25 mm with 50.8 mm stock, but was not observed for propagation distances of 6 or 20 mm in targets machined from the same plate. Tilt was slightly higher for the 6 mm test (23 nsec), which may have smeared the wave front such that relaxation could not be resolved. For the 20 mm test, which had a tilt of 16 nsec, the precursor "spike" may have relaxed completely. Material variability could also have influenced the results.

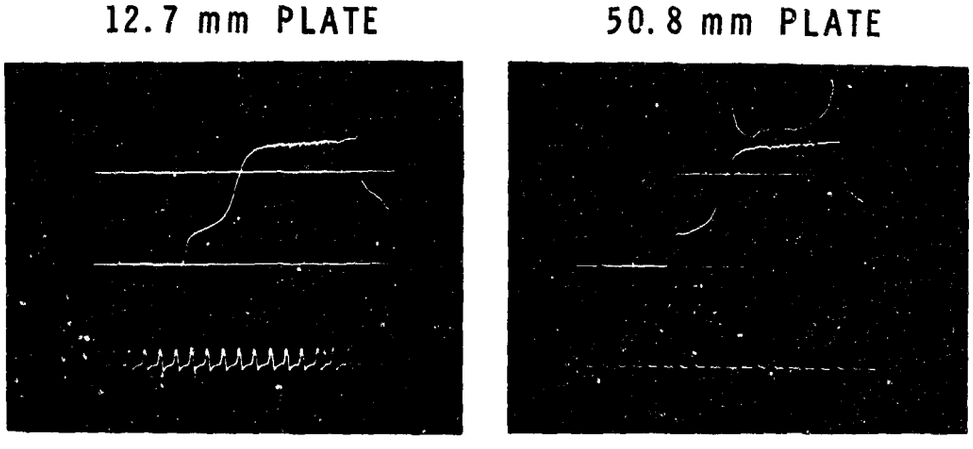

Figure 23 Quartz Gage Transmitted Wave Records, 6061-T6

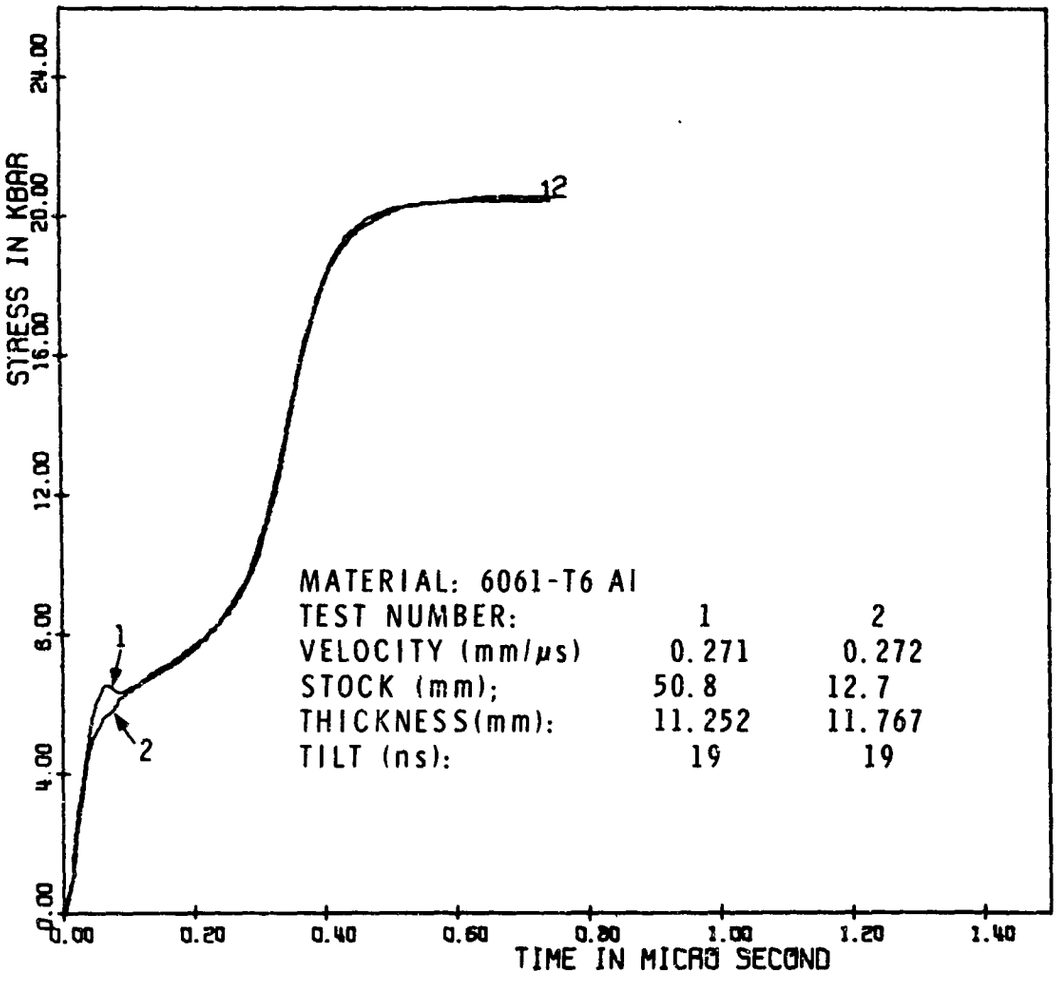

Figure 24 Compressive Waves, Material Differences

Compressive wave structure was also measured in annealed 6061, and is compared with 6061-T6 in Figure 25. The elastic limit has decreased to ∿ 1 kbar for this propagation distance (3.1 mm).

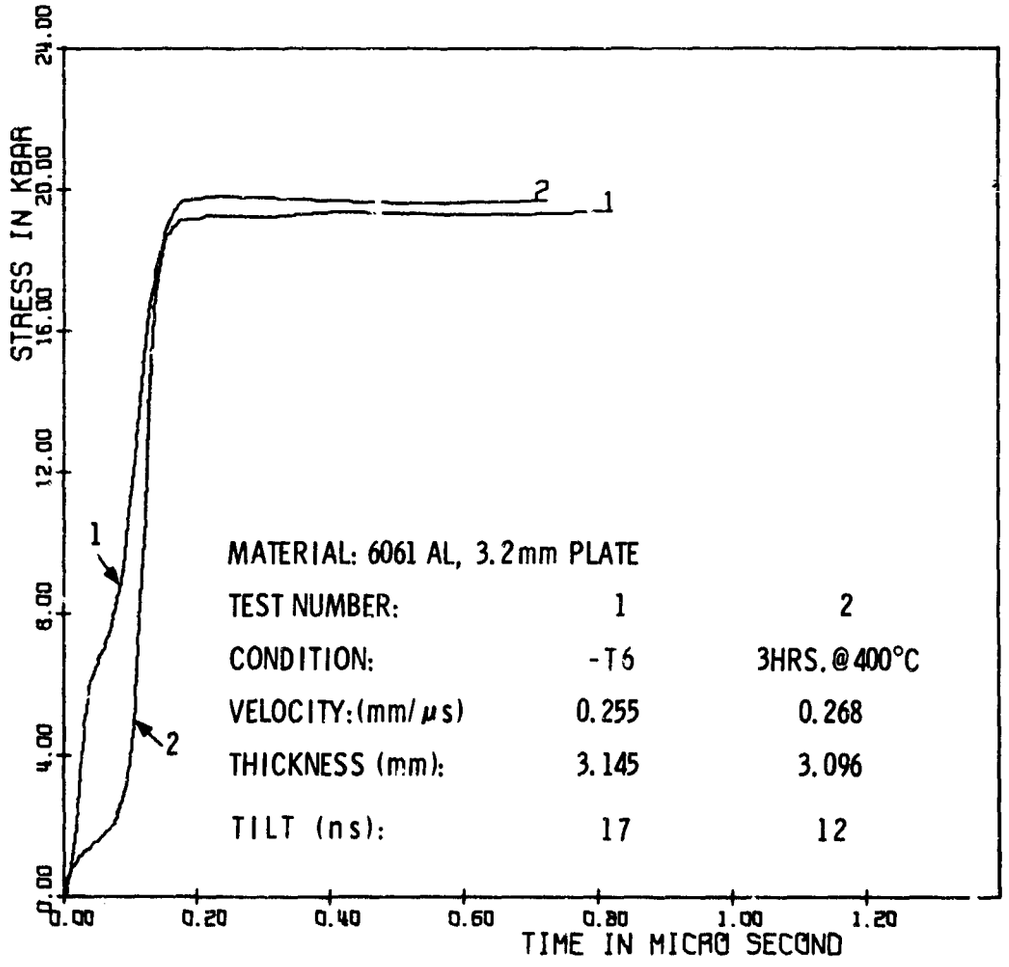

Figure 25 Compressive Waves, Annealing Effect

RELEASE WAVES AND WAVE ATTENUATION

Release waves in 6061-T6 were studied by using relatively thin impactors and measuring the complete wave profile with the laser velocity interferometer. After impact, elastic and plastic waves propagate from the impact surface into both impactor and target. The waves that reach the impactor rear surface reflect as rarefaction waves, unloading the material. These unloading waves propagate across the impact surface into the target and are recorded at the target rear surface after arrival of the compressive wave.

Three unattenuated wave profiles for 6061-T6 are shown in Figure 26, one with a 6061-T6 impactor and two with fused quartz impactors. (Additional impact data are given in Table IV). All three targets had fused quartz windows on the rear face to reduce the magnitude of unloading due to reflection of the compressive wave. This prevents spall fracture in the target. The 6061-T6 impactor for test 61 was backed by Plexiglas to prevent bowing during launch and this accounts for the wave not releasing completely. Also, the measured interface velocity for these tests is slightly higher than particle velocity in the target since the impedance of 6061-T6 is slightly greater than fused quartz. Structure is evident in the release wave for all three tests, however, the development of this structure for test 61 with a 6061-T6 impactor is more complex than for tests with fused quartz impactors. This is because elastic and plastic waves spread in the 6061-T6 impactor such that all the unloading does not occur at the same time, i.e., the release wave does not start out as an abrupt pressure drop. The fused quartz impactor gives a "square" input wave to the target, with a nearly instantaneous release at the impactor-target interface. Therefore,

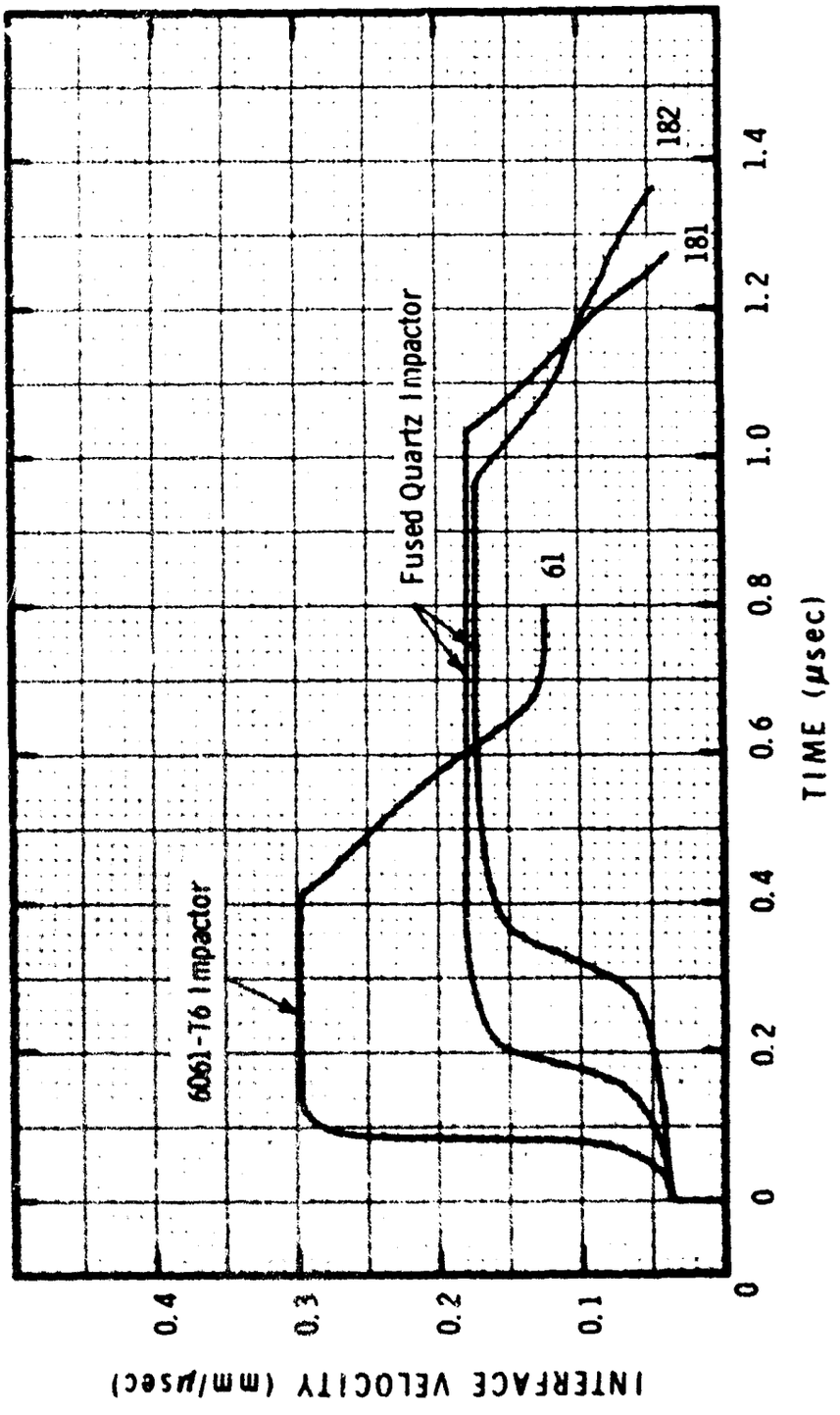

Figure 26 Complete Wave Profiles, 6061-T6

the structure in the release waves for tests 181 and 182 should be due to elastic-plastic unloading in the target material only. A shock wave attenuation study by McMillan, Isbell and Jones indicated that the initial pressure release in 6061-T6 is elastic even at pressures up to 1 mbar and the elastic release wave amplitude increases with increasing peak pressure.[73]

If target thickness is great enough compared to impactor thickness, the release wave will overtake the compressive wave and attenuate the peak stress. Wave attenuation is shown in Figure 27 for an initial stress of 20 kbar and in Figure 28 for an initial stress of 102 kbar. At the higher stress level, the impactors were backed by Plexiglas so the stress wave was not released to zero. The attenuation results are shown in Figure 29 in terms of decrease in peak stress vs. X/X_0. Also shown are calculated overtaking points assuming ideal elastic-plastic compression and release waves. This is given by:

$$\frac{X}{X_0} \approx \frac{\frac{1}{C_L} + \frac{1-u_p/U_S}{C_L^1-u_p}}{\frac{1}{U_S} - \frac{1-u_p/U_S}{C_L^1+u_p}} \qquad (25)$$

where C_L^1 is elastic release wave velocity (6.5 mm/μs for 20 kbar and 7.0 mm/μs for 102 kbar[73]).

The experimental results for 102 kbar are consistent with the calculated overtaking point, but the results for 20 kbar show attenuation much sooner than calculated. This can be attributed to the ramped plastic compressive wave at this

stress. If the velocity (~ 4.65 mm/μs) of the trailing portion of the plastic wave at 20 kbar is used for U_S rather the value (5.43 mm/μs) obtained from Equation 11, then the calculated overtaking point is X/X_0 = 4.5. This value is consistent with the experimental results for 20 kbar.

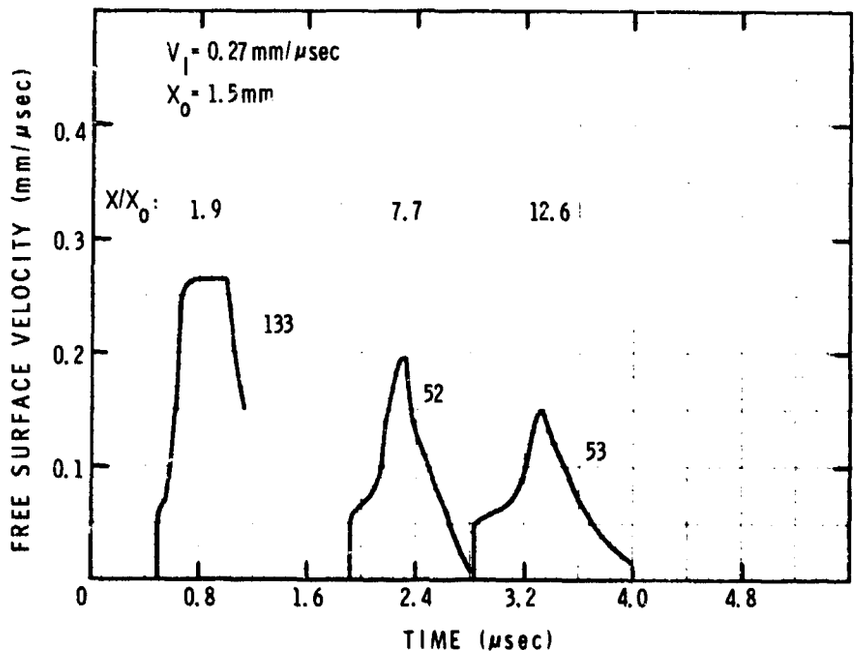

Figure 27 Wave Attenuation, Low Pressure, 6061-T6

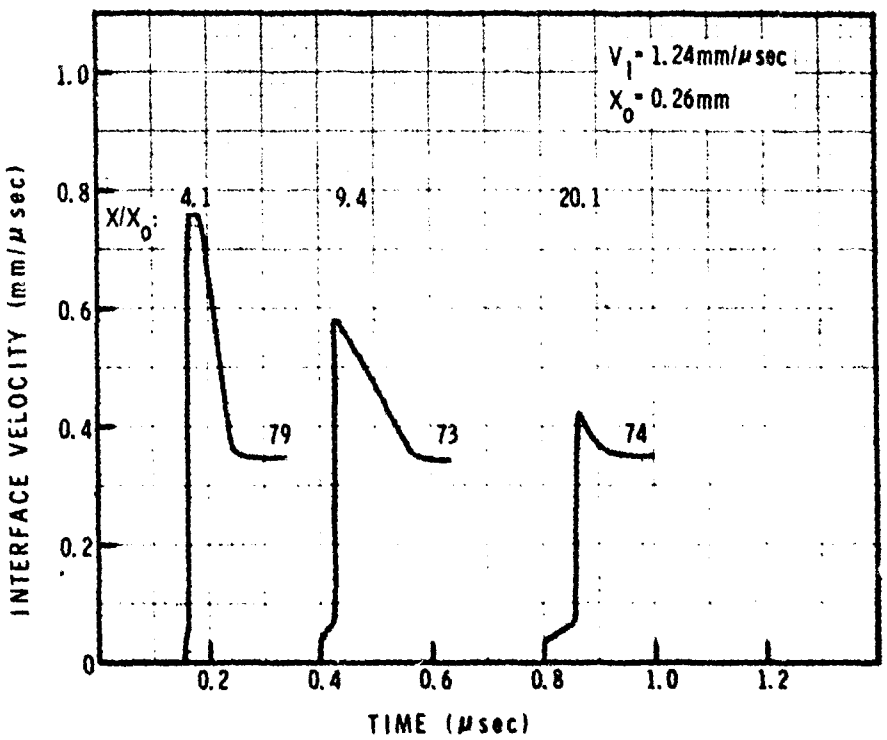

Figure 28 Wave Attenuation, High Pressure, 6061-T6

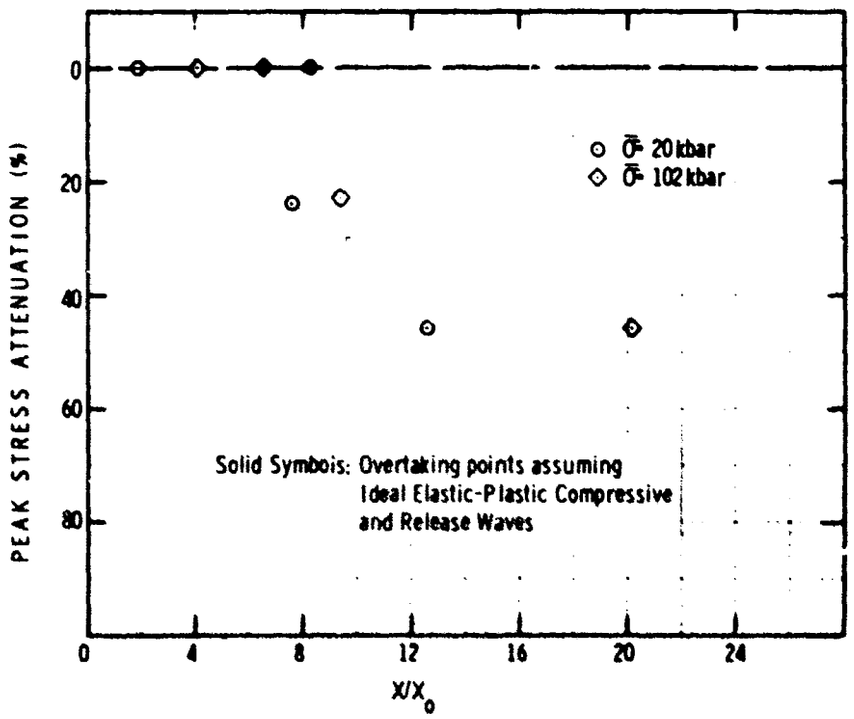

Figure 29 Peak Stress Attenuation, 6061-T6

SECTION VI

SPALL FRACTURE

Spall fracture by plate impact results from reflection of compressive waves from a relatively low impedance interface (normally a free surface) and subsequent wave interaction (see, e.g., Refs. 74-76). Spall studies were carried out with both passive and active techniques. Passive methods involve the recovery and examination of shock-loaded specimens. Metallographic examination establishes the type and degree of damage, which can be correlated with test parameters such as velocity, impactor thickness and target thickness. Active methods utilize the laser velocity interferometer and provide quantitative, time-resolved data on the influence of internal fractures or spall surfaces on shock wave profiles, as measured at the rear surface.

RECOVERY TESTS

The spall behavior of 6061-T6 was studied by carrying out a series of impact and recovery tests, where the target was sectioned across a diameter, polished, etched, and examined optically at a magnification of 50X. The specimens were then graded or classified according to the degree of fracture that was observed, which ranged from no visible damage to complete material separation. The onset of significant fracture is generally referred to as incipient spall and is a critical point since it can be used to deduce the dynamic fracture strength, and corresponds to generation of sufficient free

surfaces within the material to reflect a portion of the interacting release waves as a compressive wave. The incipient spall threshold was defined as the impact velocity (for a given set of impact parameters) corresponding to cracking over at least 50% of the width of the section estimated to be under a condition of plane strain during the time of loading.

Incipient spall results from all tests, including an attenuated pulse series and elevated temperature tests, are summarized in Table V. The data for all 20°C tests with unattenuated pulses ($X/X_0 \simeq 2$) are given in Figure 30. The symbols are defined as:

- ● Complete Separation
- ◓ Above Incipient
- ◒ Incipient Spall
- ◒ Below Incipient
- O No Visible Damage

As is typically the case with metals, the impact velocity for incipient spall increases for decreasing impactor thickness. This implies that peak stress (and, therefore, strain) required to create spall fractures increases with decreasing pulse width or time of loading. These results are compared to those of Kreer[77] and Butcher, et al.[74] in Figure 31. These data are all for gun-launched, plate-impact techniques.* Although Butcher's tests were for $X/X_0 = 4$, a comparison with data for

* Spall in 6061-T6 has been studied by Keller and Tuler[78], Jajosky and Ferdman[79] and Cohen and Berkowitz[80], using exploding-foil techniques; however, their results are not included here since differences in experimental method, condition of the impactors and metallographic analysis prevent a direct comparison. Also, Stefansky and Shea[81] studied dynamic fracture in several metals, including 6061-T6, using electron beam pulses.

TABLE V

INCIPIENT SPALL DATA FOR 6061-T6 ALUMINUM

X_0 Impactor Thickness (mm)	X Target Thickness (mm)	X/X_0	T Temperature (°C)	Δt_e Pulse* Width (μs)	V_S Spall Velocity (mm/μs)
0.25	0.48	1.92	20	0.079	0.262
0.47	1.01	2.15	20	0.148	0.220
1.55	3.02	1.95	20	0.49	0.190
1.55	3.02	1.95	288	0.49	0.172
1.55	3.02	1.95	400	0.49	0.130
2.80	5.52	1.97	20	0.88	0.175
4.00	8.08	2.02	20	1.26	0.165
4.00	8.08	2.02	288	1.26	0.150
0.46	4.02	8.74	20	0.144	0.355
1.55	5.84	3.77	20	0.49	0.200

* $\Delta t_e = \frac{2X_0}{C_L}$

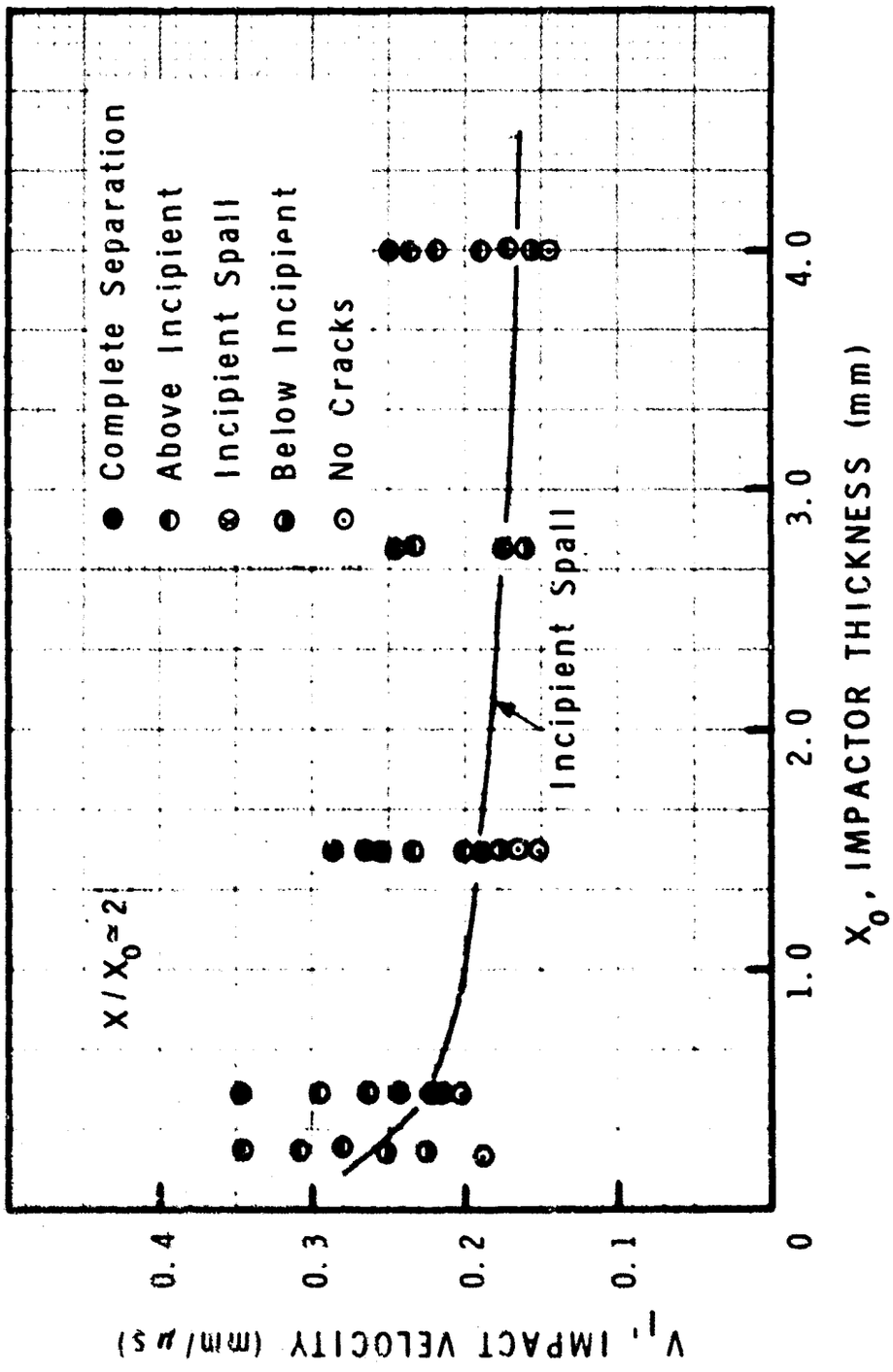

Figure 30 Spall Data, 6061-T6

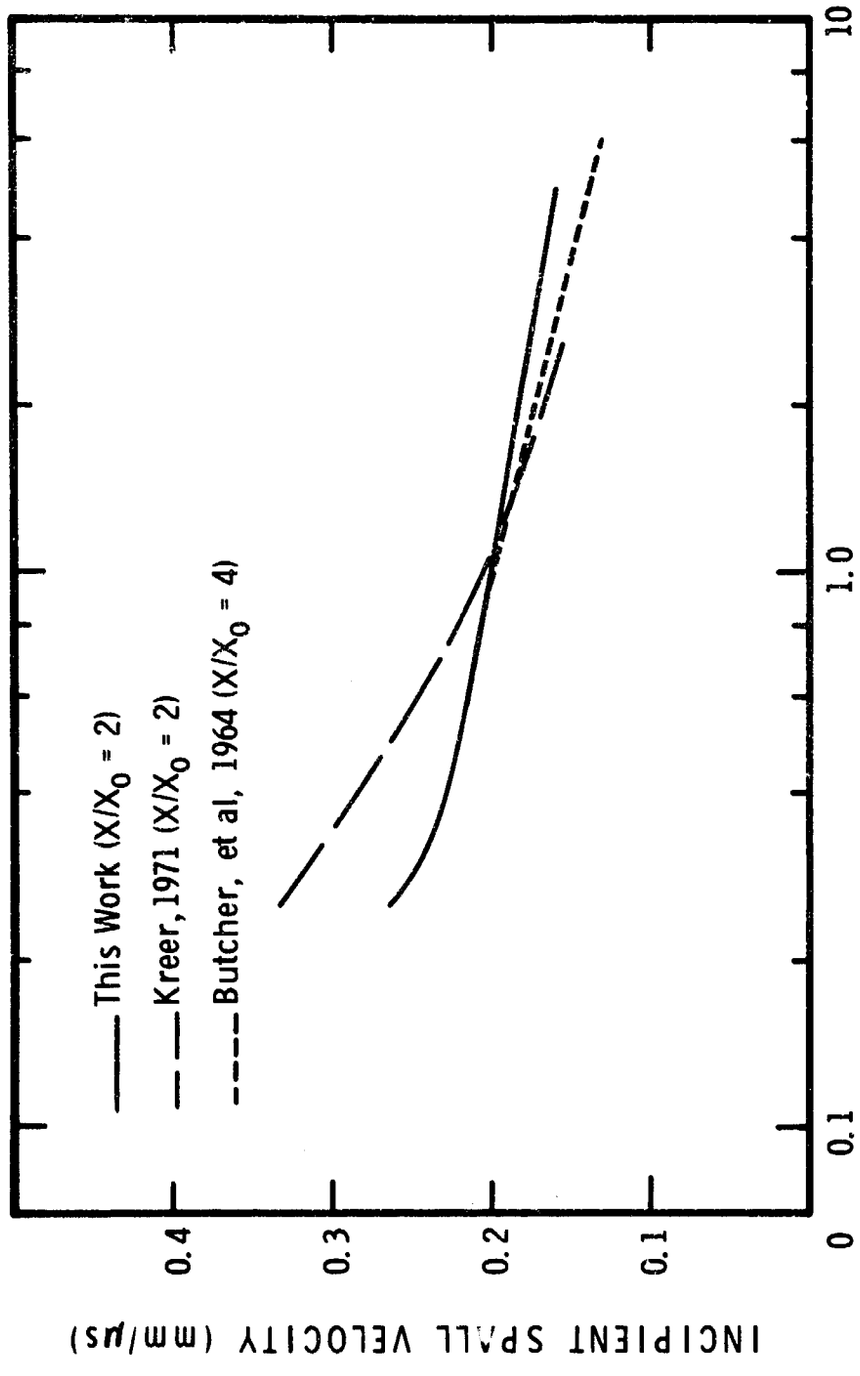

Figure 31 Spall Data Comparison, 6061-T6

$X/X_0 = 2$ is valid since the incipient spall threshold in 6061-T6 increases only ∿ 5% for a change in $X/X_0 = 2$ to $X/X_0 = 4$, as shown in Figure 32. The data given in Figure 31 show reasonable agreement for $X_0 > 0.8$ mm. For thinner impactors, however, the data from this work and that of Kreer deviate significantly. This may be due to differences in experimental techniques (e.g., impactor bowing, tilt, target construction or metallographic methods); although Kreer indicates that material property variation may also be a cause.

Optical photomicrographs of recovered specimens are shown in Figures 33 to 35.* The specimens were polished and etched to provide maximum contrast between cracks and sound material. The procedure followed was:

1. Wet grind, 320/400/600 grit silicon carbide paper.
2. Rough polish, 5 μm aluminum oxide slurry on rayon cloth.
3. Final polish, 0.05 μm gamma alumina slurry on rayon cloth.
4. Etch, 10 ml hydrofluoric acid (HF), 15 ml hydrochloric acid (HCl) and 90 ml water, 30-90 sec immersion (20°C), wash in warm water.

As noted above, spall cannot be rigorously defined in terms of a unique impact velocity or stress, but requires consideration of the degree of fracture. In general, as impact velocity increases, spall progresses from isolated cracks or voids only a few grains in size to complete material separation across the entire spall plane.

* All spall photomicrographs in this report are oriented such that initial shock wave propagation was from bottom to top.

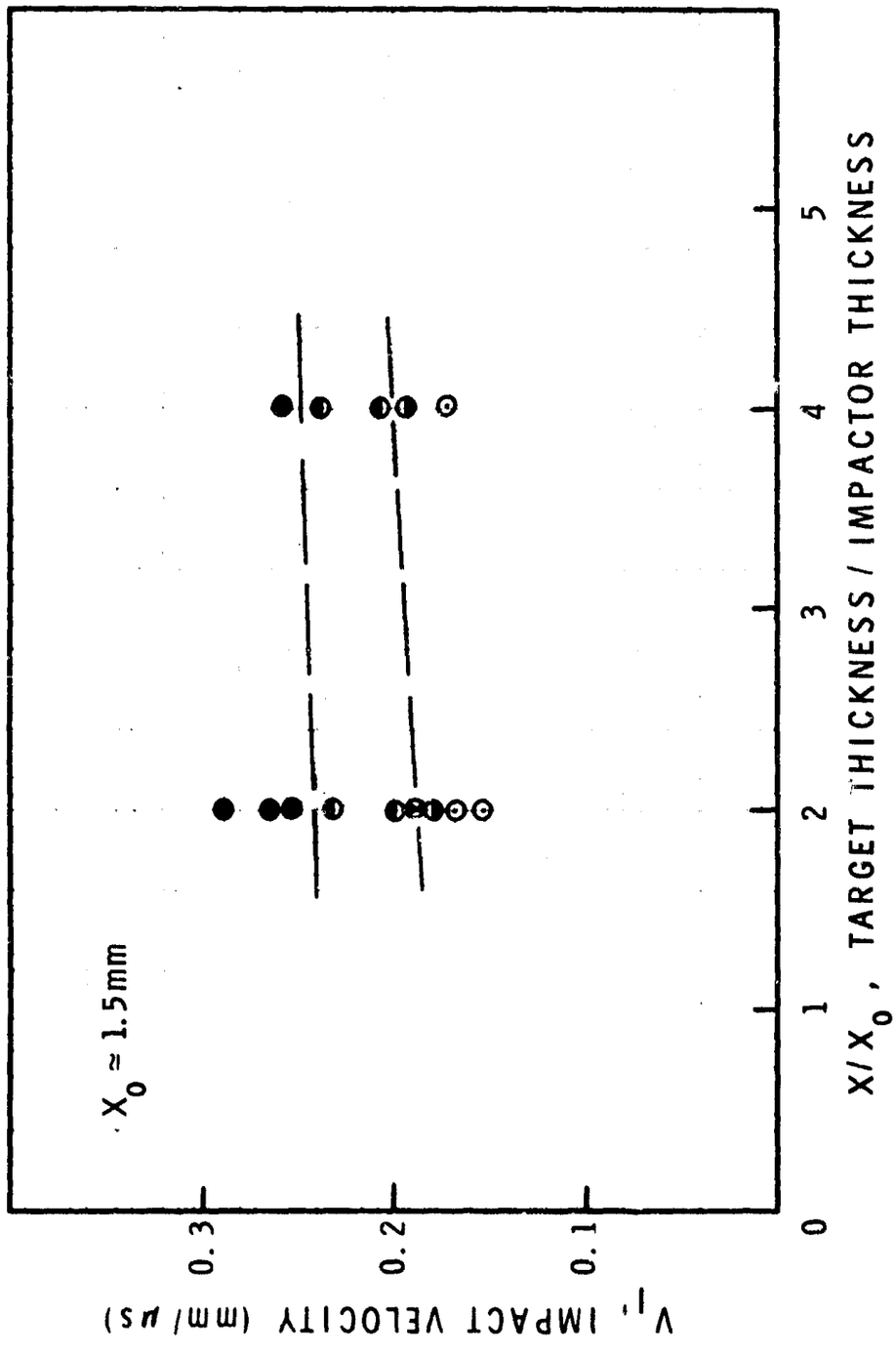

Figure 32 Spall Data, Thickness Ratio Dependence, 6061-T6

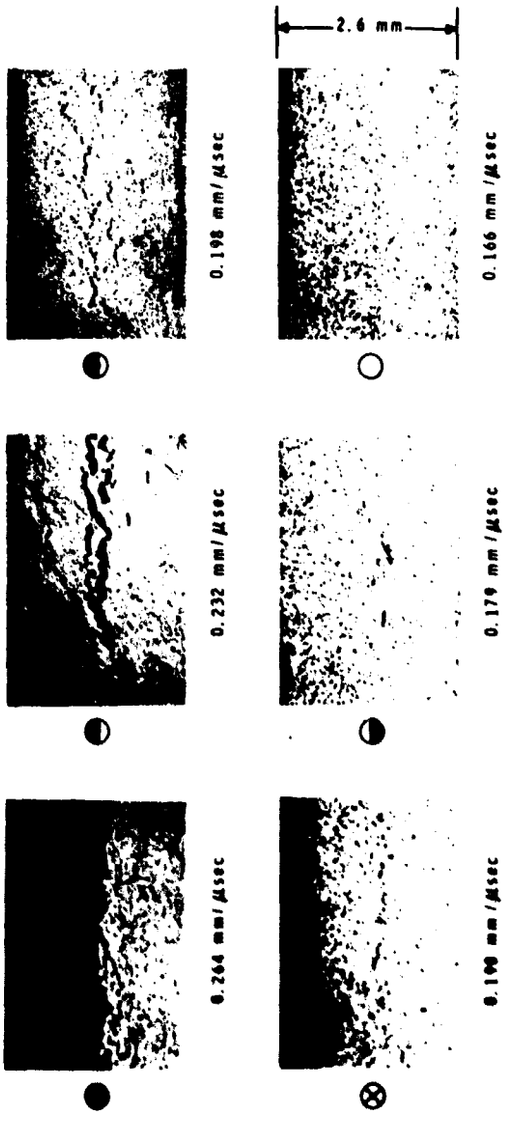

Figure 33 Spall Fractures, 6061-T6

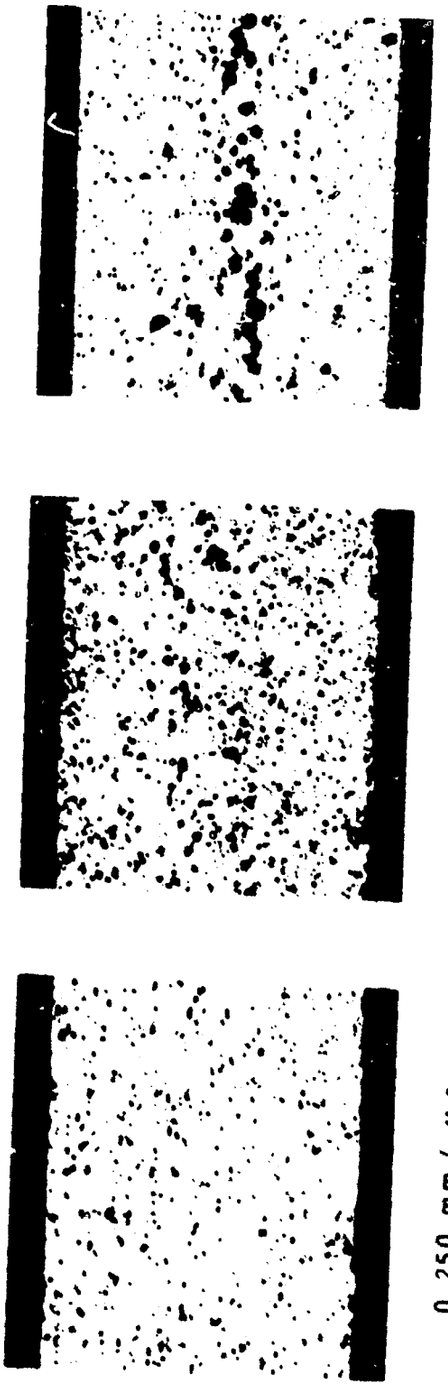

Figure 34 Spall Fractures, 6061-T6 (0.25 mm → 0.48 mm, 20°C)

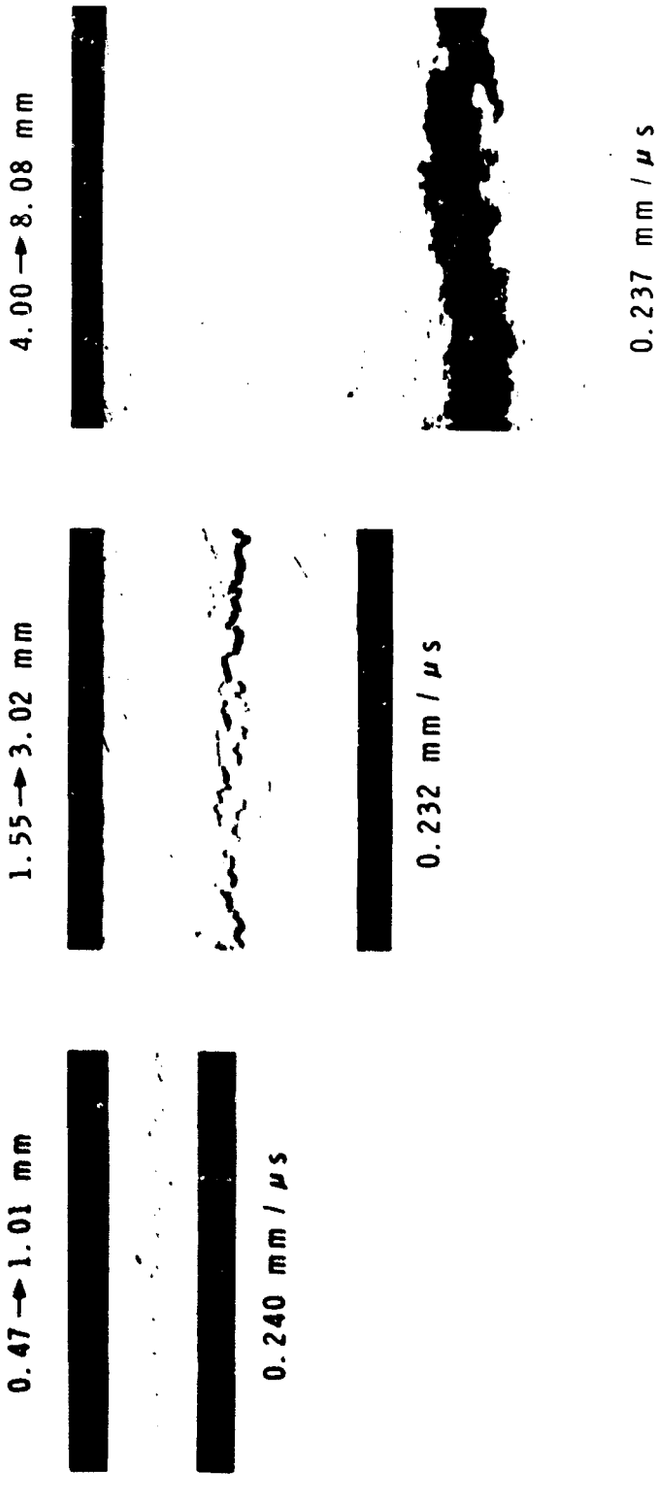

Figure 35 Spall Fractures, 6061-T6 (20°C)

Fracture in 6061-T6 is of a ductile nature with the development of individual voids. As velocity increases (see, e.g. Figures 33 and 34) the voids begin to coalesce and a complete fracture surface is formed. Note that there is some dispersion of the voids around a nominal "spall plane". This was also found for titanium[82] and tantalum[83], which have well-defined elastic wave structures, while copper[84] has a poorly-defined, low-amplitude elastic wave and showed very little void dispersion around the spall plane. Spall fractures in the four metals are compared in Figure 36.

Scanning microfractographs of the fracture surfaces for completely separated specimens are shown in Figures 37 and 38. The voids appear to have initiated at brittle particles (precipitates or second-phase particles) which are visible in the center of the voids. Some of the particles themselves appear to be fractured, an observation previously report by Au[85] for 6061-T6. Complete fracture has been primarily by normal rupture with evidence of shearing near the necked or peripheral areas of the voids. There was essentially no difference in fracture surface for specimens taken from different stock (see Figure 38). Tuler[86] reported essentially no change in fracture surface in 6061-T6 for failure due to slow bending, charpy impact and plate impact.

Several tests were conducted to determine the effect of preshocking on spall behavior. A target was assembled with radial and rear momentum traps and subjected to a 20 kbar, 0.5 μsec compressive pulse. The recovered specimen was then tested at a velocity which caused spall in a specimen that had not been preshocked. Results are compared in Figure 39. Apparently, preshocking has increased the spall fracture strength, since the unshocked specimen shows spall fractures while the preshocked specimen does not, for the same test conditions.

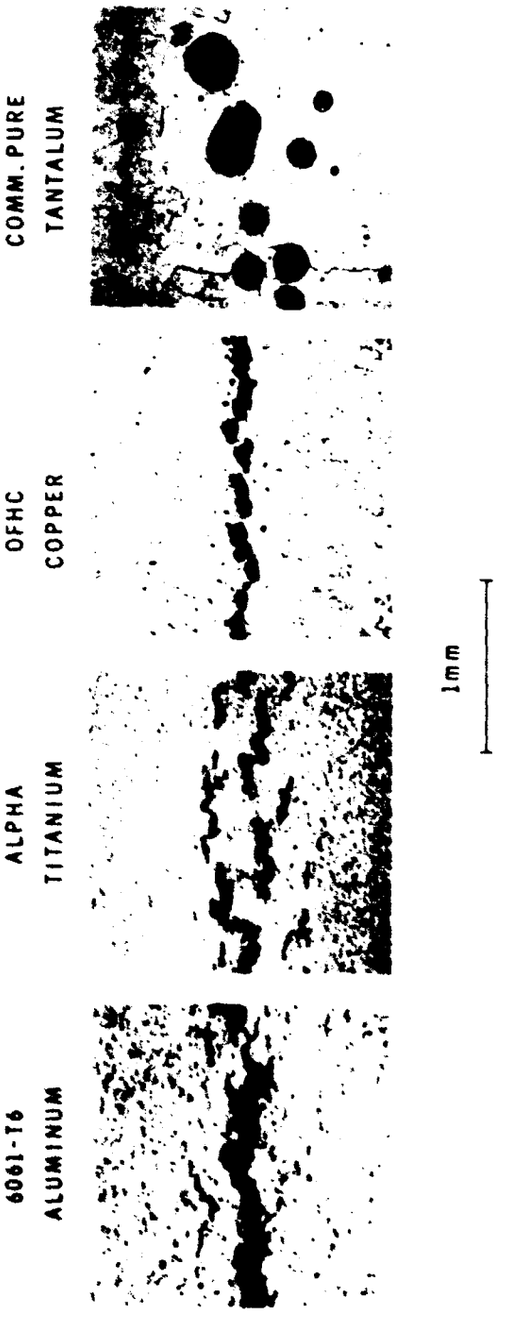

Figure 36 Spall Fractures in Metals

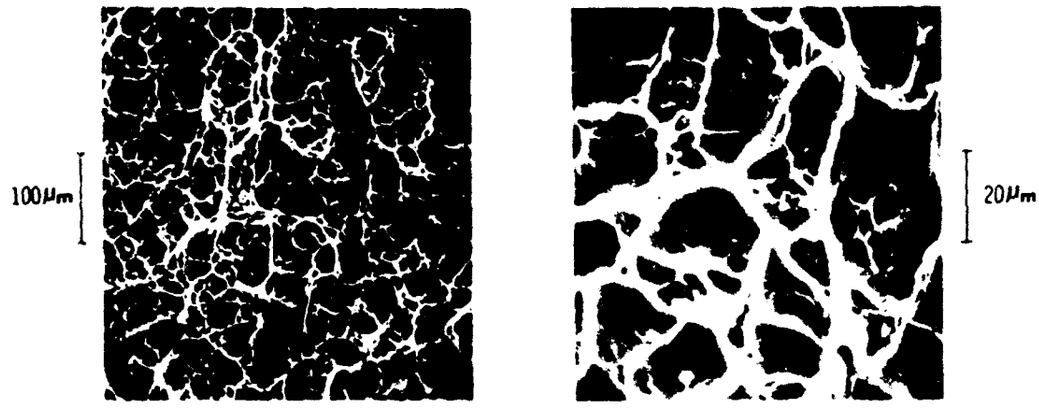

Figure 37 Spall Fracture Surface, 6061-T6 (20°C)

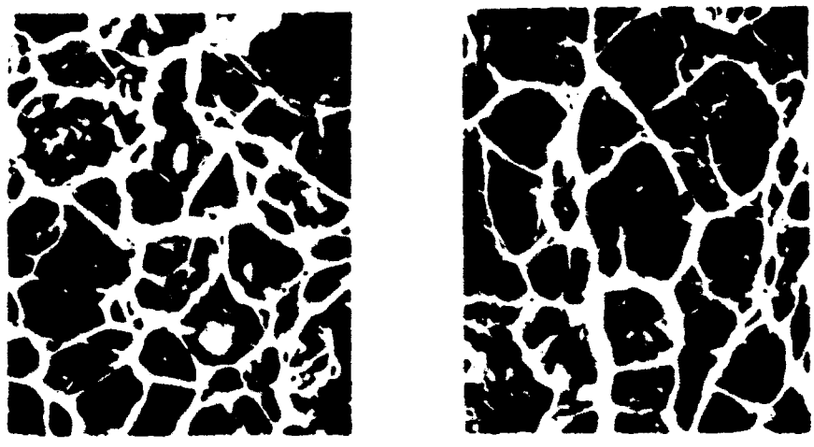

Figure 38 Spall Fracture Surfaces, Material Effect, 6061-T6 (20°C)

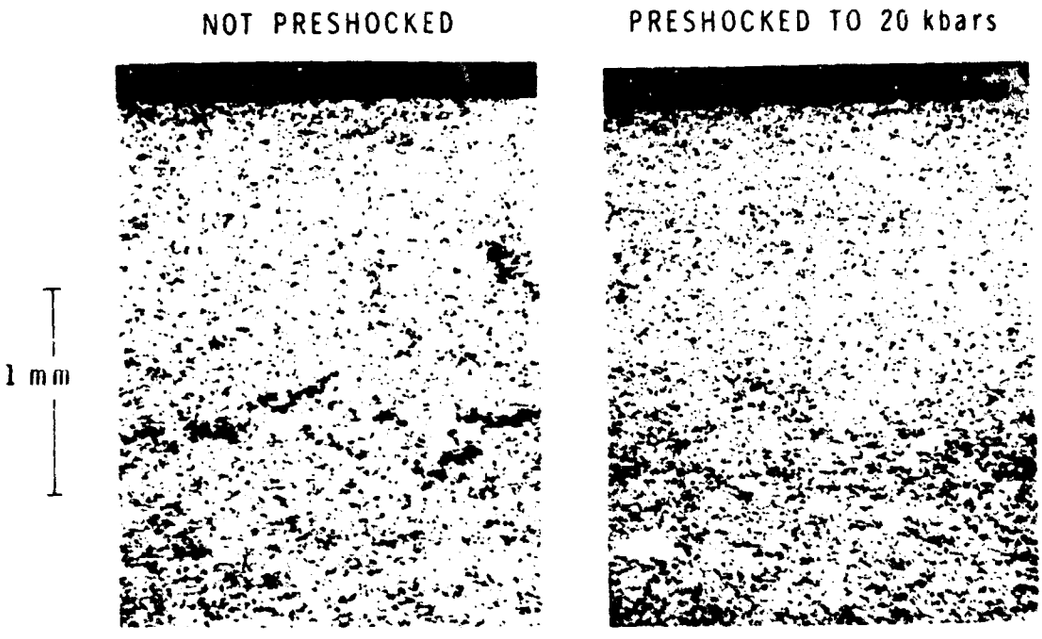

Figure 39 Spall Fractures, Preshocking Effect, 6061-T6 (20°C)

Stevens and Tuler[87] studied the influence of varying amounts of precompression on spall fracture by backing the target with a material of lower impedance (rather than a free rear surface). They reported that increasing the precompression stress from 12 to 82 kbar did not significantly change the calculated incipient spall tensile stress.

Temperature dependence of spall for 6061 is given in Figure 40. The impact velocity for incipient spall decreases with increasing temperature. This behavior is probably related to changes in the dynamic fracture strength of the material. However, as

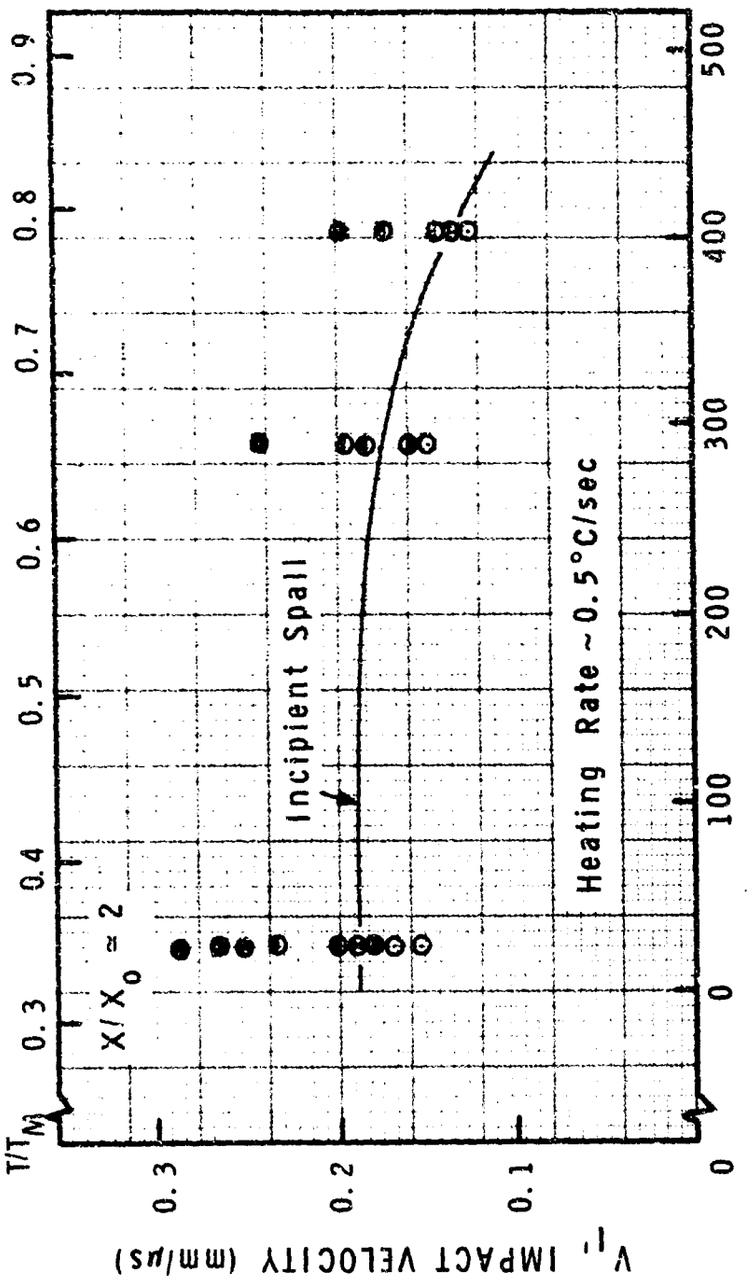

Figure 40 Spall Data, Temperature Effect, 6061

Charest has pointed out[88], the use of a room temperature impactor and a hot target (as was done here), gives impedance differences that influence development of the release wave structure and therefore stress-time history in the target. Also, the reduced hugoniot elastic limit in 6061 at elevated temperature will affect the wave structure in the target. Optical photomicrographs and scanning microfractographs of 6061 spall specimens tested at several temperatures are shown in Figures 41 and 42. Although the impact velocity required for incipient spall and for complete separation has decreased, there has been no appreciable change in the appearance of voids or fracture surface.

Several specimens were annealed by heating at 400°C for three hours and then tested at 20°C. The incipient spall threshold was ∿ 0.145 mm/μsec or ∿ 25% less than 6061-T6 for the same thickness. This is comparable to the difference reported by Butcher[89] for "-T6" and "-0" condition material. Optical photomicrographs of 6061-0 spall specimens are shown in Figure 43, and spall fracture surfaces of 6061-0 and 6061-T6 are compared in Figure 44.

SPALL PROFILES

Spall wave profiles were studied using an aluminum-into-aluminum configuration, with a free rear surface on the target for complete reflection of the compressive front. A schematic of the wave interactions resulting from such a test in shown in Figure 45. Several simplifying assumptions are made. The shock is shown as a single wave and the release waves originating at boundaries are considered simple, centered rarefaction fans.

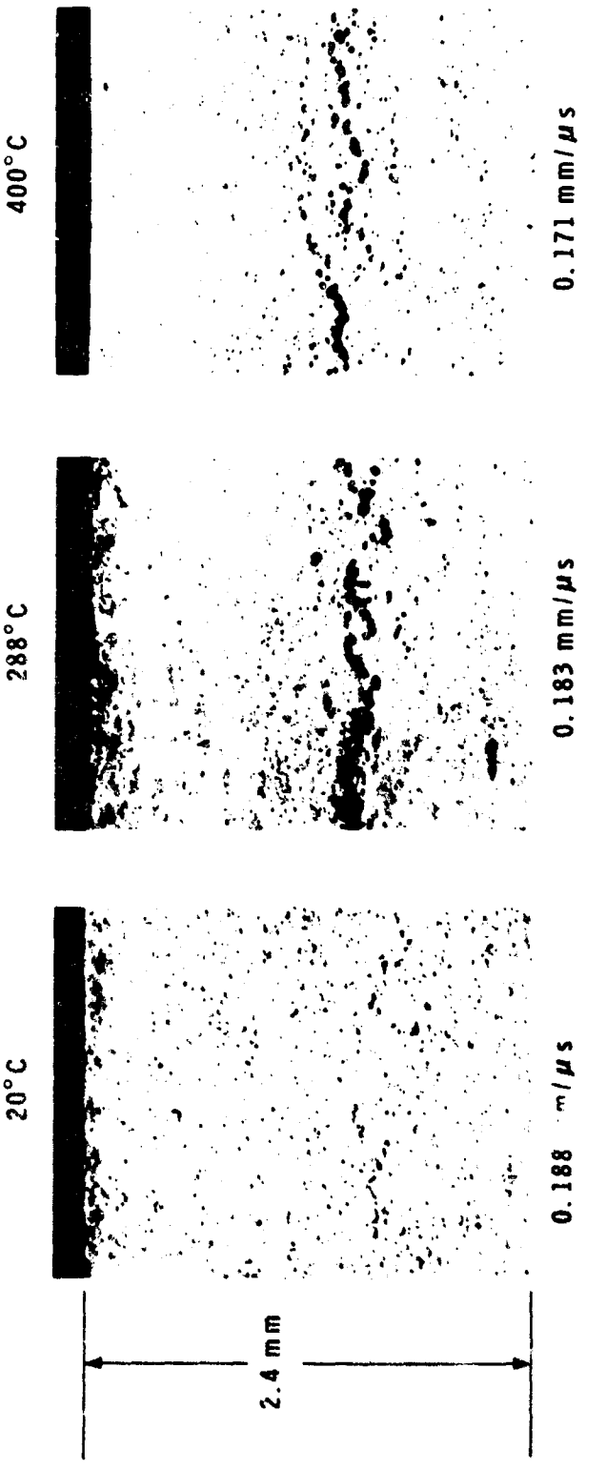

Figure 41 Spall Fractures, Temperature Effect, 6061

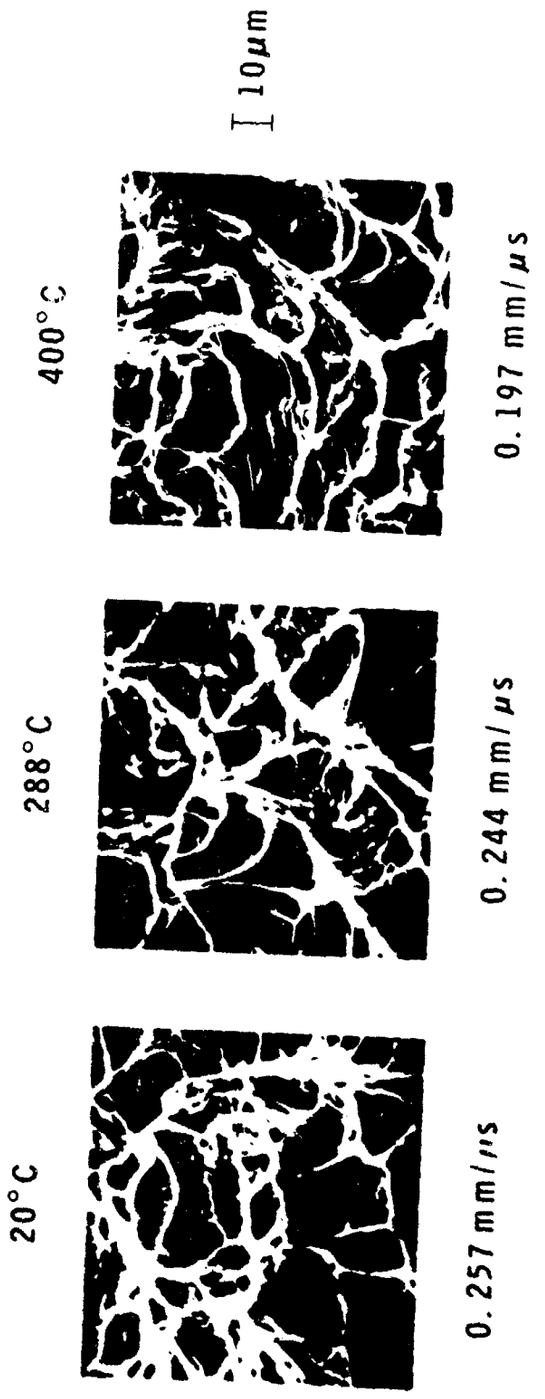

Figure 42 Spall Fracture Surfaces, Temperature Effect, 6061

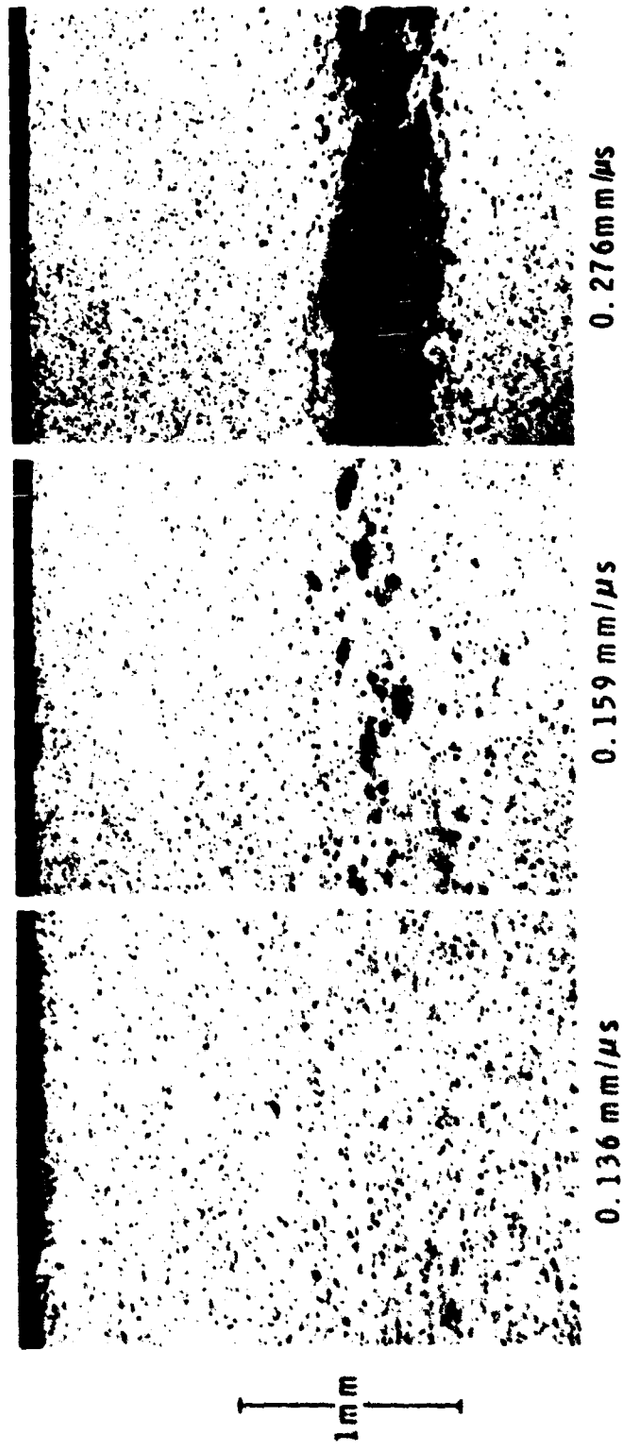

Figure 43 Spall Fractures, 6061-0 (1.5 mm → 3.0 mm, 20°C)

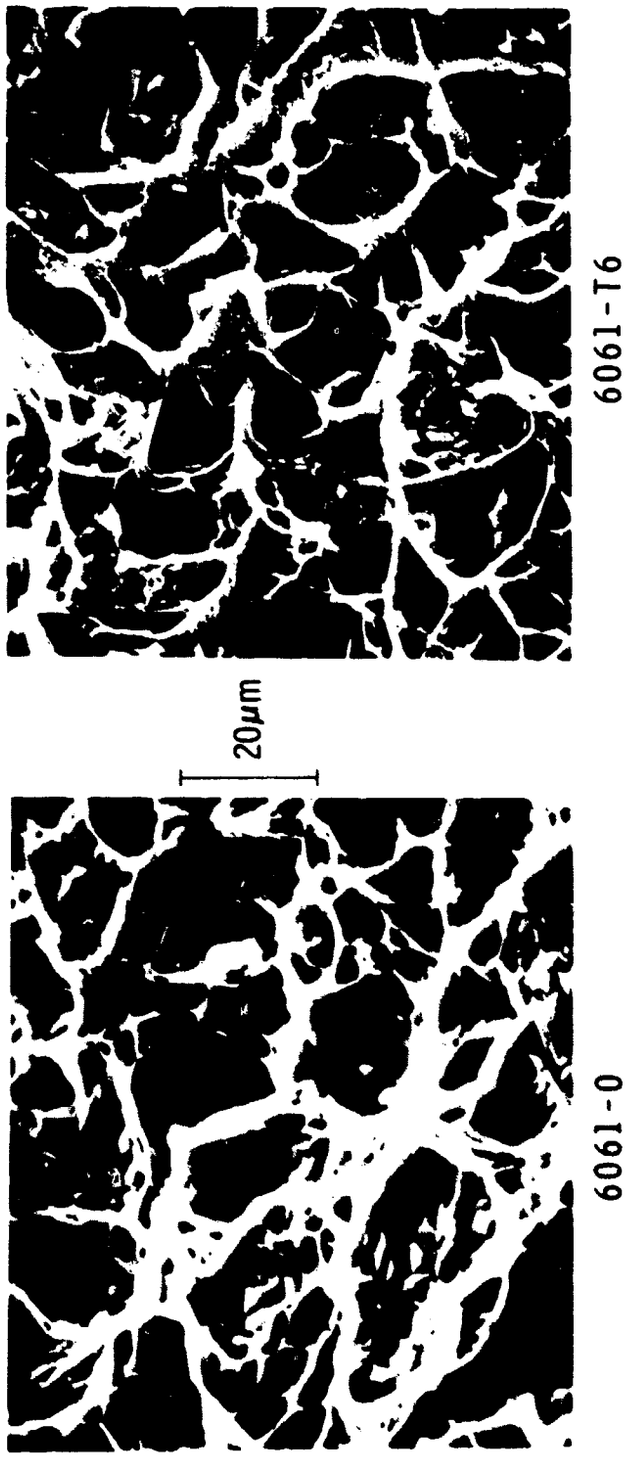

Figure 44 Spall Fracture Surfaces, Annealing Effect

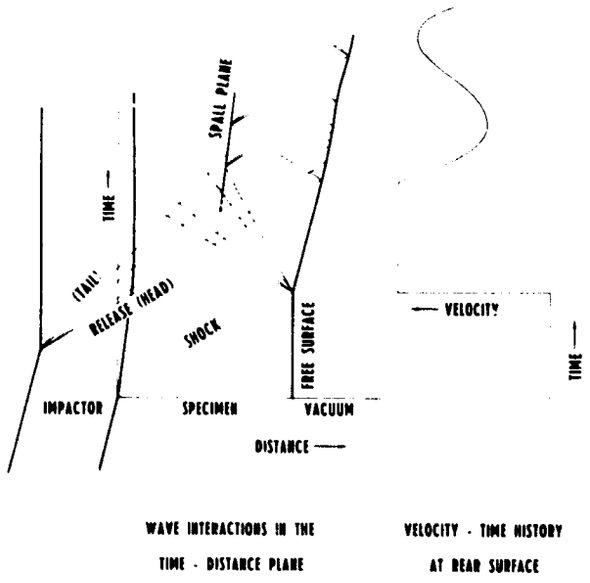

Figure 45 Wave Interaction Schematic, Spall Test

Also, small interactions between shock waves have been omitted. Fracture of the material is assumed to occur along a single surface (spall plane) rather than in a volume around this plane (see Figure 33). Wave interactions at the spall plane are shown as if the material exhibits a time-dependent fracture, i.e., the percentage of fractured area in the spall plane increases with time until the entire spall surface has separated. During the early stages of the fracture process, before complete separation is achieved, waves crossing the spall plane are partially transmitted and partially reflected. After complete separation has occurred, any waves trapped in the spalled piece reverberate, giving a sinusoidal motion to the rear surface, which eventually damps out due to attenuation and dispersion in the material and to the effects of edge rarefactions.

Measured profiles for unattenuated pulses in 6061-T6 are shown in Figure 46, with photomicrographs of the recovered and sectioned targets. Also shown for reference are the incipient and complete spall levels for this impactor/target combination as determined from the recovery tests. Evidence of fracture in the target is shown as a reversal of the measured release wave. The amount of pullback (decrease in free surface velocity to the point of first reversal) may be related to the tensile strength at the spall plane of the material for a given impact geometry. An empirical relation for this is given by:[90]

$$\sigma_s = \rho C(\Delta u_{fs}/2) \qquad (26)$$

where σ_s is tensile strength, ρ and C are local density and longitudinal wave speed, and Δu_{fs} is pullback.

The data in Figure 46 give $\sigma_s \simeq 12$ kbar. This calculated spall strength is not constant for a given material since it is proportional to Δu_{fs} which has been found to change with such factors as pulse width (see Figure 47), target temperature* (see Figure 48), and pulse shape (see Figure 49). These factors are discussed in detail in Reference 92. However, for a given set of impact conditions (thickness, material, temperature), the pullback is relatively insensitive to the maximum compressive stress as well as to the degree of fracture, as shown in Figure 50. This is consistent with the varying-precompression results of Stevens and Tuler[87] referred to earlier.

* Brammer[91] reported spall profiles for 2024 Aluminum at 22°C and 371°C which also showed a decrease in pullback at the higher temperature.

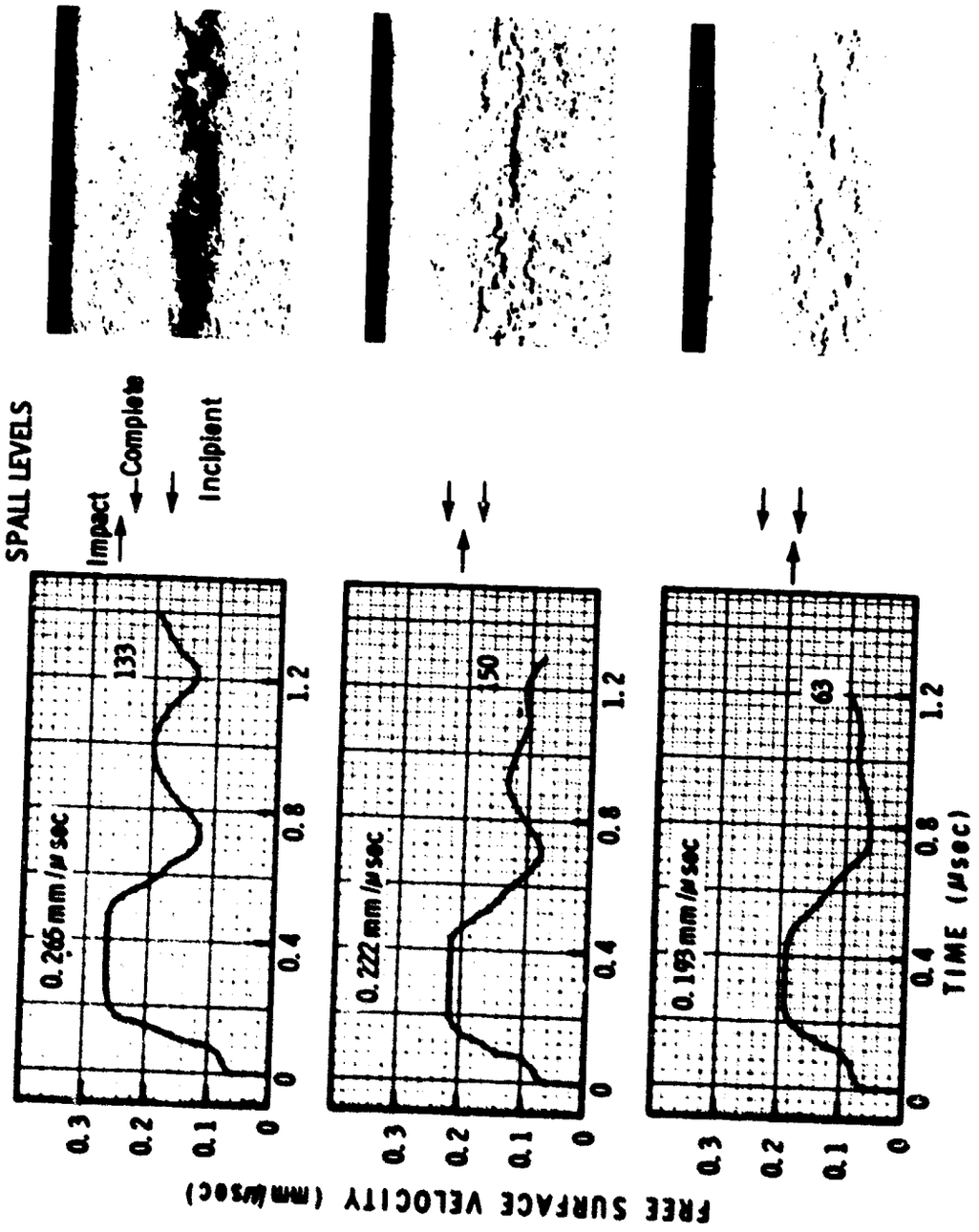

Figure 46 Spall Wave Profiles, 6061-T6

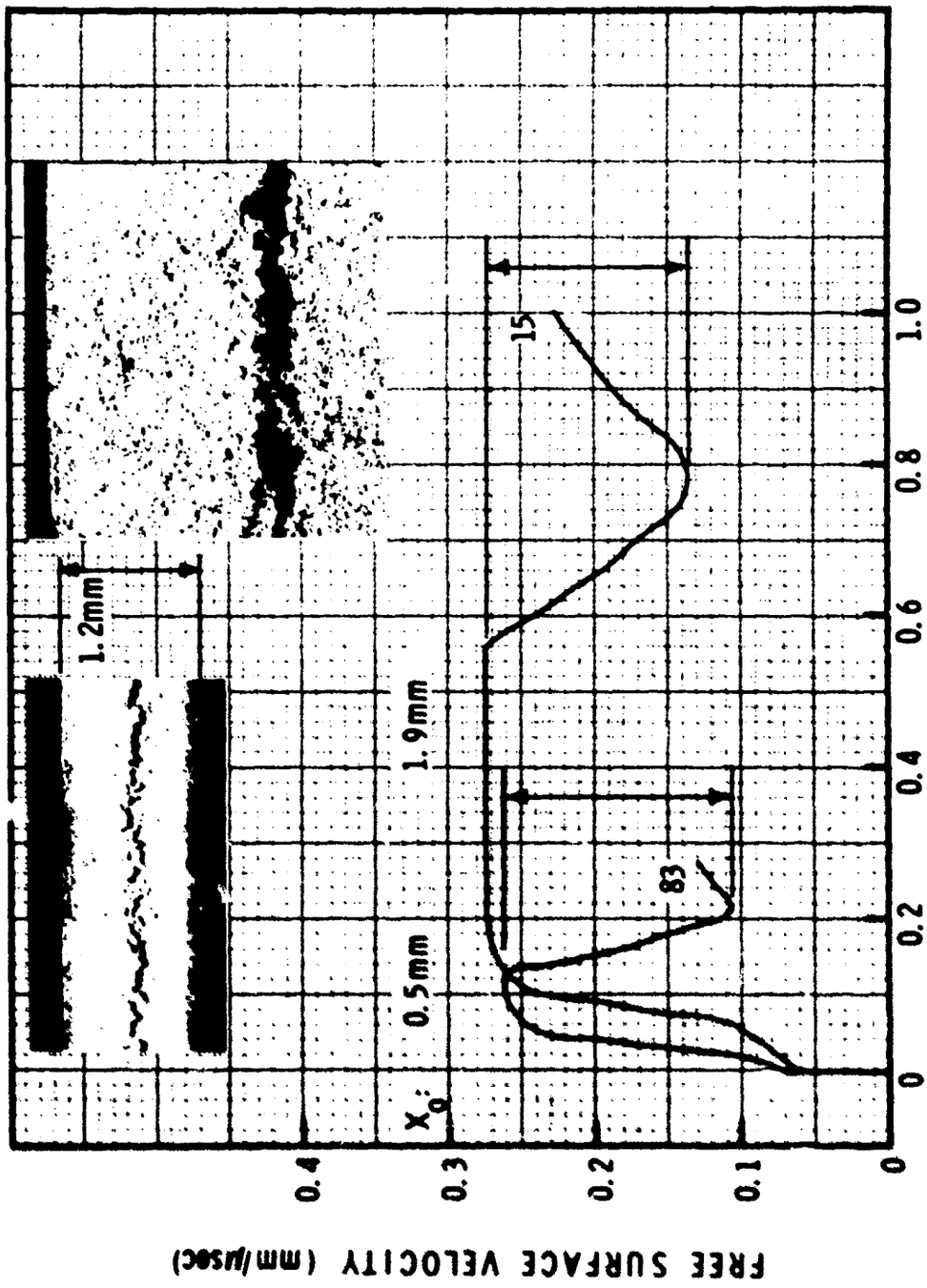

Figure 47 Spall Wave Profiles, Pulse Width Dependence, 6061-T6

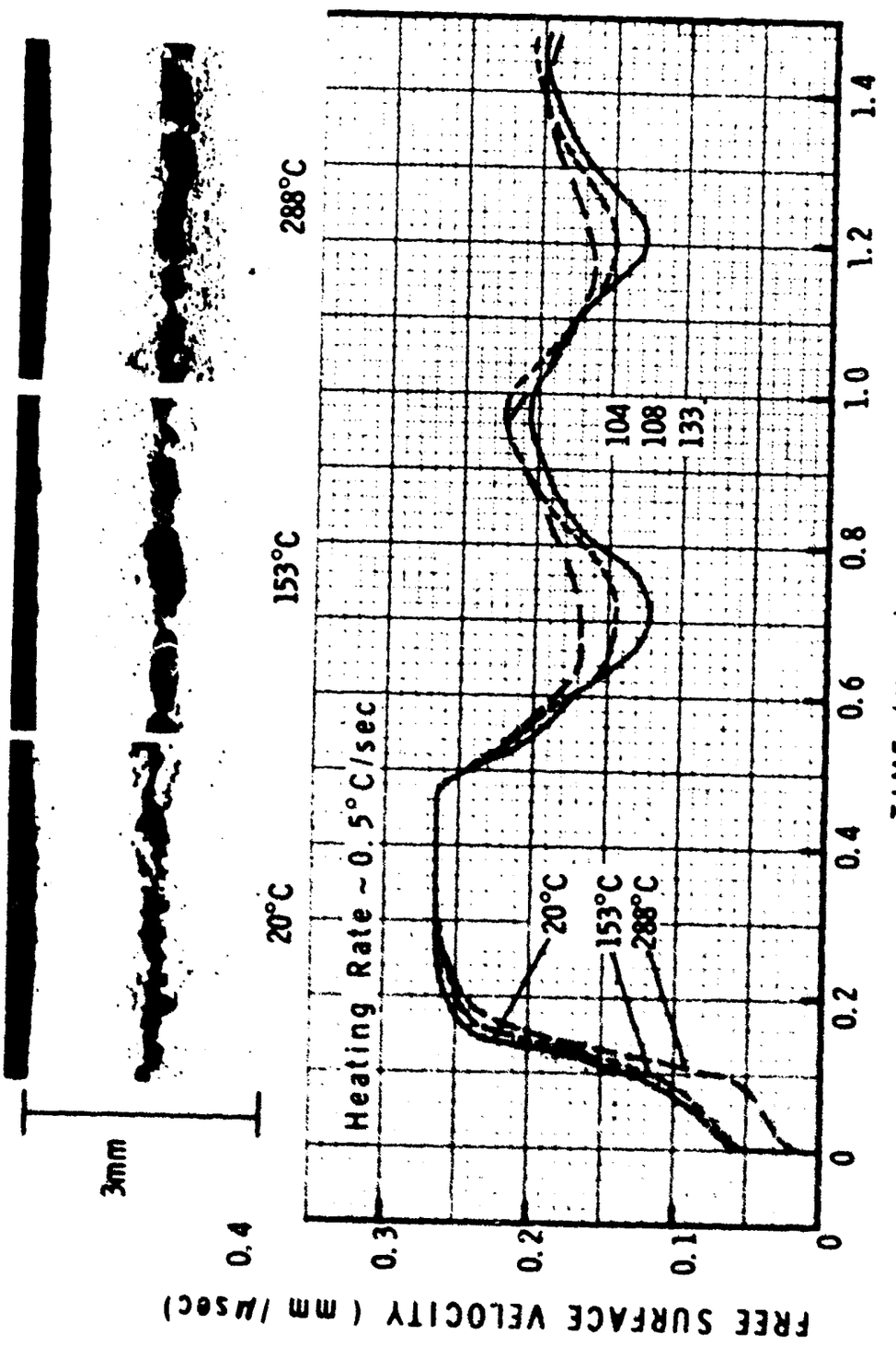

Figure 48 Spall Wave Profiles, Temperature Dependence, 6061

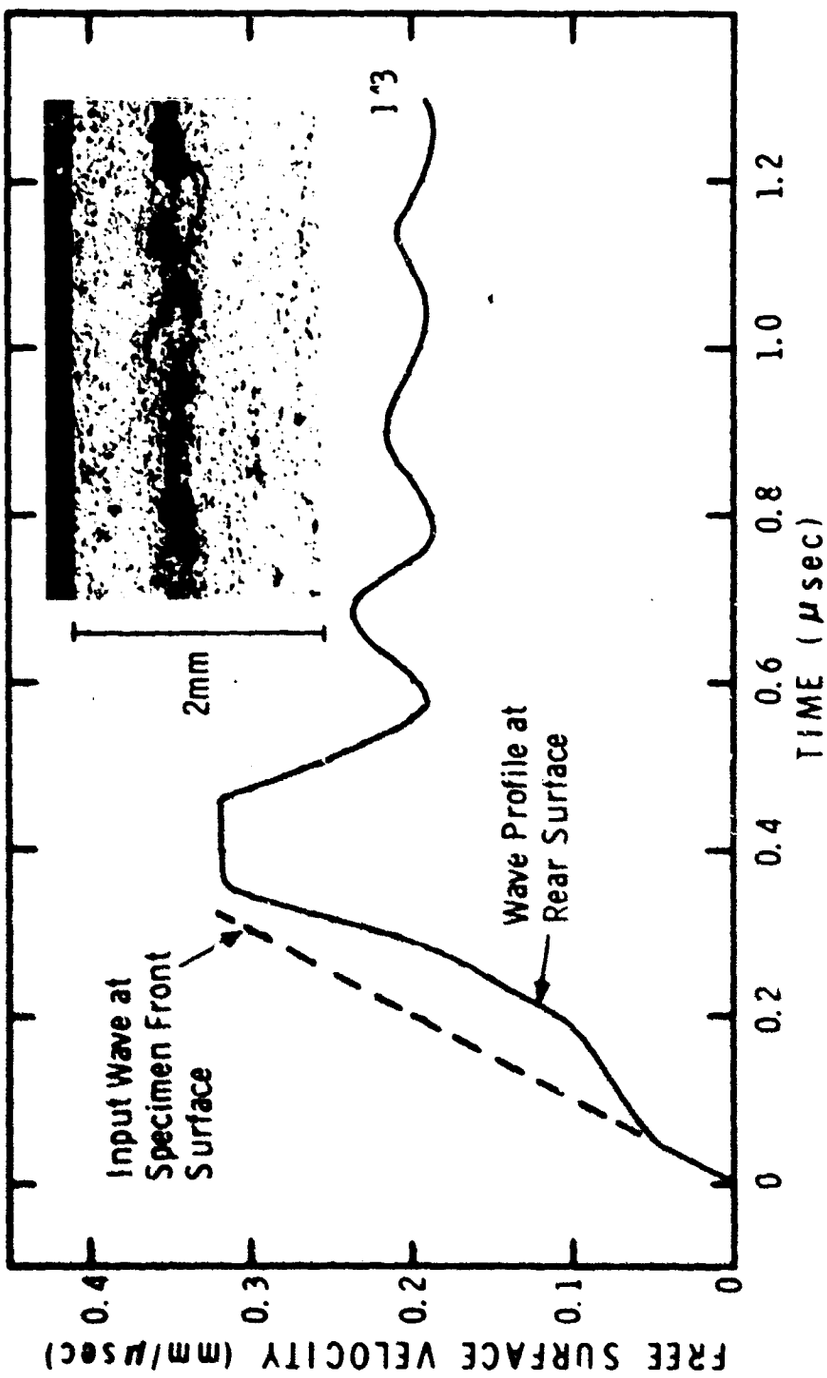

Figure 49 Ramped-Wave Spall Profile, 6061-T6

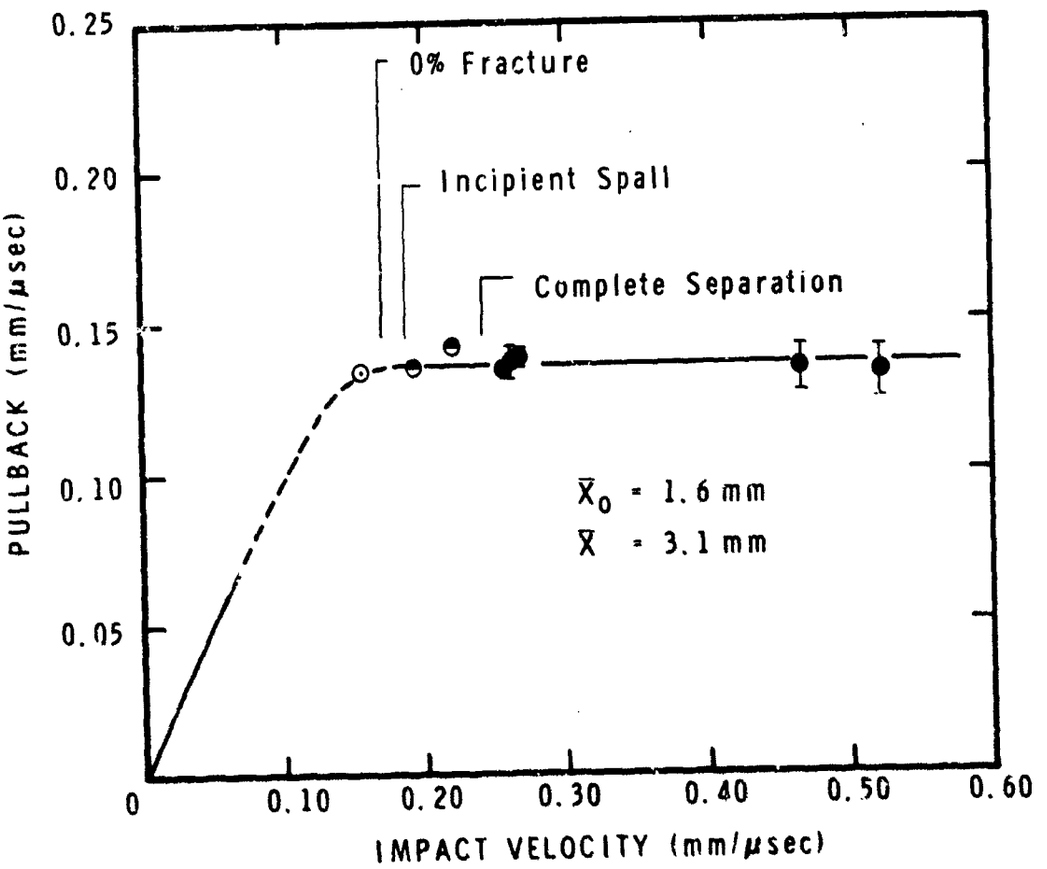

Figure 50 Pullback vs. Impact Velocity, 6061-T6

In the elastic range, pullback equals impact velocity, while at impact velocities causing fracture, the pullback is approximately 0.135 mm/μsec (independent of degree of fracture and maximum stress). Thus, the pullback appears to be associated with the incipient spall threshold, i.e., the formation and initial coalescence of voids in the material, rather than with complete fracture or separation. This conclusion may allow comparison of the dynamic fracture strength of the material over a range of wave shapes and times of loading without the necessity of conducting all tests with exactly the same degree of final fracture. An additional benefit may result if the pullback can be related to the results of the recovery-type measurements of the incipient spall threshold. Then a single wave profile test could, for a given set of initial conditions, provide the same incipient threshold data as a series of recovery tests. This data could be of use in evaluating various spall fracture models through comparison of measured shock wave/spall plane interactions with calculated wave profiles.[93-99]

The influence of spall plane strength was studied with a target having an "artifical" spall plane of essentially zero strength. This zero-strength plane was actually the interface between two target plates bonded together with a thin (< 5 μm) epoxy layer having a tensile strength of ∿ 0.01 kbars. The rear target plate was the same thickness as the impactor, putting the interface at the nominal spall plane. Referring to Figure 51, for a single wave system the free surface velocity would be expected to increase abruptly to the impact velocity. The momentum of the impact is simply transferred to the spall piece. For a two-wave system, the momentum transfer will again take place. However, the interactions at the interface are now more complicated and a net tensile stress may develop

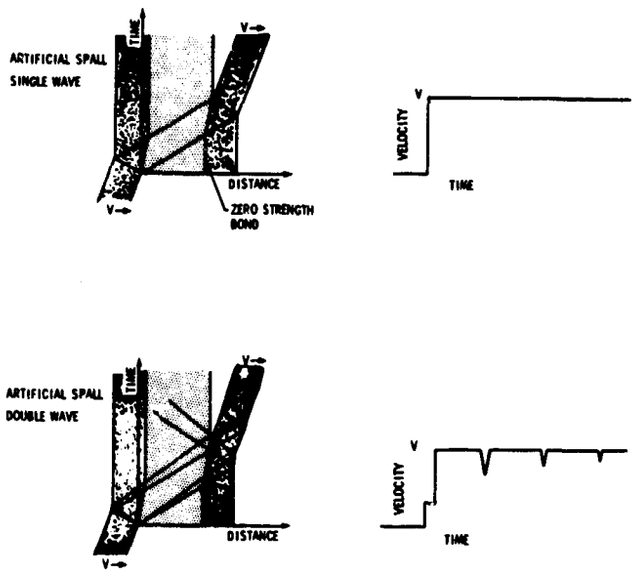

Figure 51 "Zero-Strength" Spall Behavior Schematic

in the spall piece. The pullback at the rear surface shows evidence of this tensile pulse. Figure 52 shows the measured wave profile for such a test. The ringing in the spall piece continues for many microseconds. The damped pullback apparently will decrease to zero amplitude and the piece will continue with approximately impact velocity.

Spall profiles for attenuated pulses, where the time duration of the peak tensile stress is expected to be less than for the unattenuated case, are shown in Figure 53. The pullback for this case is 0.175 mm/μsec, giving a spall strength of ∿ 15 kbar.

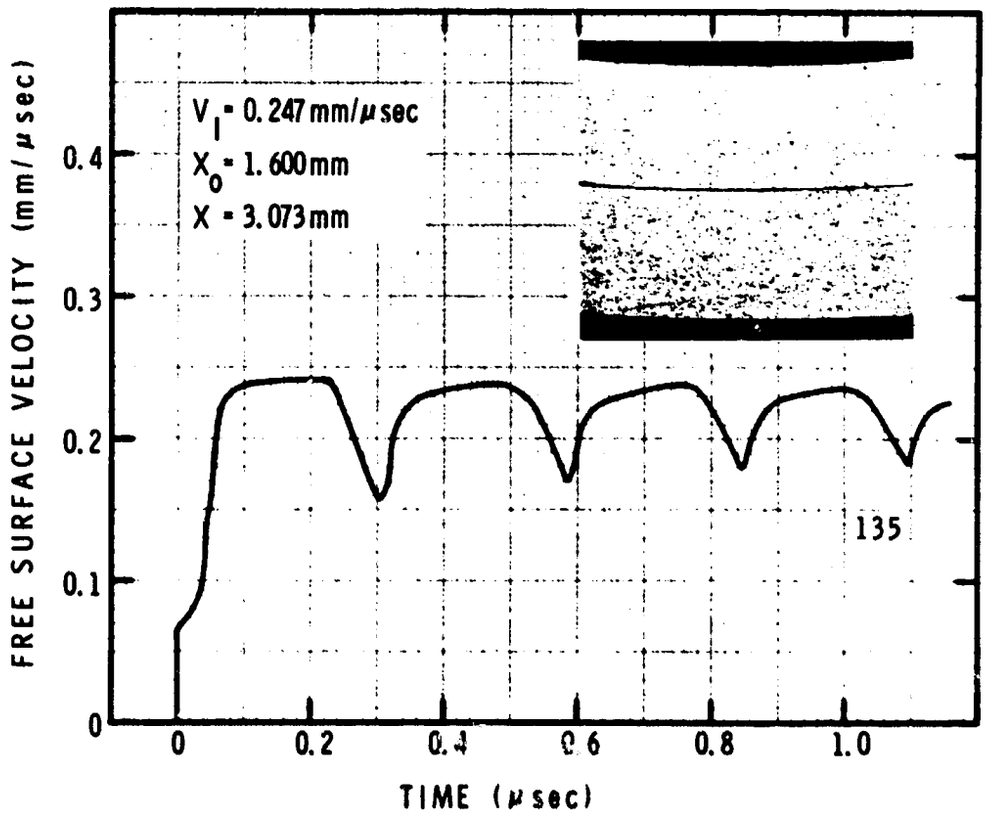

Figure 52 "Zero-Strength" Spall Profile, 6061-T6

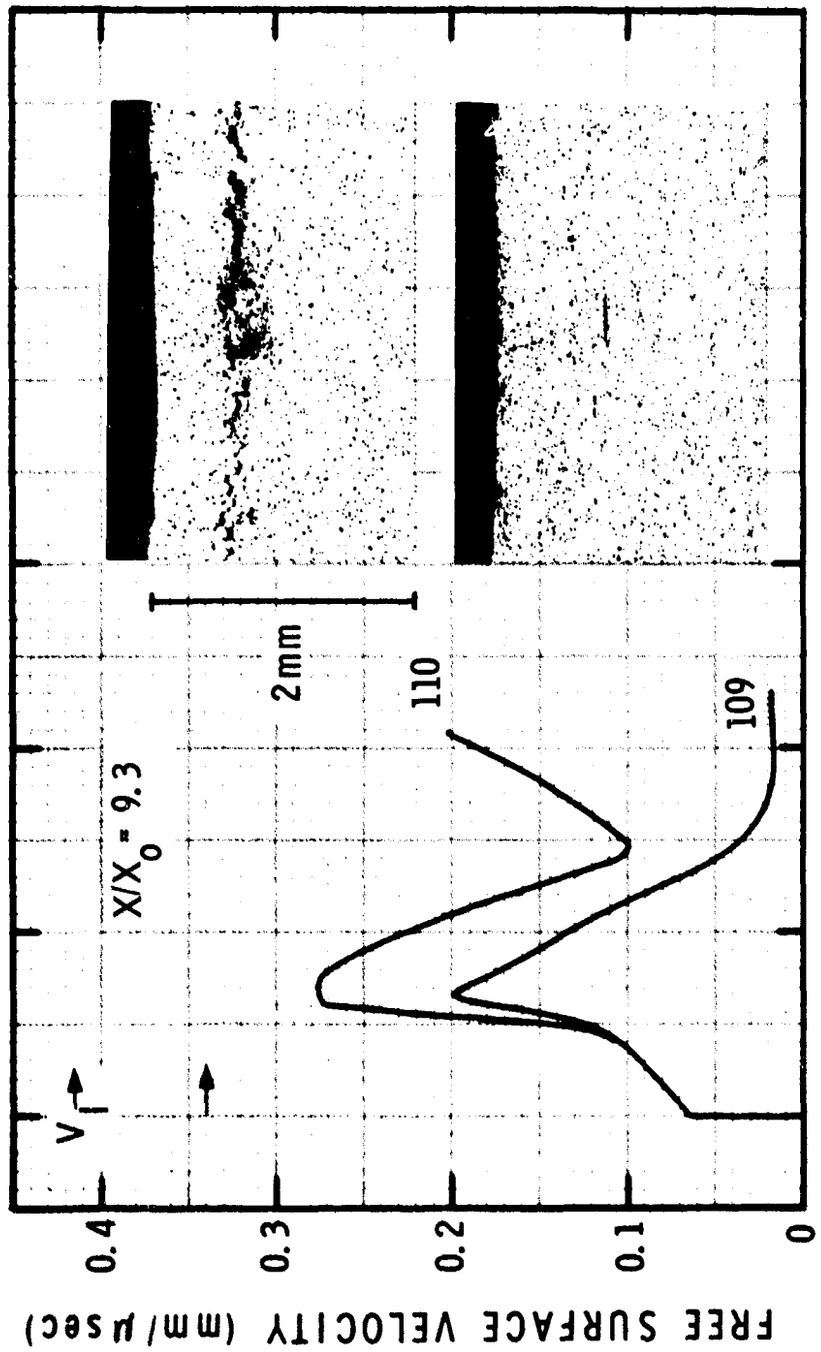

Figure 53 Attenuated Spall Profiles, 6061-T6

SUMMARY

The dynamic properties of 6061-T6 aluminum were measured under uniaxial stress and uniaxial strain conditions. The material tested was sheet and plate stock with average hardness of $57R_B$. Material response to compressive uniaxial stress deformation showed a well-defined yield with slight strain-hardening. Strain-rate sensitivity was essentially zero at 20°C (2.9 kbar yeild) but sensitivty increased and yield decreased at 150, 204 and 288°C, for a range in strain rate of 0.005/sec to 1000/sec.

Longitudinal and shear wave velocities were measured as functions of temperature and pressure, giving the following (in mm/μsec):

$$C_L = 6.387 - (0.00093T)$$

$$C_L = 3.214 - (0.00084T)$$

(T in °C)

$$C_L = 6.368 + (0.0180P) - (0.0001P^2)$$

$$C_S = 3.197 + (0.0108P) - (0.00005P^2)$$

(P in kbar)

Principal elastic constants were evaluated at T = 20°C and P = 0, including:

$$\text{Bulk Modulus} = K_0^S = 728 \text{ kbar}$$

$$\left(\frac{\partial K^S}{\partial P}\right)_S = 4.60, \quad \left(\frac{\partial K^S}{\partial P}\right)_T = 4.75$$

Shear Modulus = G_0^S = 276 kbar

$$\left(\frac{\partial G^S}{\partial P}\right)_S = 2.12, \quad \left(\frac{\partial G^S}{\partial P}\right)_T = 2.25$$

Poisson's Ratio = 0.331

Elastic wave velocity data were also used in determining the Gruneisen parameter γ and the Debye temperature θ:

$\gamma = 1.97$ @ T = 20°C and P = 0

$\frac{\partial \gamma}{\partial T} = + 0.000051/°C$ @ T = 20°C

$\frac{\partial \gamma}{\partial P} = - 0.0051/kbar$ @ P = 0

$\theta = 420°K$

The shock wave hugoniot was determined experimentally to be:

$$\sigma_H = 1.0 + 140.4\ u_p + 37.7\ u_p^2 \quad (\sigma_H < 200 \text{ kbar})$$

Assumption of an ideal elastic-plastic wave structure with a 5.7 kbar hugoniot elastic limit and equilibrium initial and final states gave:

$$\sigma_H = 2.3 + 708\ \mu + 1607\mu^2$$

$$P_H = 708\ \mu + 1607\mu^2$$

$$U_S = 5.24 + 1.40u_p$$

The hydrostat as determined from elastic constants data was:

$$P_H = 896 \left[(1+\mu)^{1.93} - 1 \right] - 1004 \ln (1+\mu) + 676 \left(\frac{\mu}{1+\mu} \right)^3$$

(Keane equation of state)

Measurements of compressive wave development showed the wave front to be characterized by a well-defined elastic portion and a transition to a spreading plastic wave. Elastic precursor decay was ∿ 75% to 6 kbar after 6 mm of travel. Peak pressure attenuation was ∿ 44% at X/X_0 = 12.6 for a 20 kbar, 0.5 μsec pulse, and ∿ 46% at X/X_0 = 20 for a 102 kbar, 0.08 μsec pulse.

Spall fracture behavior was determined for several elastic pulse widths ranging from 0.08 to 1.26 μsec. The incipient spall threshold, expressed as impact velocity, increased with decreasing pulse width, and decreased with increasing temperature for 20, 288 and 400°C. The spall plane was reasonably well-defined, and was located approximately one impactor thickness from the target rear surface, for unattenuated pulses. Failure was of a ductile nature with voids initiated at relatively brittle particles.

ACKNOWLEDGMENTS

The authors wish to thank Mr. N. H. Froula and Mr. A. R. McMillan for contributions to the equation of state and wave propagation studies, Mr. F. L. Schierloh for assistance in the strain rate work and Dr. H. Chin for development of the data analysis programs. Also the assistance of the following Materials and Structures Laboratory personnel in the experimental work is gratefully recognized: Mr. F. Stemczynski and Mr. E. Stretanski for EOS and wave profile tests; Mr. J. Havens for ultrasonics measurements; Mr. C. Woodcock for spall tests; Mr. J. Bonner and Mr. H. Simmons for strain rate tests; Mr. C. Whitchurch and Mr. L. Seltz for metallographic work; and Mr. W. Trippen and Mr. C. Strong for data analysis.

REFERENCES

1. "A Selected Bibliography on Dynamic Properties of Materials", compiled by Christman, D. R., General Motors Corporation, Manufacturing Development, DASA 2511, June 1970 (AD 710823).

2. Alcoa Aluminum Handbook, Aluminum Company of America, Pittsburgh, Pa., 1962.

3. Materials Data Handbook, Aluminum Alloy 6061, Technology Utilization Office, NASA, TSP-10065, 1969 (PB 183426).

4. Metals Handbook, 8th. Ed., Vol. 1: Properties and Selection of Metals, Lyman, T., Ed., American Society for Metals, Metals Park, Ohio, 1961.

5. Handbook of Chemistry and Physics, 45th. Ed., Weast, R. C., Ed., The Chemical Rubber Co., Cleveland, Ohio, 1964.

6. Thermophysical Properties of High Temperature Solid Materials, Vol. 1: Elements, Touloukian, Y. S., Ed., The McMillan Co., New York, N. Y., 1967.

7. Aerospace Structural Metals Handbook, Chapter Code 3206 (ALWT, 6061 Aluminum), Mechanical Properties Data Center, Belfour Stulen Inc., Traverse City, Michigan, 1966.

8. Babcock, S. G., Langan, J. J., Norvey, D. B., Michaels, T. E., Schierloh, F. L. and Green, S. J., "Characterization of Three Aluminum Alloys", General Motors Corporation, Manufacturing Development, AMRC-CR-71-3, January 1971 (AD724195).

9. Milligan, R. V., Koo, W. H. and Davidson, T. E., "The Bauschinger Effect in a High-Strength Steel", ASME Trans. - J. Basic Eng., Ser. D., Vol. 88, p. 480-488, 1966.

10. Milligan, R. V., Private Communication, Watervleit Arsenal, Watervleit, New York, 1970.

11. Buckley, S. N. and Entwistle, K. M., "The Bauschinger Effect in Super-Pure Aluminum Single Crystals and Polycrystals", Acta Met., Vol. 4, p. 352-361, 1956.

12. Babcock, S. G., Kumar, [illegible] and Green, S. J., "Response of Materials to Suddenly Applied Stress Loads, Part I: High Strain-Rate Properties of Eleven Reentry-Vehicle Materials at Elevated Temperatures", General Motors Corporation, Manufacturing Development, AFFDL-TR-67-35, Part I, April 1967 (AD 813880).

13. Maiden, C. J. and Green, S. J., "Compressive Strain-Rate Tests on Six Selected Materials at Strain Rates From 10^{-3} to 10^{4} In/In/Sec", ASME Trans. - J. Appl. Mech., Ser. E., Vol. 33, p. 496-504, 1966.

14. Holt, D. L., Babcock, S. G., Green, S. J. and Maiden, C. J., "The Strain-Rate Dependence of the Flow Stress in Some Aluminum Alloys", ASM Trans. Quart., Vol. 60, p. 152-159, 1967.

15. Green, S. J., Leasia, J. D., Perkins, R. D. and Maiden, C. J., "Development of Multiaxial Stress High Strain-Rate Techniques", General Motors Corporation, Manufacturing Development, SAMSO-TR-68-71, Vol. III, Jan. 1968 (AD 847163L).

16. Perkins, R. D., Jones, A. H., Green, S. J., Leasia, J. D. and Heimbuch, R. A., "Multiaxial Loading Behavior of Four Materials Including ATJ-S Graphite and RAD-6300 Carbon Phenolic", General Motors Corporation, Manufacturing Development, SAMSO-TR-69-393, Vol. I, Aug. 1970 (AD 874866L).

17. Babcock, S. G. and Hochstein, P. A., "High Strain-Rate Testing of Rapidly Heated Conductive Materials to 7000°F", Exp. Mech., Vol. 10, p. 78-83, 1970.

18. Babcock, S. G., Langan, J. J., Norvey, D. B. and Schierloh, F. L., "Subsequent Yield and High Heating Rate Properties of Two Aluminum Alloys", General Motors Corporation, Manufacturing Development, Materials and Structures Laboratory, MSL-70-24, Sept. 1970.

19. Green, S. J., et al., "Fundamental Material Behavior Study", General Motors Corporation, GM Defense Research Laboratories, BSD-TR-66-398, Oct. 1966 (AD 804889L).

20. Barker, L. M., Lundergan, C. D. and Herrmann, W., "Dynamic Response of Aluminum", J. Appl. Phys., Vol. 35, p. 1203-1212, 1964.

21. Asay, J. R., Urzendowski, S. R. and Guenther, A. J., "Ultrasonic and Thermal Studies of Selected Metals, Laminated Materials and Plastics", Air Force Weapons Laboratory, AFWL-TR-67-91, Jan. 1968 (AD 827596); also, Asay, J. R. and Guenther, A. H., "Ultrasonic Studies of 1060 and 6061-T6 Aluminum", J. Appl. Phys., Vol. 38, p. 4086-4088, 1967.

22. Seaman, L., Williams, R. F., Rosenberg, J. T., Erlich, D. C. and Linde, R. K., "Classification of Materials by Shock Properties", Stanford Research Institute, AFWL-TR-69-96, Nov. 1969 (AD 865505).

23. Johnson, J. N. and Barker, L. M., "Dislocation Dynamics and Steady Plastic Wave Profiles in 6061-T6 Aluminum", J. Appl. Phys., Vol. 40, p. 4321-4334, 1969.

24. Toupin, R. A. and Bernstein, B., "Sound Waves in Deformed Perfectly Elastic Materials, Acoustoelastic Effect", Ac. Soc. Am. J., Vol. 33, p. 216-225, 1961.

25. Gerlich, D. and Fisher, E. S., "The High Temperature Elastic Moduli of Aluminum", J. Phys. Chem. Solids, Vol. 30, p. 1197-1205, 1969.

26. Thomas, J. F., "Third-Order Elastic Constants of Aluminum", Phys. Rev., Vol. 175, p. 955-962, 1968.

27. Ho, P. S. and Ruoff, A. L., "Pressure Dependence of the Elastic Constants for Aluminum from 77° to 300°K", J. Appl. Phys., Vol. 40, p. 3151-3156, 1969.

28. Kolsky, H., Stress Waves in Solids, S1098, Dover Publications, Inc., New York, N. Y. 1963.

29. Mason, W. P., "Acoustic Properties of Solids", American Institute of Physics Handbook, 2nd. Ed., p. 3-28, 3-97, 1963.

30. Barsch, G. R. and Chang, Z. P., "Adiabatic, Isothermal, and Intermediate Pressure Derivatives of the Elastic Constants for Cubic Symmetry", Phy. Stat. Sol., Vol. 19, p. 129-151, 1967.

31. Anderson, O. L., "Elastic Constants Under Pressure", Lamont Geological Observatory, 1968 (PB 182479).

32. Walsh, J. M., Rice, M. H., McQueen, R. G. and Yarger, F. L., "Shock-Wave Compressions of Twenty-Seven Metals, Equation of State of Metals", Phys. Rev., Vol. 108, p. 196-216, 1957.

33. Gschneidner, K. A., "Physical Properties and Interrelationships of Metallic and Semimetallic Elements", Solid State Physics, Vol. 16, p. 275-426, 1964.

34. Huang, Y. K., "Direct Method of Calculating the Gruneisen Parameter γ Based on Shock-Wave Measurements of Metals", J. Chem. Phys., Vol. 51, p. 2573-2577, 1969.

35. Slater, J. C., Introduction to Chemical Physics, McGraw-Hill Book Co., New York, N. Y., 1939.

36. Dugdale, J. S. and MacDonald, D. K. C., "The Thermal Expansion of Solids", Phys. Rev., Vol. 89, p. 832-834, 1953.

37. Schreiber, E. and Anderson, O. L., "Pressure Derivatives of the Sound Velocities of Polycrystalline Alumina", Am. Ceram. Soc. J., Vol. 49, p. 184-190, 1966.

38. Anderson, O. L. and Dienes, G. J., Non-Crystalline Solids (Chapter 18), Ed. by Frechette, V. D., John Wiley and Sons, New York, 1960.

39. Schuele, D. E. and Smith, C. S., "Low Temperature Thermal Expansion of RbI", J. Phys. Chem. Solids, Vol. 25, p. 801-814, 1964.

40. Herbstein, F. H., "Methods of Measuring Debye Temperature and Comparisons of Results for Some Cubic Crystals", Adv. Phys., Vol. 10, p 313-355, 1961.

41. Anderson, O. L., "A Simplified Method for Calculating the Debye Temperature from Elastic Constants", J. Phys. Chem. Solids, Vol. 24, p. 909-917, 1963.

42. Alers, G. A., "Use of Sound Velocity Measurements in Determining the Debye Temperature of Solids", Physical Acoustics, Vol. III, Part B (Lattice Dynamics), Academic Press, New York, N. Y., p. 1-42, 1965.

43. Sutton, P. M., "The Variation of the Elastic Constants of Crystalline Aluminum with Temperature between 63°K and 773°K", Phys. Rev., Vol. 91, p. 816-821, 1953 and Phys. Rev., Vol. 112, p. 2139, 1958.

44. Rice, M. H., McQueen, R. G. and Walsh, J. M., "Compression of Solids by Strong Shock Waves", Solid State Physics, Vol. 6, p. 1-63, 1958.

45. Al'tshuler, L. V., "Use of Shock Waves in High-Pressure Physics", Sov. Phys. Uspekhi, Vol. 8, p. 52-91, 1965.

46. Goodwin, L. K., Johnson, L. A. and Wright, R. S., "An Equation of State for Metals", Philco-Ford Corporation, Aeronutronic Division, DASA-2286, April 1969 (AD 858302).

47. Munson, D. E. and Barker, L. M., "Dynamically Determined Pressure-Volume, Relationships for Aluminum, Copper and Lead", J. Appl. Phys., Vol. 37, p. 1652-1660, 1966.

48. McQueen, R. G., Marsh, S. P., Taylor, J. W., Fritz, J. N. and Carter, W. J., "The Equation of State of Solids from Shock Wave Studies", High-Velocity Impact Phenomena, p. 293-417, Academic Press, New York, N. Y., 1970.

49. Jones, A. H., Maiden, C. J. and Isbell, W. M., "The Effect of High-Pressure Shock Waves on Metals: Mechanical and Metallurgical Behavior", Mechanical Behavior of Materials Under Pressure, Pugh, H. Ll. D., Ed., p. 680-747, Elsevier Publishing Co., New York, 1970.

50. Chin, H. C., "A Computer Program to Analyze X-Cut Quartz Data Obtained from Shock Loading", General Motors Corporation, Manufacturing Development, Materials and Structures Laboratory, MSL-70-15, June, 1970.

51. Lundergan, C. D. and Herrmann, W., "Equation of State of 6061-T6 Aluminum at Low Pressures", J. Appl. Phys., Vol. 34, p. 2046-2052, 1963.

52. Froula, N. E., Unpublished Data, General Motors Corporation, Manufacturing Development, 1969.

53. Overton, W. C., "Relation Between Ultrasonically Measured Properties and the Coefficients in the Solid Equation of State", J. Chem. Phys., Vol. 37, p. 116-119, 1962.

54. Swenson, C. A., "Equation of State of Cubic Solids; Some Generalizations", J. Phys. Chem. Solids, Vol. 29, p. 1337-1348, 1968.

55. Anderson, O. L., "The Use of Ultrasonic Measurements Under Modest Pressures to Estimate Compression at High Pressures", J. Phys. Chem. Solids, Vol. 27, p. 547-565, 1966.

56. Lamberson, D. L., "The High Pressure Equation of State of Tantalum, Polystyrene and Carbon Phenolic Determined from Ultrasonic Velocities", Doctoral Dissertation, Air Force Institute of Technology (AFIT-SE), Wright-Patterson AFB, Ohio, March, 1969.

57. MacDonald, J. R., "Review of Some Experimental and Analytical Equations of State", Rev. Mod. Phys., Vol. 41, p. 316-349, 1969.

58. Birch, F., "The Effect of Pressure Upon the Elastic Parameters of Isotropic Solids, According to Murnaghan's Theory of Finite Strain", J. Appl. Phys., Vol. 9, p. 279-288, 1938.

59. Birch, F., "Elasticity and Constitution of the Earth's Interior", J. Geophys. Res., Vol. 57, p. 227-286, 1952.

60. Murnaghan, F. D., "The Compressibility of Media Under Extreme Pressures", Proc. Nat. Ac. Sci., Vol. 30, p. 244-247, 1944.

61. Keane, A., "An Investigation of Finite Strain in an Isotropic Material Subjected to Hydrostatic Pressure and Its Seismological Applications", Australian J. Phys., Vol. 7, p. 323-333, 1954.

62. Anderson, O. L., "On the Use of Ultrasonic and Shock-Wave Data to Estimate Compressions at Extremely High Pressures", Phys. Earth Planet. Interiors, Vol. 1, p. 169-176, 1968.

63. Duvall, G. E. and Zwolinski, B. J., "Entropic Equations of State and Their Applications to Shock Wave Phenomena in Solids", Acoust. Soc. Am. J., Vol. 27, p. 1054-1058, 1955.

64. Zel'dovich, Y. B. and Raizer, Y. P., Physics of Shock Waves and High-Temperature Hydrodynamic Phenomena, Vol. II, Academic Press, New York, N. Y., p. 688-709, 1967.

65. Ruoff, A. L., "Linear Shock-Velocity-Particle-Velocity Relationship", J. Appl. Phys., Vol. 38, p. 4976-4980, 1967.

66. Vaidya, S. N. and Kennedy, G. C., "Compressibility of 18 Metals to 45 kbar", J. Phys. Chem. Solids, Vol. 31, p. 2329-2345, 1970.

67. Herrmann, W., "Nonlinear Stress Waves in Metals", Wave Propagation in Solids, Miklowitz, J., Ed., p. 129-183, American Society of Mechanical Engineers, 1969.

68. Chang, H. L. and Horie, Y., "An Analysis of Plane Shock-Structures in 6061-T6 Aluminum", North Carolina State University, TR-71-1, Feb. 1971 (AD 720716).

69. Johnson, J. N., "Constitutive Relation for Rate-Dependent Plastic Flow in Polycrystalline Metals", J. Appl. Phys., Vol. 40, p. 2287-2293, 1969.

70. Read, H. E., Triplett, J. R. and Cecil, R. A., "Dislocation Dynamics and the Formulation of Constitutive Equations for Rate Dependent Plastic Flow in Metals", Systems, Science, and Software, DASA 2638, Dec. 1970 (AD 722314).

71. Taylor, J. W., "Dislocation Dynamics and Dynamic Yielding", J. Appl. Phys., Vol. 36, p. 3146-3150, 1965.

72. Gilman, J. J., "Dislocation Dynamics and the Response of Materials to Impact", Appl. Mech. Rev., Vol. 21, p. 767-783, 1968.

73. McMillan, A. R., Isbell, W. M. and Jones, A. H., "High Pressure Shock Wave Attenuation", General Motors Corporation, Manufacturing Development, DASA 2425, June 1971.

74. Butcher, B. M., Barker, L. M., Munson, D. E. and Lundergan, C. D., "Influence of Stress History on Time-Dependent Spall in Metals", AIAA J., Vol. 2, p. 977-990, 1964.

75. Oscarson, J. H. and Graff, K. F., "Spall Fracture and Dynamic Response of Materials", Battelle Memorial Institute, BAT-197A-4-3, 21 March 1968 (AD 669440).

76. Charest, J. A., Horne, D. E. and Jenrette, B. D., "Phenomenological Considerations for Spall Measurements", E,G&G, Santa Barbara Division, S-56-TP, Jan. 1970.

77. Kreer, J. R., "Dynamic Fracture in 6061-T6 Aluminum", Air Force Weapons Laboratory, AFWL-TR-70-180, Jan. 1971 (AD 881534L).

78. Keller, D. V. and Tuler, F. R., "Predix Metals Report", (Preliminary Draft), Effects Technology, Inc., CR-70-06, 1970.

79. Jajosky, C. and Ferdman, M. A., "Spall Studies on 6061-T6 Aluminum, Air Force Weapons Laboratory, AFWL-TR-69-101, Sept. 1969 (AD 860078).

80. Cohen, L. J. and Berkowitz, H. M., "Time-Dependent Fracture Criteria for 6061-T6 Aluminum Under Stress-Wave Loading in Uniaxial Strain", McDonnell Douglas Astronautics Company, Western Division, Douglas Paper 10191, Nov. 1969.

81. Stefansky, T. and Shea, J. H., "Dynamic Fracture Experiments Using High-Energy Pulsed Electron Beams", Physics International Co., DASA 2699, July 1971 (AD727983).

82. Christman, D. R., Michaels, T. E., Isbell, W. M. and Babcock, S. G., "Measurements of Dynamic Properties of Materials, Vol. IV: Alpha Titanium", General Motors Corporation, Manufacturing Development, DASA 2501-4, 1971.

83. Isbell, W. M., Christman, D. R. and Babcock, S. G., "Measurements of Dynamic Properties of Materials, Vol. VI: Tantalum", General Motors Corporation, Manufacturing Development, DASA 2501-6, 1971.

84. Christman, D. R., Isbell, W. M. and Babcock, S. G., "Measurements of Dynamic Properties of Materials, Vol. V: OFHC Copper", General Motors Corporation, Manufacturing Development, DASA 2501-5, 1971.

85. Au, R. H. C., "Nucleating Mechanisms for Spall in Aluminum", AIAA J., Vol. 8, p. 1171-1173, 1970.

86. Tuler, F. R., "Fracture Surface Observations in 6061-T6 Aluminum at Different Strain Rates", Sandia Laboratories, SC-DR-68-497, Oct. 1968.

87. Stevens, A. L. and Tuler, F. R., "The Effect of Precompression on the Dynamic Fracture Strength of 1020 Steel and 6061-T6 Aluminum", Sandia Laboratories, to be published.

88. Charest, J. A., "Spall Compendium", E,G&G, Santa Barbara Division, 1971.

89. Butcher, B. M., "Spallation in 6061-T6 Aluminum", Behavior of Dense Media Under High Dynamic Pressures, Gordon and Breach, New York, N. Y., p. 245-250, 1968.

90. Taylor, J. W., "Stress Wave Profiles in Several Metals", Dislocation Dynamics, p. 573-589, McGraw-Hill Book Co., New York, N. Y., 1968.

91. Brammer, J. A., "Temperature Influence on the Shock Response of 2024 Aluminum", Sandia Laboratories, SC-RR-70-124, March 1970.

92. Isbell, W. M. and Christman, D. R., "Shock Propagation and Fracture in 6061-T6 Aluminum from Wave Profile Measurements", General Motors Corporation, Manufacturing Development, DASA 2419, April 1970 (AD 705536).

93. Al'tshuler, L. V., Novikov, S. A. and Divnov, I. I., "The Relationship Between the Critical Breaking Stress and the Time of Failure as a Result of the Explosive Stressing of Metals", Sov. Phys.-Doklady, Vol. 11, p. 79-82, 1966.

94. Thurston, R. S. and Mudd, W. L., "Spallation Criteria for Numerical Calculation", Los Alamos Scientific Laboratory, LA-4013, Sept., 1968.

95. Tuler, F. R. and Butcher, B. M., "A Criterion for the Time Dependence of Dynamic Fracture", Int. J. Fract. Mech., Vol. 4, p. 431-437, 1968.

96. Field, F. A., "A Simple Crack Extension Criterion for Time Dependent Spallation", Aerospace Corporation, SAMSO-TR-69-405, 20 Oct., 1969 (AD 863205).

97. Barbee, T., Seaman, L. and Crewdson, R. C., "Dynamic Fracture Criteria of Homogeneous Materials", Stanford Research Institute, AFWL-TR-70-99, Nov., 1970.

98. Butcher, B. M. and Young, E. G., "A Critical Evaluation of 6061-T6 Spall Data", Sandia Laboratories, SC-DR-710173, May, 1971.

(Page 108 is Blank)

APPENDIX A

ELASTIC CONSTANTS EQUATIONS

Following are the equations used in calculating various elastic constants and the adiabatic and isothermal pressure and temperature derivatives of the bulk and shear modulii (K and G)*:

$$C_B = \sqrt{C_L^2 - 4/3\ C_S^2}$$

(Bulk Wave Velocity)

$$C_E = \sqrt{2(1+\nu)\ C_S^2}$$

(Sound wave velocity, longitudinal wave of infinite wave length in bar, lateral displacement allowed)

$$C_R: \quad k_1^6 - 8k_1^4 + (24-16\alpha_1^2)k_1^2 + (16\alpha_1^2-16) = 0$$

where $k_1^2 = (C_R/C_S)^2$, $\alpha_1^2 = (C_S/C_L)^2$

(Rayleigh or Surface Wave Velocity)

---

* The expressions for the pressure derivatives are simplified in these equations, e.g.,

$$K_{0S}^{S'} = \left(\frac{\partial K^S}{\partial P}\right)_S \Bigg|_{P=0}.$$

$$\nu = [0.5-(C_S/C_L)^2]/[1.0-(C_S/C_L)^2]$$

(Poisson's Ratio)

$$K = \rho C_B^2 = \rho(C_L^2-4/3C_S^2)$$

(Bulk Modulus)

$$G = \rho C_S^2$$

(Shear or Rigidity Modulus)

$$E = 2\rho(1+\nu)\ C_S^2$$

(Young's or Elastic Modulus)

$$\lambda = 2\rho\nu C_S^2/(1-2\nu)$$

(Lamé's Parameter)

$$K_0^T = \frac{K_0^S}{1 + \beta\gamma_0 T}$$

where $\gamma_0 = \dfrac{\beta K_0^S}{\rho_0 c_p}$

$$K_{0S}^{S'} = K_{0T}^{S'} + \left(\frac{\partial K^S}{\partial T}\right)_0 \left(\frac{\gamma_0 T}{K_0^S}\right)$$

$$K_{0T}^{T'} = K_{0T}^{S'} + \beta\gamma_0 T \left(\frac{K_0^T}{K_0^S} \right) \left[1 - \frac{2}{\beta K_0^T} \left(\frac{\partial K^T}{\partial T} \right)_0 - 2K_{0T}^{S'} \right]$$

$$+ \left[\beta\gamma_0 T \left(\frac{K_0^T}{K_0^S} \right) \right]^2 \left[K_{0T}^{S'} - 1 - \frac{1}{\beta^2} \left(\frac{\partial \beta}{\partial T} \right)_0 \right]$$

$$K_{0S}^{T'} = K_{0T}^{T'} + \left(\frac{\partial K^T}{\partial T} \right)_0 \left(\frac{\gamma_0 T}{K_0^S} \right)$$

$$\left(\frac{\partial K^S}{\partial T} \right)_S = \left(\frac{\partial K^S}{\partial T} \right)_0 + K_{0T}^{S'} \left(\frac{K_0^S}{\gamma_0 T} \right)$$

$$\left(\frac{\partial K^T}{\partial T} \right)_0 = \frac{\left(\frac{\partial K^S}{\partial T} \right)_0 - \beta\gamma_0 K_0^T - \beta T K_0^T \left(\frac{\partial \gamma}{\partial T} \right)_0 - \gamma_0 T K_0^T \left(\frac{\partial \beta}{\partial T} \right)_0}{(1+\beta\gamma_0 T)}$$

$$\left(\frac{\partial K^T}{\partial T} \right)_S = \left(\frac{\partial K^T}{\partial T} \right)_0 + K_{0T}^{T'} \left(\frac{K_0^S}{\gamma_0 T} \right)$$

$$G_0^T = G_0^S = G_0$$

$$G_{0T}^{T'} = G_{0T}^{S'} = G_{0T}'$$

$$G'_{0S} = G'_{0T} + \left(\frac{\partial G}{\partial T}\right)_0 \left(\frac{\gamma_0 T}{K_0^S}\right)$$

$$\left(\frac{\partial G}{\partial T}\right)_S = \left(\frac{\partial G}{\partial T}\right)_0 + G'_{0T} \left(\frac{K_0^S}{\gamma_0 T}\right)$$

APPENDIX B

GRUNEISEN PARAMETER ESTIMATES

1. The Gruneisen parameter is defined thermodynamically as

$$\gamma = \frac{1}{\rho c_p} \left(\frac{\partial V}{\partial T}\right)_P \left(\frac{\partial P}{\partial V}\right)_S = \frac{\beta K^S}{\rho c_p}$$

For an isotropic elastic solid, this becomes

$$\gamma = \frac{\beta}{c_p} \left(C_L^2 - \frac{4}{3} C_S^2\right)$$

Substituting appropriate values for aluminum gives

$$\gamma_0 = 1.97$$

2. Slater developed a relation that was an extension of the Debye Theory for a three-dimensional continuum, and assumed Poisson's ratio was independent of volume and γ is the same for all vibrational frequencies:

$$\gamma = -\frac{V}{2} \left(\frac{\partial^2 P/\partial V^2}{\partial P/\partial V}\right) - \frac{2}{3}$$

which simplifies at zero pressure to

$$\gamma_0 = \frac{1}{2} \left(K_{0S}^{S'} - \frac{1}{3}\right) = 2S - \frac{2}{3}$$

where S is from $U_S = C_B + Su_p$.

Ultrasonic data gives S = 1.40 and γ = 2.13.

Shock wave data gives S = 1.4[illegible] and γ = 2.13.

3. Dugdale and MacDonald give an expression for plane wave velocity vs. volume in a three-dimensional continuum that leads to an expression for γ differing from Slater's by a constant (1/3):

$$\gamma = -\frac{V}{2}\left(\frac{\partial^2 P/\partial V^2}{\partial P/\partial V}\right) - 1$$

which simplifies at zero pressure to

$$\gamma_0 = \frac{1}{2}\left(K_{0S}^{S'} - 1\right) = 2S - 1$$

Both ultrasonic and shock wave data give γ = 1.80.

4. Anderson and Dienes give expressions for γ in terms of the longitudinal and shear modes of wave propagation:

$$\gamma_L = \frac{1}{3} + \frac{K_0^T}{C_L}\left(\frac{dC_L}{dP}\right)_0$$

$$\gamma_S = \frac{1}{3} + \frac{K_0^T}{C_S}\left(\frac{dC_S}{dP}\right)_0$$

Ultrasonic data gives γ_L = 2.31 and γ_S = 2.70.

5. Schuele and Smith give expressions for the "low-temperature" and "high-temperature" Gruneisen ratio, where low-temperature is the range in which it is assumed the solid behaves as a continuum and high-temperature is the range where all vibrational modes are excited and γ is constant:

$$\gamma_{LT} = \frac{1}{2+\varepsilon^3} \left(\varepsilon^3 \gamma_L + 2\gamma_S \right)$$

$$(\varepsilon = C_S/C_L)$$

$$\gamma_{HT} = \frac{1}{3} \left(\gamma_L = 2\gamma_S \right)$$

Using ultrasonic data and γ_L and γ_S from above gives $\gamma_{LT} = 2.68$ and $\gamma_{HT} = 2.57$.

6. Perry calculated the Grueisen parameter from laser interferometer data obtained for electron beam energy deposition.* For polycrystalline aluminum, he obtained $\gamma = 2.02$ assuming instantaneous deposition and $\gamma = 2.11$ assuming 50 nsec deposition time.

(All of the ultrasonics data used in this appendix are for zero pressure and 20°C).

* Perry, F. C. "Thermoelastic Response of Polycrystalline Metals to Relativistic Electron Beam Absorption", J. Appl. Phys., Vol. 41, p. 5017-5022, 1970.

APPENDIX C

GRUNEISEN PARAMETER, PRESSURE DERIVATIVE

1. Thermodynamic Relation -

$$\gamma = \frac{\beta K}{\rho c_p}$$

$$\left(\frac{\partial \gamma}{\partial P}\right)_T = \gamma_0 \left[\frac{1}{\beta}\left(\frac{\partial \beta}{\partial P}\right)_T + \frac{1}{K^S}\left(\frac{\partial K^S}{\partial P}\right)_T - \frac{1}{\rho}\left(\frac{\partial \rho}{\partial P}\right)_T - \frac{1}{c_p}\left(\frac{\partial c_p}{\partial P}\right)_T\right] .$$

This can be simplified by using:*

$$\left(\frac{\partial \beta}{\partial P}\right)_T = \left(\frac{1}{K^T}\right)^2 \left(\frac{\partial K^T}{\partial T}\right)_P$$

$$\left(\frac{\partial \rho}{\partial P}\right)_T = \frac{\rho}{K^T}$$

$$\left(\frac{\partial c_p}{\partial P}\right)_T = -\frac{T}{\rho}\left[\left(\frac{\partial \beta}{\partial T}\right)_P + \beta^2\right]$$

* See, e.g. Thurston, R. N., "Ultrasonic Data and the Thermodynamics of Solids", IEEE Proc., Vol. 53, p. 1320-1336, 1965.

to give:

$$\left(\frac{\partial\gamma}{\partial P}\right)_T = \gamma_0 \left[\frac{1}{\beta K^T{}^2} \left(\frac{\partial K^T}{\partial T}\right)_P + \frac{1}{K^S} \left(\frac{\partial K^S}{\partial P}\right)_T - \frac{1}{K^T} + \frac{T}{c_p \rho} \left\{ \left(\frac{\partial \beta}{\partial T}\right)_P + \beta^2 \right\} \times 23.9 \right]$$

This can be modified to:

$$\left(\frac{\partial\gamma}{\partial P}\right)_T = \frac{\gamma_0}{K^S} \left[\left(\frac{\partial K^S}{\partial P}\right)_T + \frac{1}{\beta K^T} \left(\frac{\partial K^S}{\partial T}\right)_P - 1 - \gamma - T \left(\frac{\partial \gamma}{\partial T}\right)_P \right]$$

2. Constant γ/V:

$$\frac{\gamma}{V} = \frac{\gamma_0}{V_0} \quad \text{or} \quad \gamma = \rho_0 \gamma_0 V$$

$$\left(\frac{\partial\gamma}{\partial P}\right)_T = \rho_0 \gamma_0 \left(\frac{\partial V}{\partial P}\right)_T$$

but $$\left(\frac{\partial V}{\partial P}\right)_T = -\frac{1}{\rho^2} \left(\frac{\partial \rho}{\partial P}\right)_T = -\frac{1}{\rho K^T}$$

so $$\left(\frac{\partial\gamma}{\partial P}\right)_T = -\frac{\rho_0 \gamma_0}{\rho K^T}$$

Letting $\rho = \rho_0 \left(\frac{K_0^T + K_{0T}^{T'} P}{K_0^T} \right)^{1/K_{0T}^{T'}}$

and $K^T = K_0^T + K_{0T}^{T'} P$

gives:

$$\left(\frac{\partial \gamma}{\partial P} \right)_T = \frac{-\gamma_0}{\left(\frac{1}{K_0^T} \right)^{\left(1/K_{0T}^{T'} \right)} \left(K_0^T + K_{0T}^{T'} P \right)^{\left(1+K_{0T}^{T'} \right)/K_{0T}^{T'}}}$$

At P = 0, this reduces to

$$\left(\frac{\partial \gamma}{\partial P} \right)_T = - \frac{\gamma_0}{K_0^T}$$

APPENDIX D

DEVIATORIC STRESS ESTIMATES

The shock wave equation of state for aluminum is given by:

$$\left.\begin{aligned} \sigma_H &= 1.0 + 140.4\, u_p + 37.7\, u_p^2 \\ \sigma_H &= 2.3 + 708\mu + 1607\mu^2 \\ P_H &= 708\mu + 1607\mu^2 \quad \text{(Hydrostat)} \end{aligned}\right\} \qquad \text{(D-1)}$$

where $\mu = (v_o/v) - 1.$

The deviatoric stress (σ_D) can be defined as the difference between the dynamic stress-compression path ($\sigma_H - \mu$) and the hydrostat, and is a measure of the material's ability to support shear. If the material strain hardens, the deviatoric stress will be a function of μ. In Equation D-1, σ_D was assumed constant at 2.3 kbar which gives $P_H = \sigma_H - 2.3$.

The deviatoric stress can also be estimated from uniaxial stress data, shock wave data or ultrasonics data as follows:

$$\sigma_D = \sigma_H - P_H = \frac{2}{3} Y \qquad \text{(D-2)}$$

where Y is flow stress under uniaxial stress conditions.

A. The flow stress at low strain rate from the uniaxial stress tests (see Figure 3) is ~ 3.4 kbar, which gives σ_D = 2.3 kbar.

B. For a hugoniot elastic limit (σ_e) of 5.7 kbar, the relation $Y = \sigma_e (1-2\nu/1-\nu)$ gives Y = 2.9 kbar. From Equation D-2, σ_D = 1.9 kbar.

C. Since σ_D can also be taken as the difference between σ_H and P_H at a compression corresponding to the hugoniot elastic limit, one has

$$\sigma_D = \sigma_H - P_H = \sigma_e - P_e$$

where

$$\sigma_e = \rho_0 C_L^2 \left(\frac{\mu_e}{1+\mu_e}\right) = 1096 \left(\frac{\mu_e}{1+\mu_e}\right)$$

$$P_e = \rho_0 C_B^2 \left(\frac{\mu_e}{1+\mu_e}\right) = 728 \left(\frac{\mu_e}{1+\mu_e}\right)$$

For σ_e = 5.7 kbar: μ_e = 0.0052 and P_e = 3.8 kbar. This gives σ_D = 1.9 kbar.

The agreement of these estimates with the value of 2.3 kbar from Equation D-1 is considered good, taking into account the assumptions underlying each method and the experimental inaccuracies.

Also, it should be noted that the stress-axis intercept is larger in the σ_H - u plane than the σ_H - u_p plane. Assuming linear elastic and hydrostatic behavior up to the elastic limit, then:

σ_H - u_p plane -

$$\sigma_{D_u} = \rho_0 u_e (C_L - C_B)$$

σ_H - μ plane -

$$\sigma_{D_\mu} = \frac{\mu_e}{1+\mu_e} \left(\rho_0 C_L^2 - \rho_0 C_B^2 \right)$$

Using the approximations $u_e \simeq \mu_e / C_L$ and $\mu_e \simeq \mu_e/(1+\mu_e)$, and subtracting:

$$\Delta\sigma_D = \sigma_{D_u} - \sigma_{D_\mu} = \rho_0 C_B \mu_e (C_L - C_B)$$

For σ_e = 5.7 kbar, μ_e = 0.0052 and $\Delta\sigma_D$ = 0.9 kbar, compared to $\Delta\sigma_D$ = 1.3 kbar from σ_H - u_p and σ_H - μ given in Equation D-1.

APPENDIX E

EQUATION OF STATE, ULTRASONICS

Numerous analytical and empirical relations have been developed for determining equations of state from ultrasonics data. Some of these are presented here.

1. The Birch equation of state for the isotherm can be expressed as:*

$$P_T = \frac{3}{2} K_0^T \left[(1+\mu)^{7/3} - (1+\mu)^{5/3} \right] \left[1-\xi \left\{ (1+\mu)^{2/3} - 1 \right\} \right]$$

where $\xi = \frac{12-3\,K_{0T}^{T'}}{4}$

$$P_T = 1050 \left[(1+\mu)^{7/3} - (1+\mu)^{5/3} \right] \left[1+0.653 \left\{ (1+\mu)^{2/3} - 1 \right\} \right]$$

---

* Another parameter sometimes used with this equation of state is

$$+ \left[(1+\mu)^{2/3} - 1 \right]^2$$

where $= \frac{3}{8} \left[K_0^T K_{0t}^{T''} - 7K_{0T}^{T'} + \left(K_{0T}^{T'} \right)^2 + \frac{143}{9} \right]$

However, this term can usually be neglected, contributing ~0.6% at 100 kbar for aluminum.

2. The Murnaghan equation of state is derived by assuming the bulk modulus is linear with pressure which gives:

$$\text{Isotherm} - P_T = \frac{K_0^T}{K_{0T}^{T'}} \left[(1+\mu)^{K_{0T}^{T'}} - 1 \right]$$

$$P_T = 143.7 \left[(1+\mu)^{4.87} - 1 \right]$$

$$\text{Adiabat} - P_S = \frac{K_0^S}{K_{0S}^{S'}} \left[(1+\mu)^{K_{0S}^{S'}} - 1 \right]$$

$$P_S = 158.3 \left[(1+\mu)^{4.60} - 1 \right]$$

3. Instead of a linear bulk modulus-pressure relation, Keane assumed:

$$dK^S = \left[\frac{\left(K_0^{S'} - K_\infty^{S'} \right) K_0^S}{K^S} + K_\infty^{S'} \right] dP$$

where $K_\infty^{S'}$ is the limiting value of $K^{S'}$ at very high pressure.

This leads to:

$$P_S = \frac{K_0^S K_{0S}^{S'}}{\left(K_\infty^{S'} \right)^2} \left[(1+\mu)^{K_\infty^{S'}} - 1 \right] - \frac{\left(K_{0S}^{S'} - K_\infty^{S'} \right) K_0^S}{K_\infty^{S'}} \ln (1+\mu)$$

Huang* gives the upper bound for $K^{S'}$ as:

$$K_{\infty}^{S'} = 4S - \frac{11}{3} = K_{0S}^{S'} - \frac{8}{3} = 1.93$$

This gives:

$$P_S = 896 \left[(1+\mu)^{1.93} - 1 \right] - 1004 \ln (1+\mu)$$

* Huang, Y. K., "Analytical Approach to the Shock Compressibility of the 18 Cubic-Lattice Metals", J. Chem. Phys., Vol. 53, p. 571-575, 1970.

APPENDIX F

WAVE PROFILES

(Quartz Gage and Velocity Interferometer)

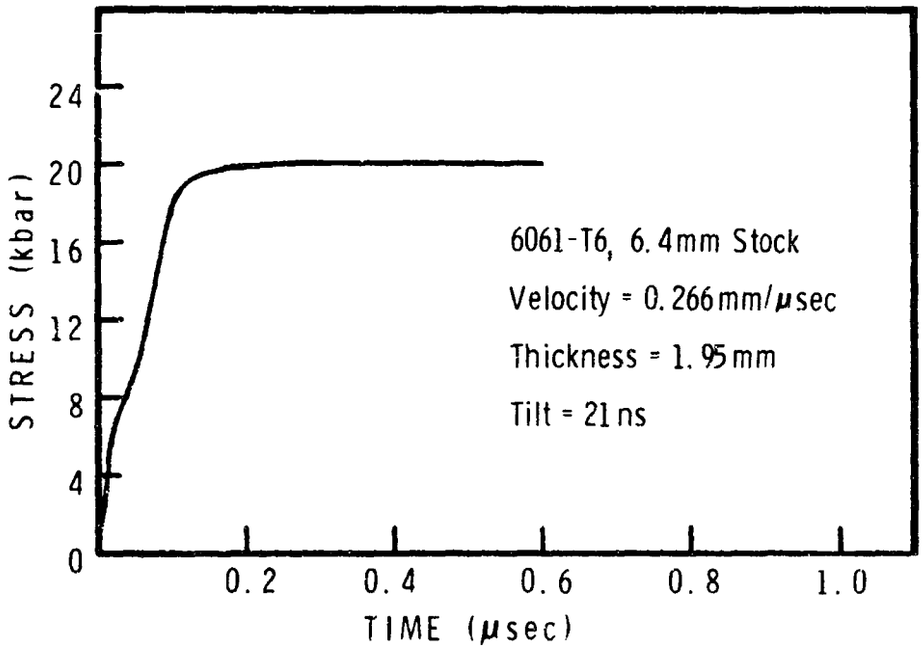
STRESS (kbar)
24
20
16
12
8
4
0
0.2
0.4
0.6
0.8
1.0
TIME (μsec)
6061-T6, 6.4mm Stock
Velocity = 0.266mm/μsec
Thickness = 1.95mm
Tilt = 21ns

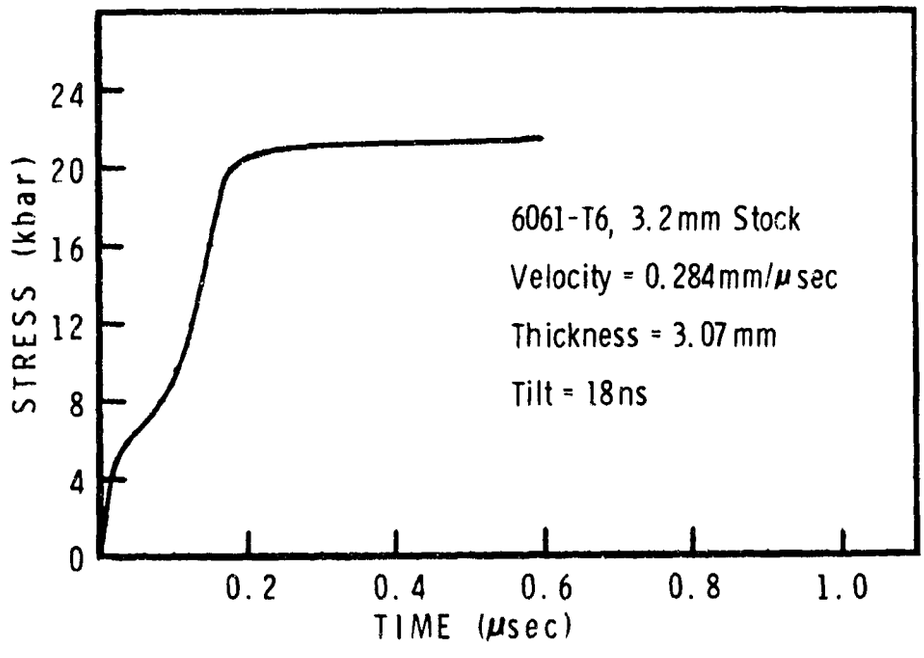
STRESS (kbar)
24
20
16
12
8
4
0
0.2
0.4
0.6
0.8
1.0
TIME (μsec)
6061-T6, 3.2mm Stock
Velocity = 0.284mm/μsec
Thickness = 3.07mm
Tilt = 18ns

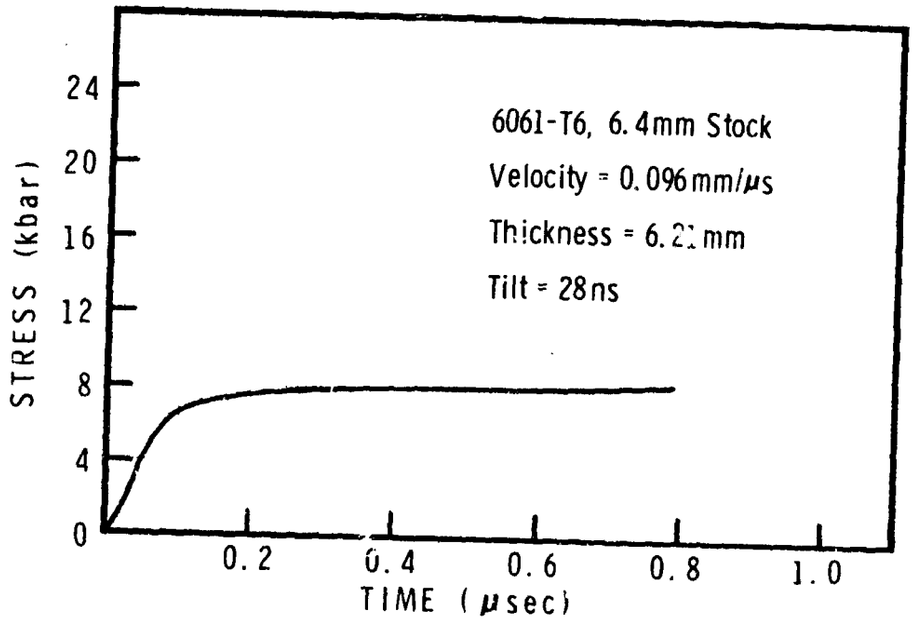
6061-T6, 6.4mm Stock
Velocity = 0.096 mm/μs
Thickness = 6.2[illegible] mm
Tilt = 28 ns
STRESS (kbar)
0
4
8
12
16
20
24
0.2
0.4
0.6
0.8
1.0
TIME (μsec)

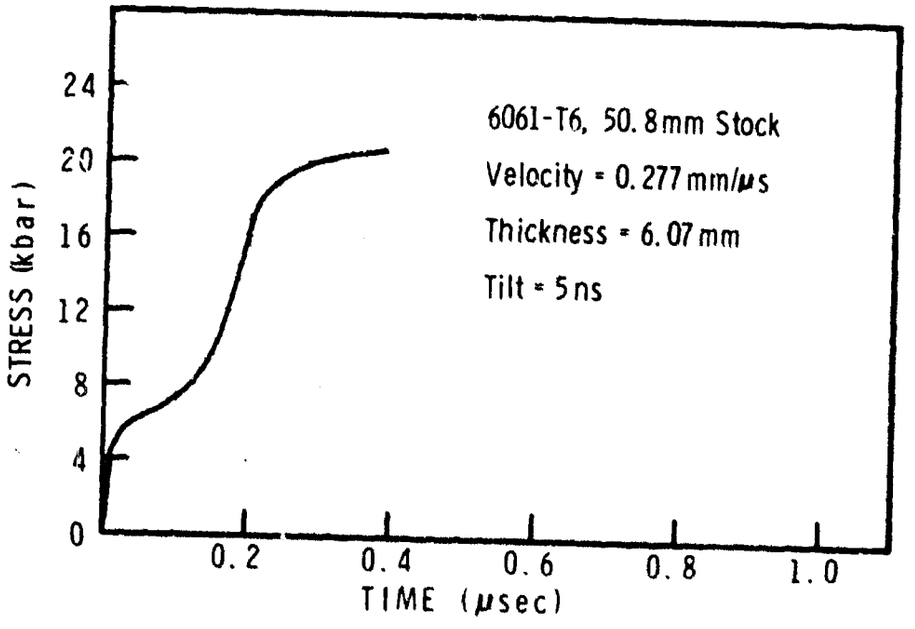
6061-T6, 50.8mm Stock
Velocity = 0.277 mm/μs
Thickness = 6.07 mm
Tilt = 5 ns
STRESS (kbar)
0
4
8
12
16
20
24
0.2
0.4
0.6
0.8
1.0
TIME (μsec)

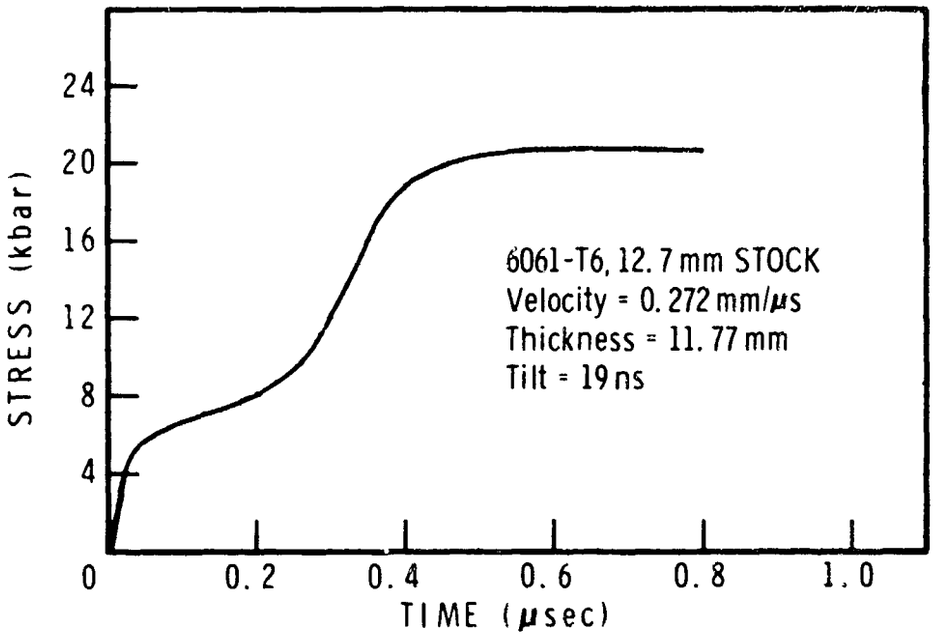
STRESS (kbar)
24
20
16
12
8
4
0
0.2
0.4
0.6
0.8
1.0
TIME (μsec)
6061-T6, 12.7 mm STOCK
Velocity = 0.272 mm/μs
Thickness = 11.77 mm
Tilt = 19 ns

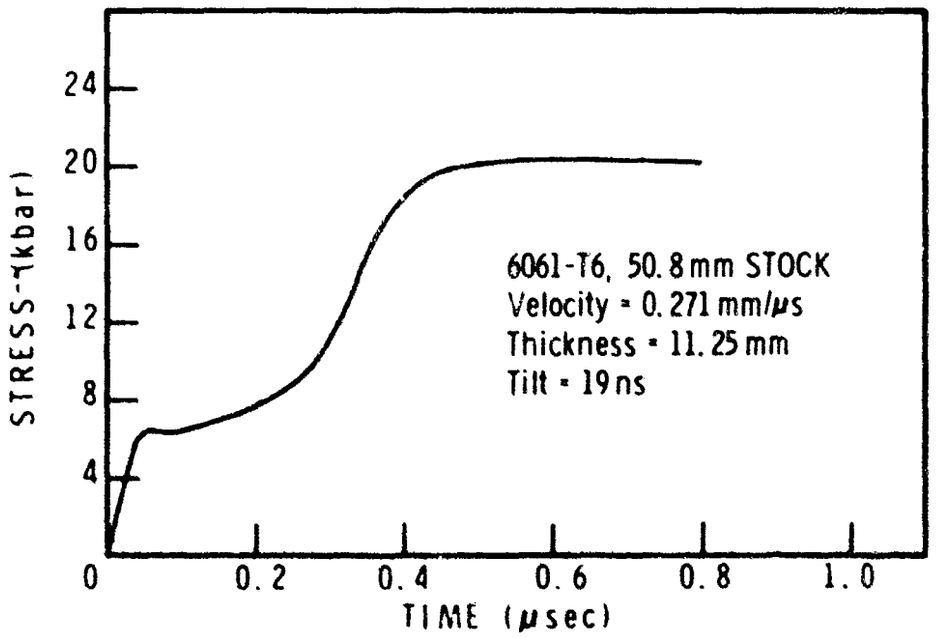
STRESS (kbar)
24
20
16
12
8
4
0
0.2
0.4
0.6
0.8
1.0
TIME (μsec)
6061-T6, 50.8 mm STOCK
Velocity = 0.271 mm/μs
Thickness = 11.25 mm
Tilt = 19 ns

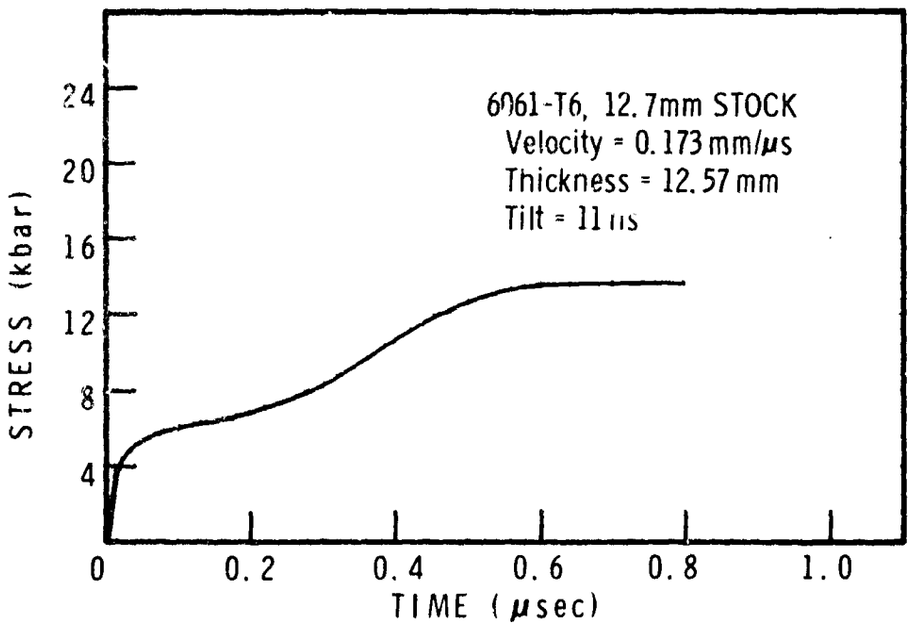
6061-T6, 12.7mm STOCK
Velocity = 0.173 mm/μs
Thickness = 12.57 mm
Tilt = 11 ns
STRESS (kbar)
24
20
16
12
8
4
0
0.2
0.4
0.6
0.8
1.0
TIME (μsec)

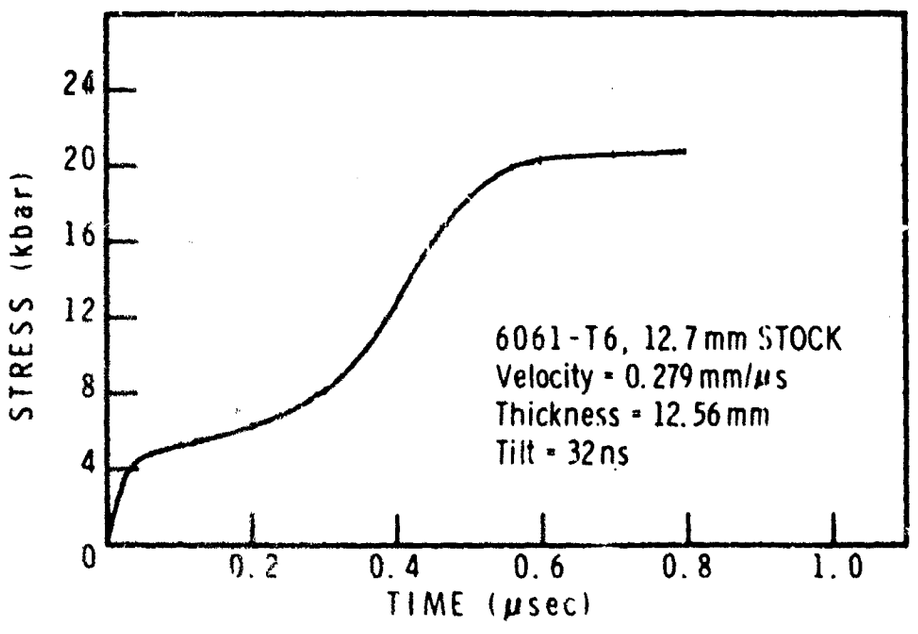
6061-T6, 12.7 mm STOCK
Velocity = 0.279 mm/μs
Thickness = 12.56 mm
Tilt = 32 ns
STRESS (kbar)
24
20
16
12
8
4
0
0.2
0.4
0.6
0.8
1.0
TIME (μsec)

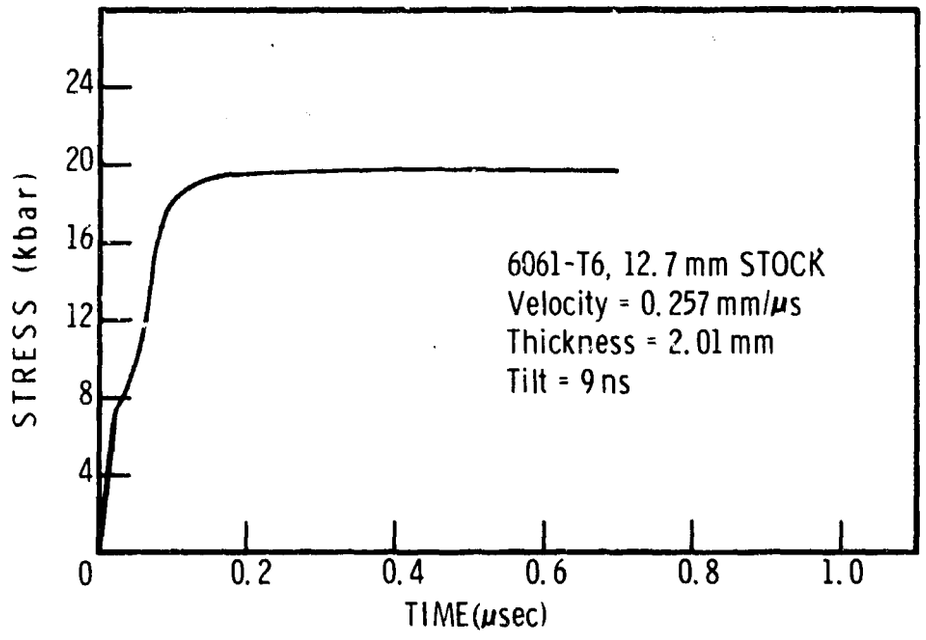
STRESS (kbar)
24
20
16
12
8
4
0
0.2
0.4
0.6
0.8
1.0
TIME(μsec)
6061-T6, 12.7 mm STOCK
Velocity = 0.257 mm/μs
Thickness = 2.01 mm
Tilt = 9 ns

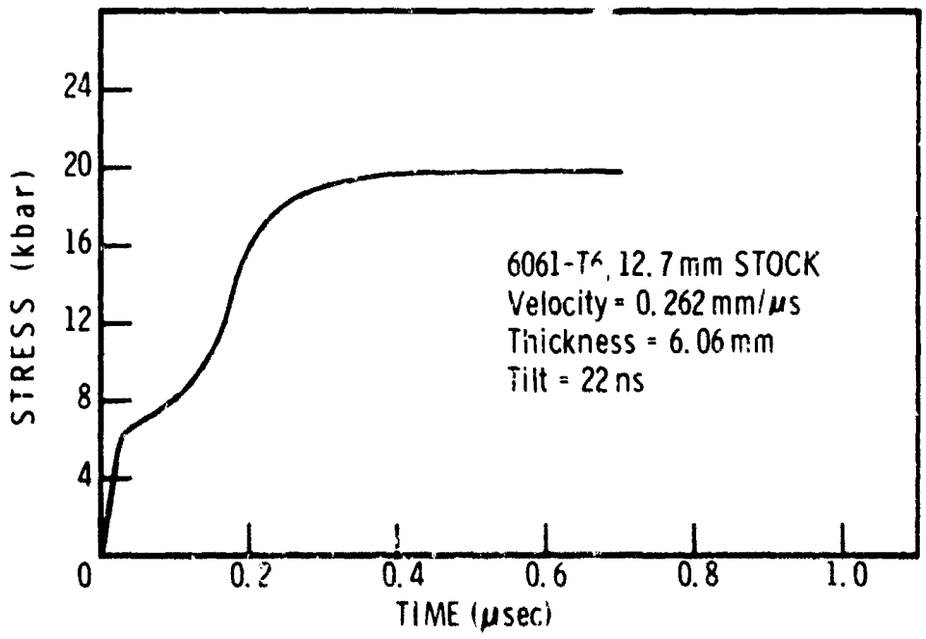
STRESS (kbar)
24
20
16
12
8
4
0
0.2
0.4
0.6
0.8
1.0
TIME (μsec)
6061-T6, 12.7 mm STOCK
Velocity = 0.262 mm/μs
Thickness = 6.06 mm
Tilt = 22 ns

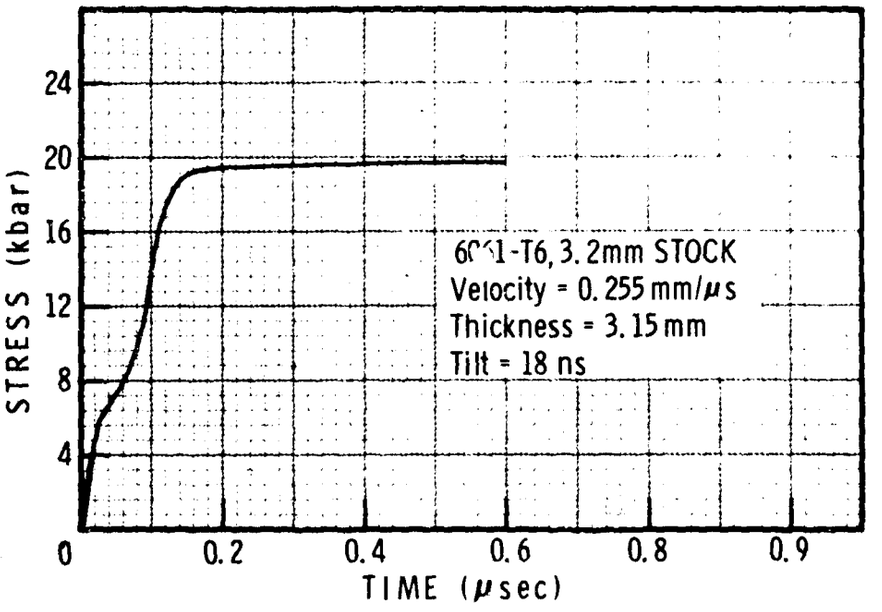
STRESS (kbar)
24
20
16
12
8
4
0
0.2
0.4
0.6
0.8
0.9
TIME (μsec)
6061-T6, 3.2mm STOCK
Velocity = 0.255 mm/μs
Thickness = 3.15 mm
Tilt = 18 ns

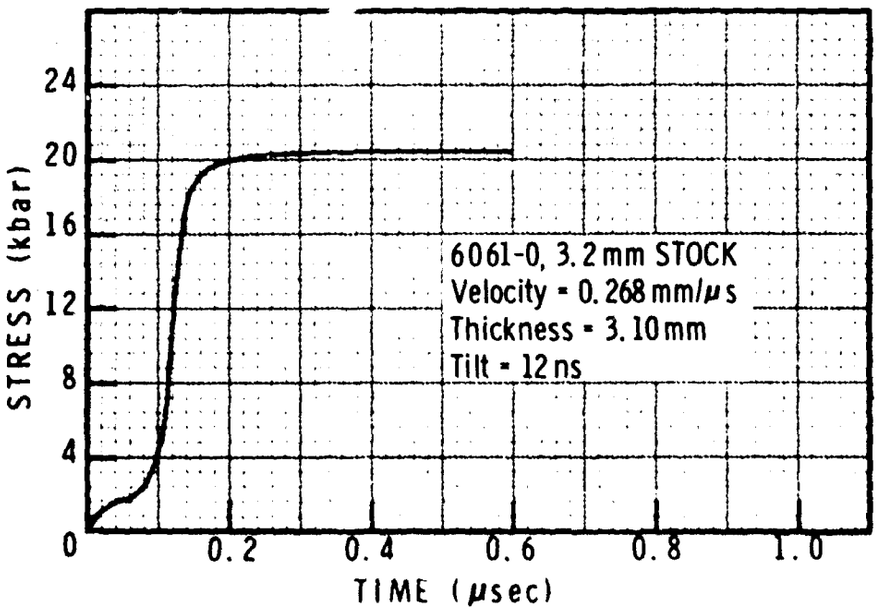
STRESS (kbar)
24
20
16
12
8
4
0
0.2
0.4
0.6
0.8
1.0
TIME (μsec)
6061-0, 3.2 mm STOCK
Velocity = 0.268 mm/μs
Thickness = 3.10 mm
Tilt = 12 ns

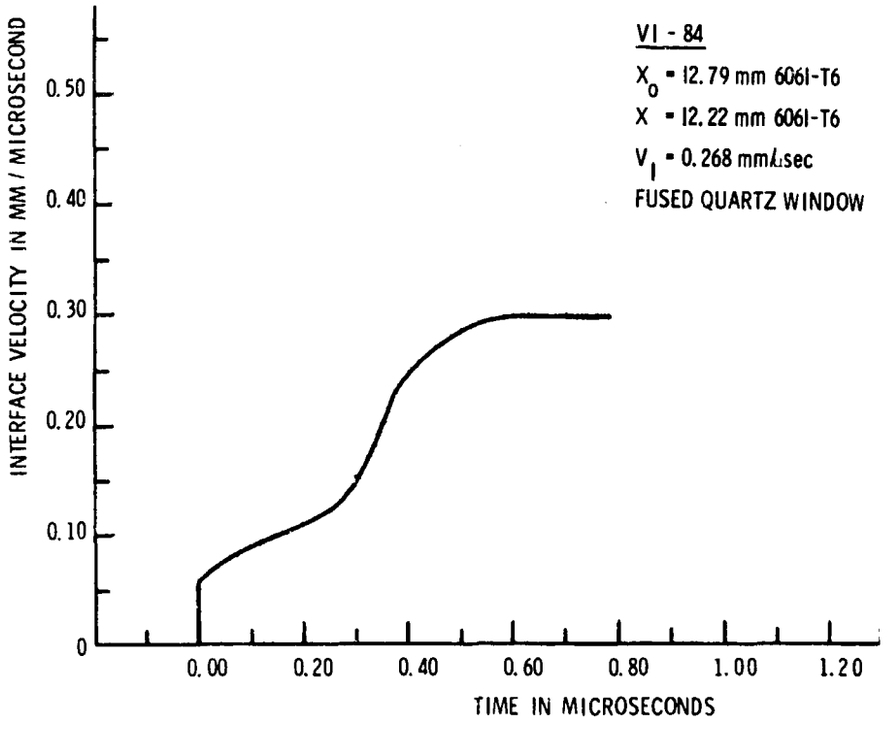
VI - 84
X_0 = 12.79 mm 6061-T6
X = 12.22 mm 6061-T6
V_I = 0.268 mm/μsec
FUSED QUARTZ WINDOW
INTERFACE VELOCITY IN MM / MICROSECOND
0.50
0.40
0.30
0.20
0.10
0
0.00
0.20
0.40
0.60
0.80
1.00
1.20
TIME IN MICROSECONDS

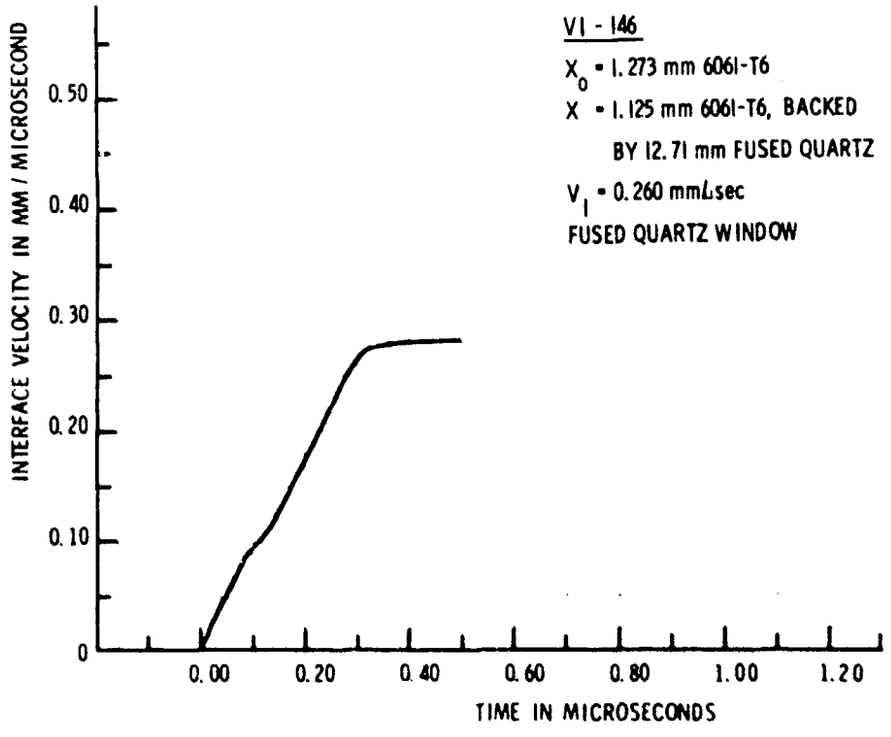
VI - 146
X_0 = 1.273 mm 6061-T6
X = 1.125 mm 6061-T6, BACKED
BY 12.71 mm FUSED QUARTZ
V_I = 0.260 mm/μsec
FUSED QUARTZ WINDOW
INTERFACE VELOCITY IN MM / MICROSECOND
0.50
0.40
0.30
0.20
0.10
0
0.00
0.20
0.40
0.60
0.80
1.00
1.20
TIME IN MICROSECONDS

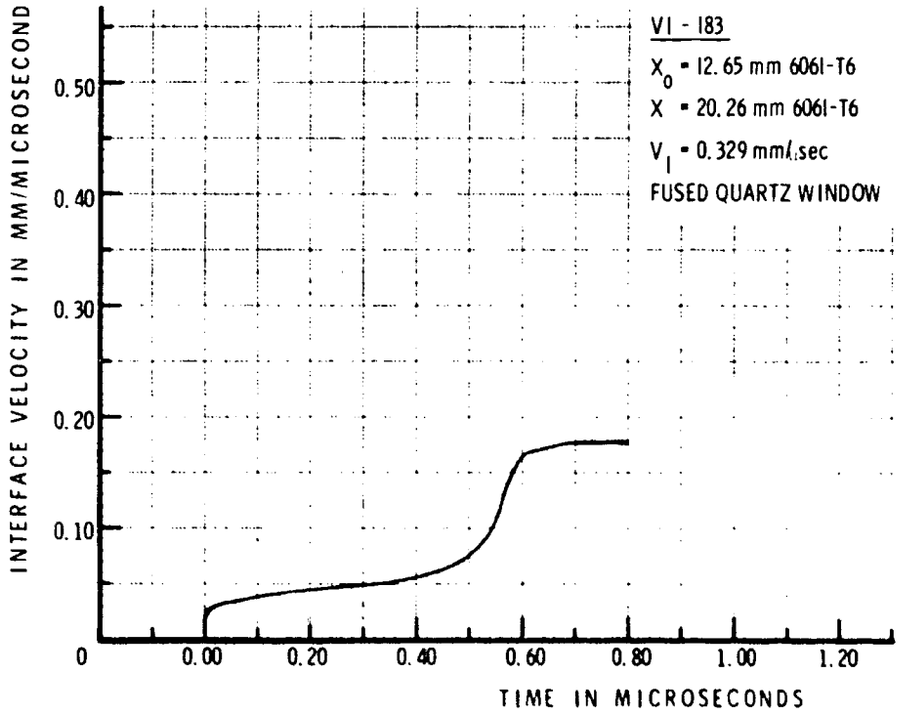
VI - 183
X_0 = 12.65 mm 6061-T6
X = 20.26 mm 6061-T6
V_I = 0.329 mm/sec
FUSED QUARTZ WINDOW
INTERFACE VELOCITY IN MM/MICROSECOND
0.50
0.40
0.30
0.20
0.10
0
0.00
0.20
0.40
0.60
0.80
1.00
1.20
TIME IN MICROSECONDS

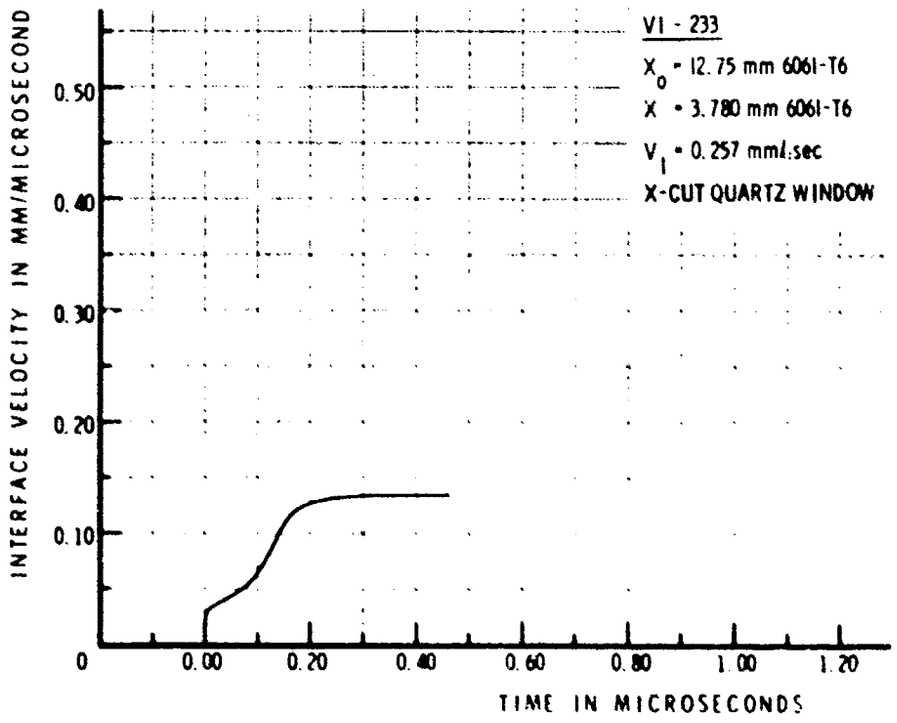
VI - 233
X_0 = 12.75 mm 6061-T6
X = 3.780 mm 6061-T6
V_I = 0.257 mm/sec
X-CUT QUARTZ WINDOW
INTERFACE VELOCITY IN MM/MICROSECOND
0.50
0.40
0.30
0.20
0.10
0
0.00
0.20
0.40
0.60
0.80
1.00
1.20
TIME IN MICROSECONDS

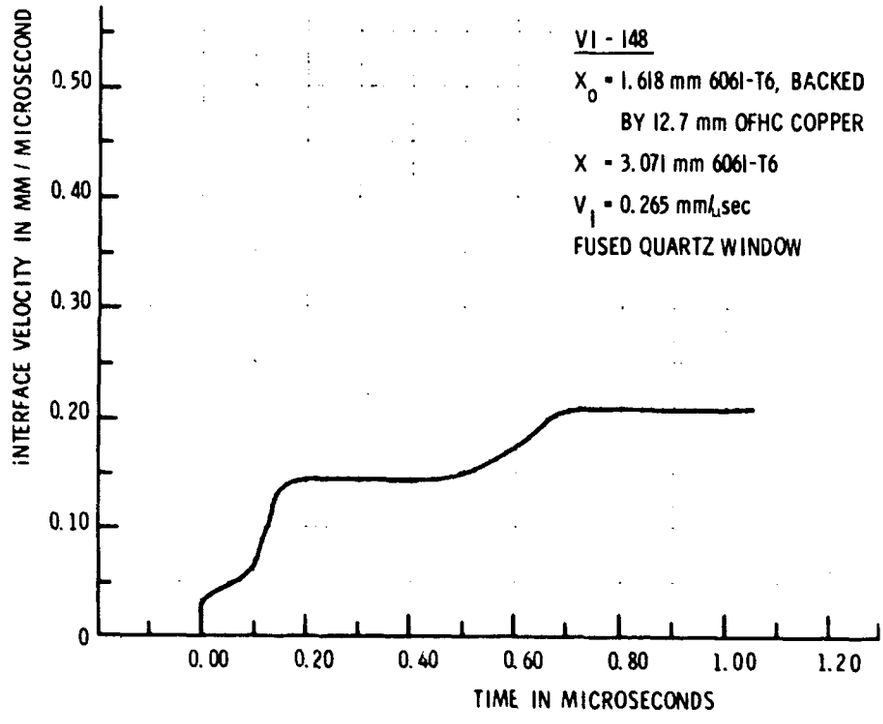
VI - 148
X_0 = 1.618 mm 6061-T6, BACKED BY 12.7 mm OFHC COPPER
X = 3.071 mm 6061-T6
V_I = 0.265 mm/μsec
FUSED QUARTZ WINDOW
INTERFACE VELOCITY IN MM / MICROSECOND
0.50
0.40
0.30
0.20
0.10
0
0.00
0.20
0.40
0.60
0.80
1.00
1.20
TIME IN MICROSECONDS

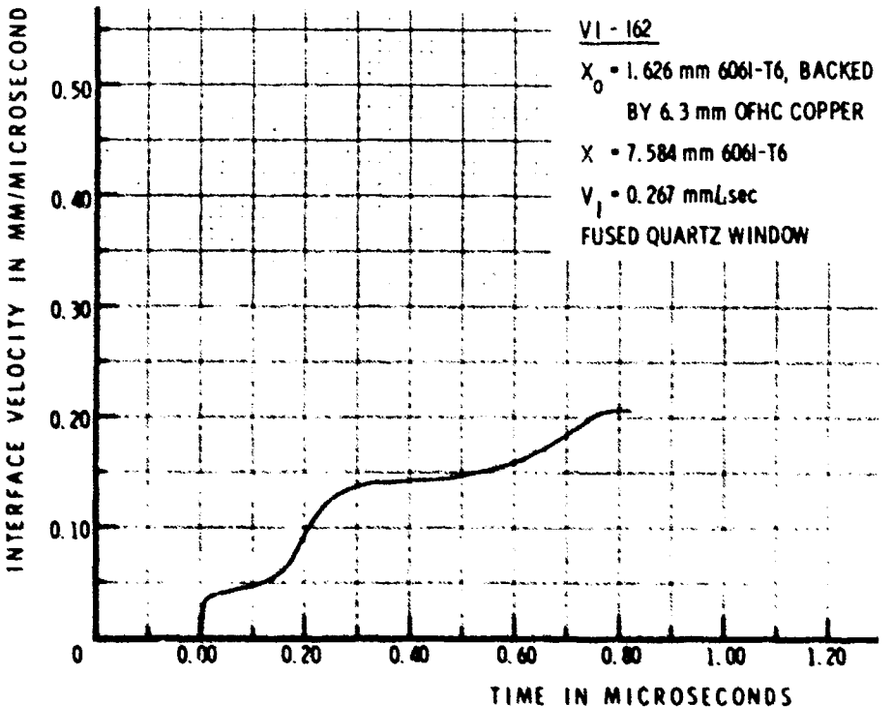
VI - 162
X_0 = 1.626 mm 6061-T6, BACKED BY 6.3 mm OFHC COPPER
X = 7.584 mm 6061-T6
V_I = 0.267 mm/μsec
FUSED QUARTZ WINDOW
INTERFACE VELOCITY IN MM/MICROSECOND
0.50
0.40
0.30
0.20
0.10
0
0.00
0.20
0.40
0.60
0.80
1.00
1.20
TIME IN MICROSECONDS

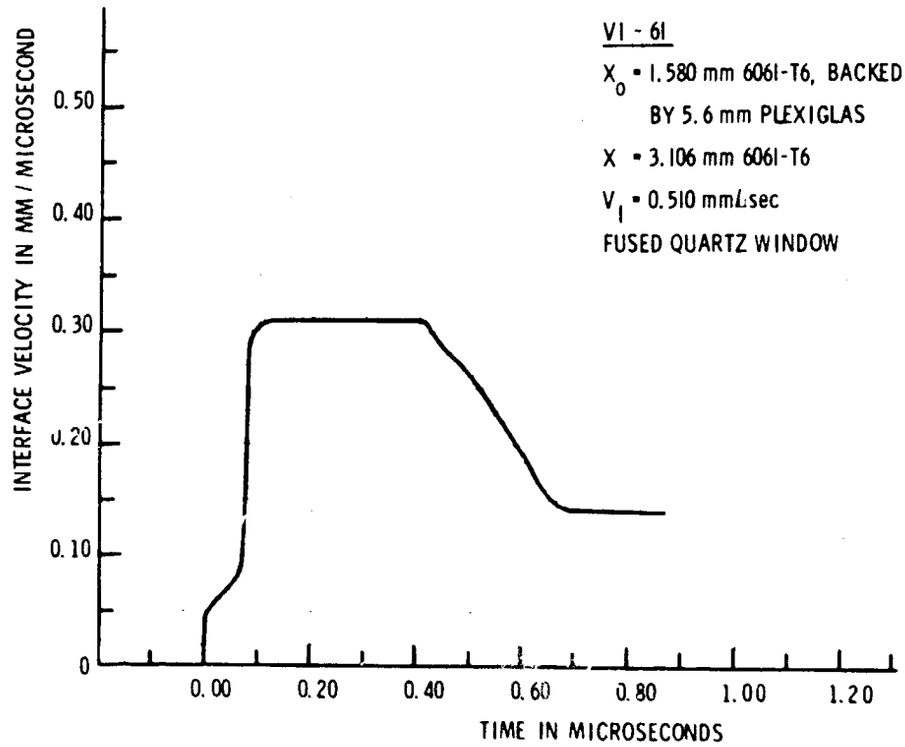
VI - 61
X_0 = 1.580 mm 6061-T6, BACKED BY 5.6 mm PLEXIGLAS
X = 3.106 mm 6061-T6
V_1 = 0.510 mm/μsec
FUSED QUARTZ WINDOW
INTERFACE VELOCITY IN MM / MICROSECOND
0.50
0.40
0.30
0.20
0.10
0
0.00
0.20
0.40
0.60
0.80
1.00
1.20
TIME IN MICROSECONDS

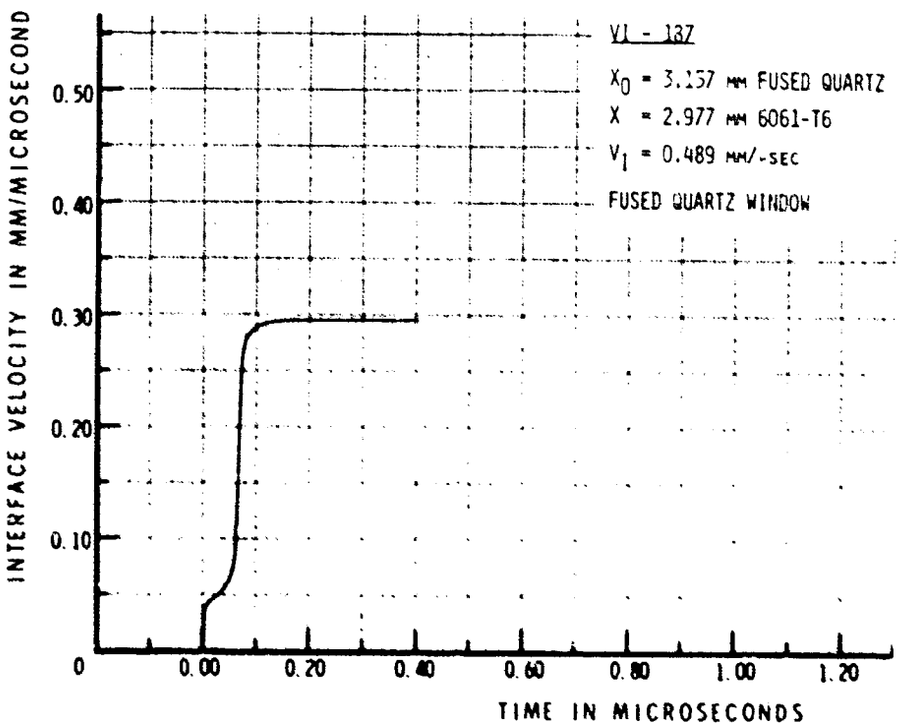
VI - 137
X_0 = 3.157 mm FUSED QUARTZ
X = 2.977 mm 6061-T6
V_1 = 0.489 mm/-sec
FUSED QUARTZ WINDOW
INTERFACE VELOCITY IN MM/MICROSECOND
0.50
0.40
0.30
0.20
0.10
0
0.00
0.20
0.40
0.60
0.80
1.00
1.20
TIME IN MICROSECONDS

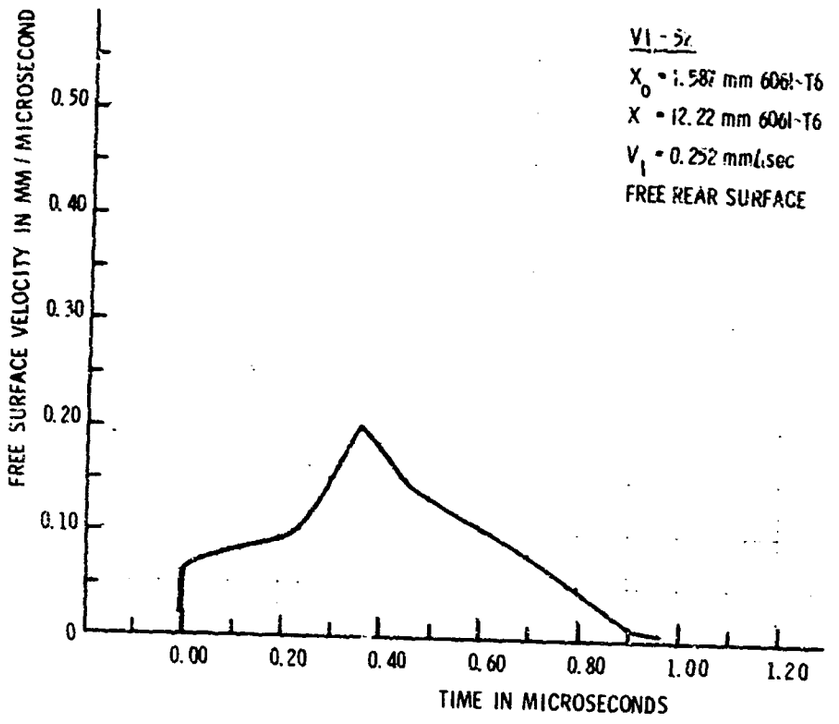
VI - 52
X_0 = 1.587 mm 6061-T6
X = 12.22 mm 6061-T6
V_1 = 0.252 mm/μsec
FREE REAR SURFACE
FREE SURFACE VELOCITY IN MM / MICROSECOND
0.50
0.40
0.30
0.20
0.10
0
0.00
0.20
0.40
0.60
0.80
1.00
1.20
TIME IN MICROSECONDS

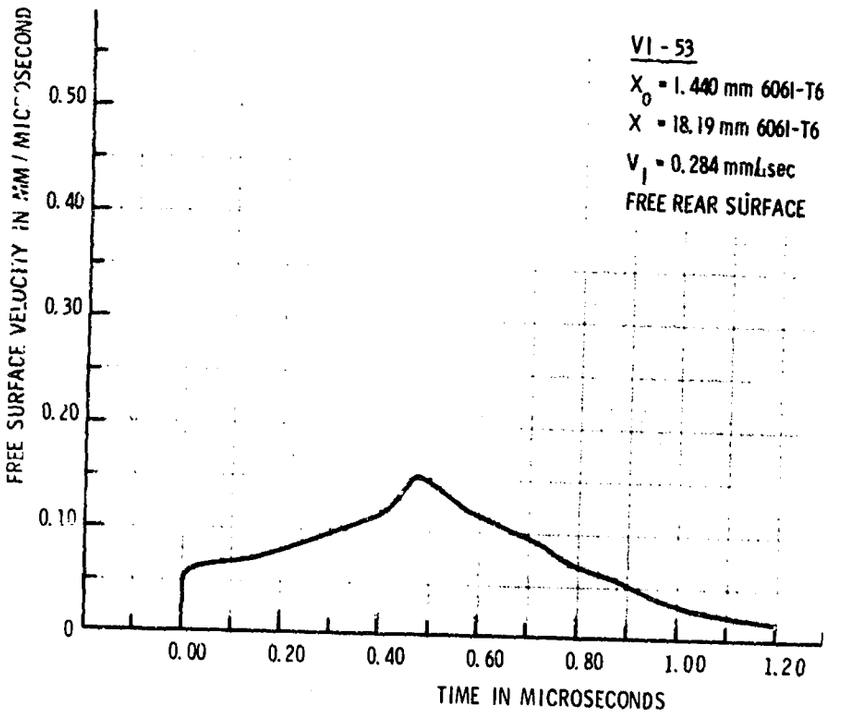
VI - 53
X_0 = 1.440 mm 6061-T6
X = 18.19 mm 6061-T6
V_1 = 0.284 mm/μsec
FREE REAR SURFACE
FREE SURFACE VELOCITY IN MM / MICROSECOND
0.50
0.40
0.30
0.20
0.10
0
0.00
0.20
0.40
0.60
0.80
1.00
1.20
TIME IN MICROSECONDS

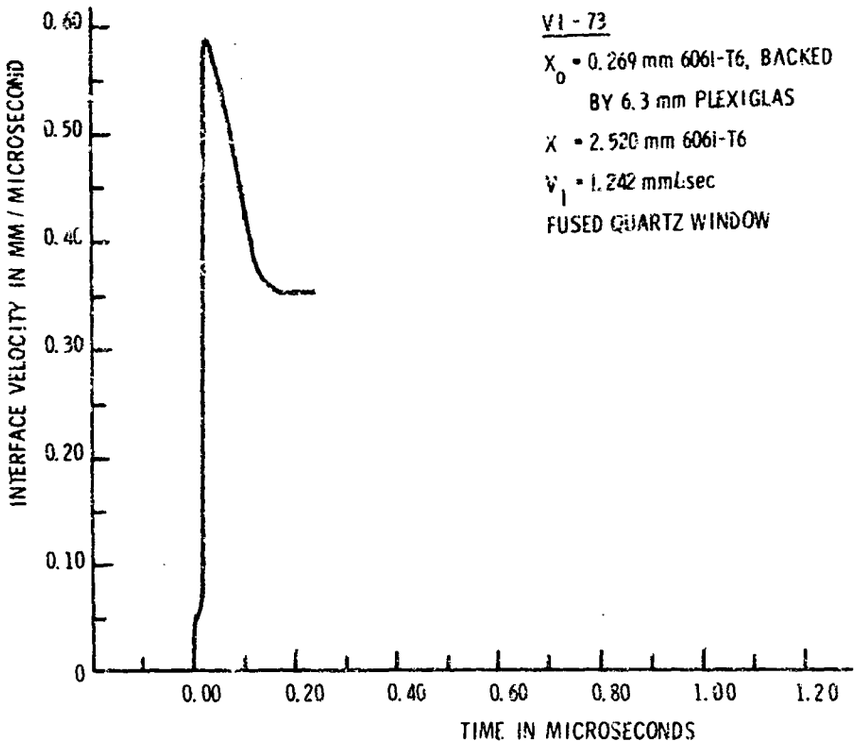
VI - 73
X_0 = 0.269 mm 6061-T6, BACKED BY 6.3 mm PLEXIGLAS
X = 2.520 mm 6061-T6
V_I = 1.242 mm/μsec
FUSED QUARTZ WINDOW
INTERFACE VELOCITY IN MM / MICROSECOND
0.60
0.50
0.40
0.30
0.20
0.10
0
0.00
0.20
0.40
0.60
0.80
1.00
1.20
TIME IN MICROSECONDS

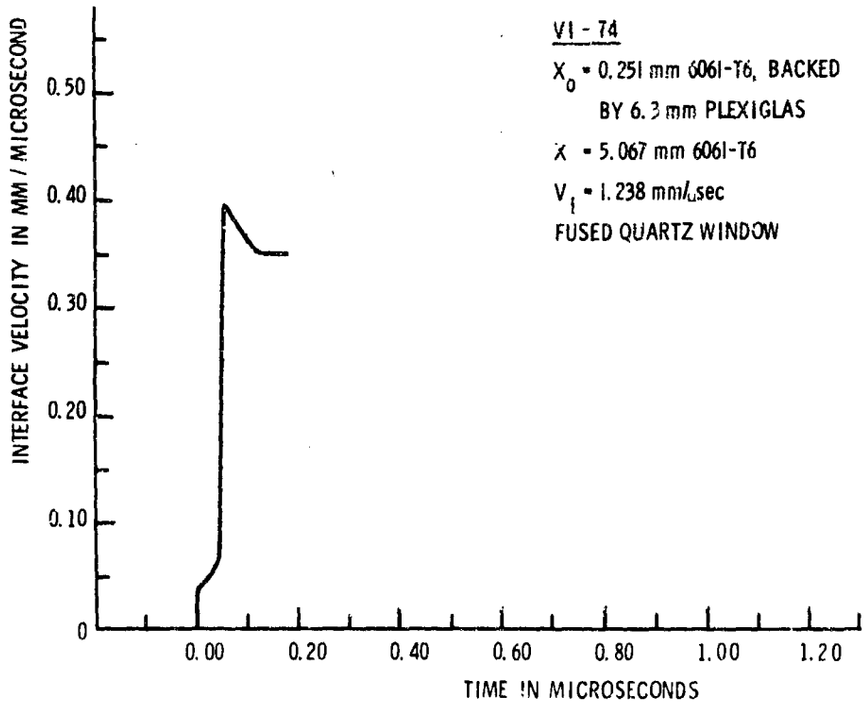
VI - 74
X_0 = 0.251 mm 6061-T6, BACKED BY 6.3 mm PLEXIGLAS
X = 5.067 mm 6061-T6
V_I = 1.238 mm/μsec
FUSED QUARTZ WINDOW
INTERFACE VELOCITY IN MM / MICROSECOND
0.50
0.40
0.30
0.20
0.10
0
0.00
0.20
0.40
0.60
0.80
1.00
1.20
TIME IN MICROSECONDS

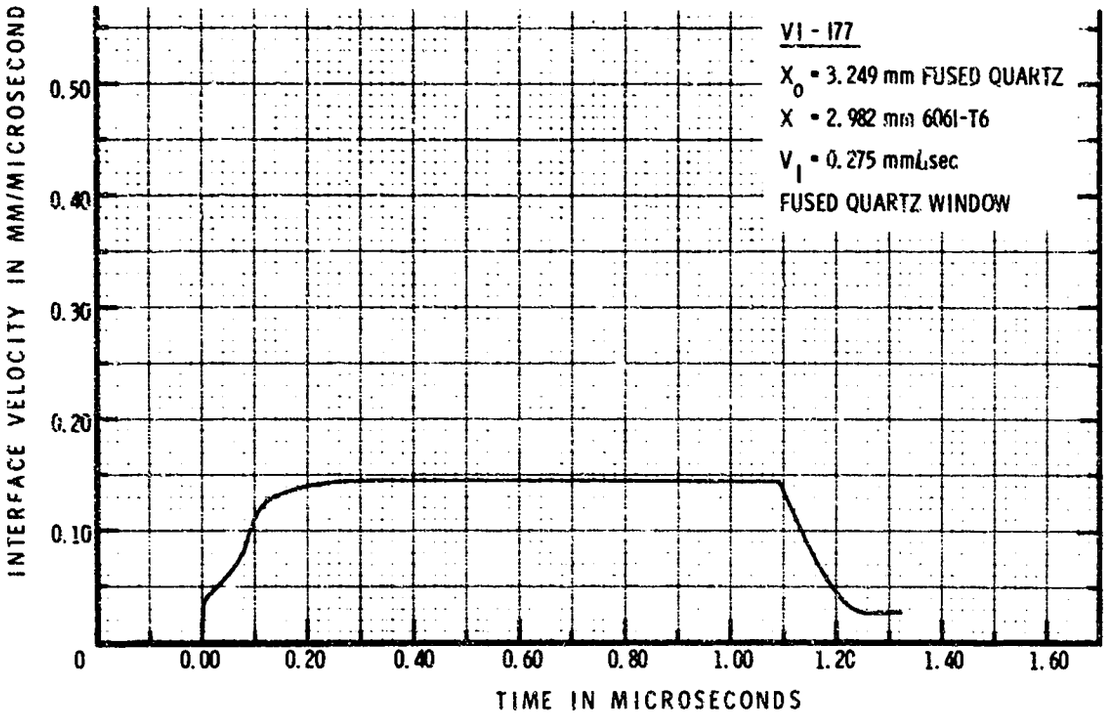
VI - 177
X_0 = 3.249 mm FUSED QUARTZ
X = 2.982 mm 6061-T6
V_I = 0.275 mm/μsec
FUSED QUARTZ WINDOW
INTERFACE VELOCITY IN MM/MICROSECOND
0.50
0.40
0.30
0.20
0.10
0
0.00
0.20
0.40
0.60
0.80
1.00
1.20
1.40
1.60
TIME IN MICROSECONDS

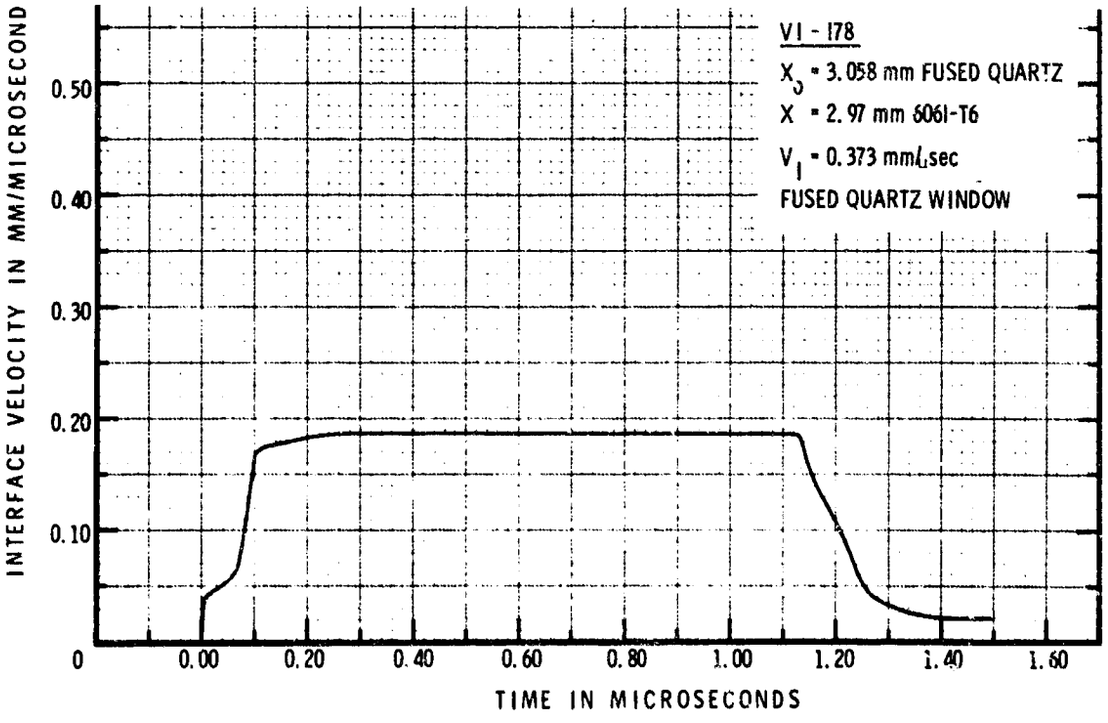
VI - 178
X_0 = 3.058 mm FUSED QUARTZ
X = 2.97 mm 6061-T6
V_I = 0.373 mm/μsec
FUSED QUARTZ WINDOW
INTERFACE VELOCITY IN MM/MICROSECOND
0.50
0.40
0.30
0.20
0.10
0
0.00
0.20
0.40
0.60
0.80
1.00
1.20
1.40
1.60
TIME IN MICROSECONDS

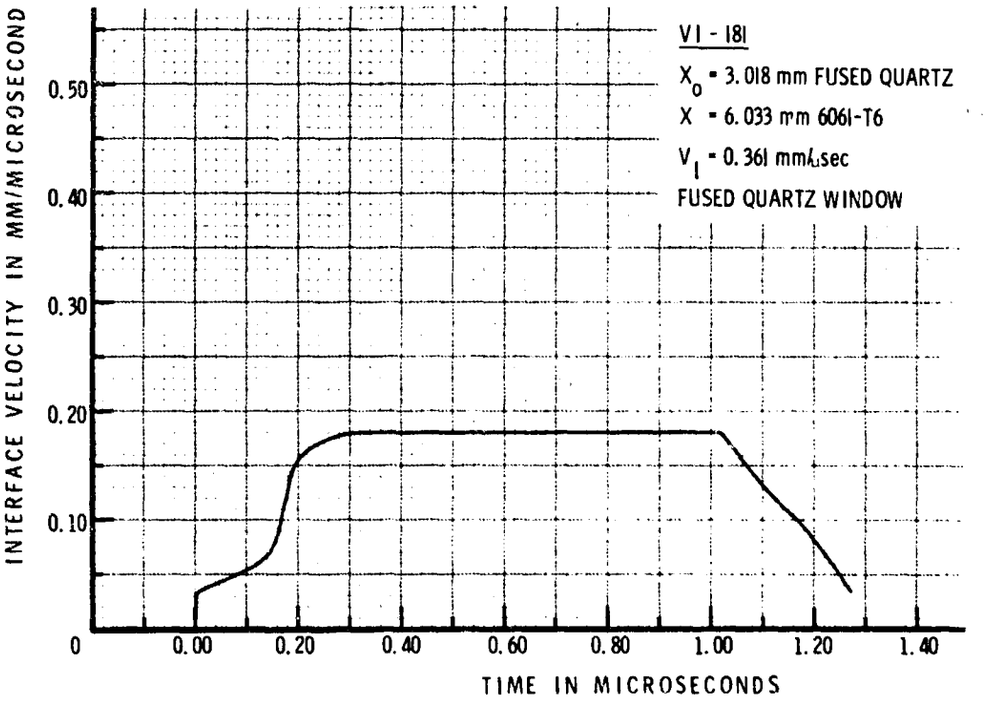
VI - 181
X_0 = 3.018 mm FUSED QUARTZ
X = 6.033 mm 6061-T6
V_I = 0.361 mm/μsec
FUSED QUARTZ WINDOW
INTERFACE VELOCITY IN MM/MICROSECOND
0.50
0.40
0.30
0.20
0.10
0
0.00
0.20
0.40
0.60
0.80
1.00
1.20
1.40
TIME IN MICROSECONDS

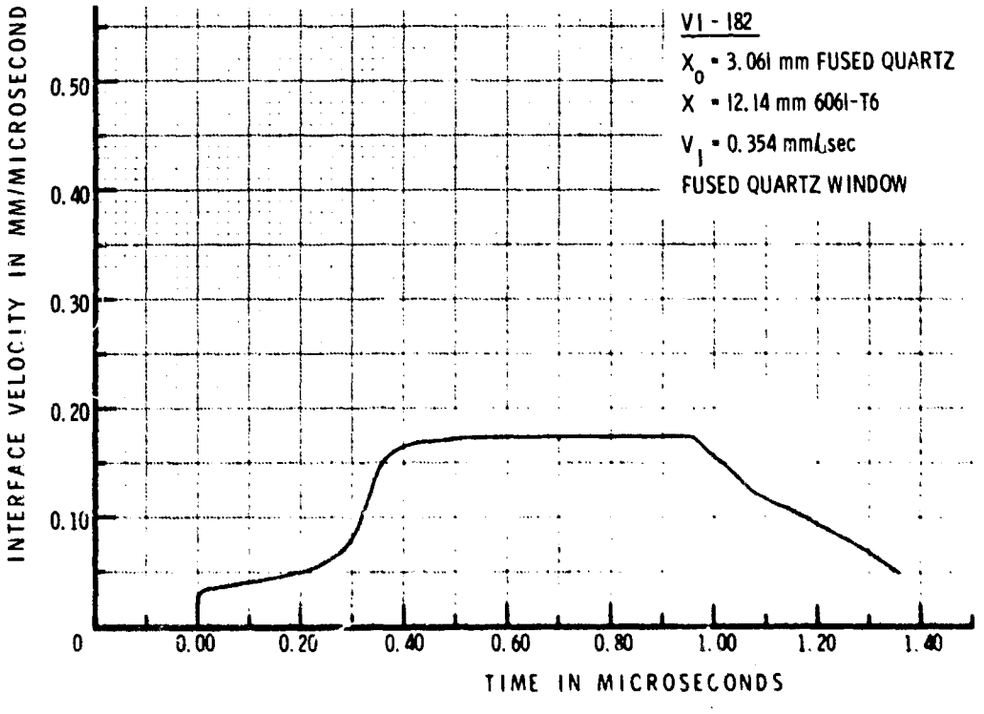
VI - 182
X_0 = 3.061 mm FUSED QUARTZ
X = 12.14 mm 6061-T6
V_I = 0.354 mm/μsec
FUSED QUARTZ WINDOW
INTERFACE VELOCITY IN MM/MICROSECOND
0.50
0.40
0.30
0.20
0.10
0
0.00
0.20
0.40
0.60
0.80
1.00
1.20
1.40
TIME IN MICROSECONDS

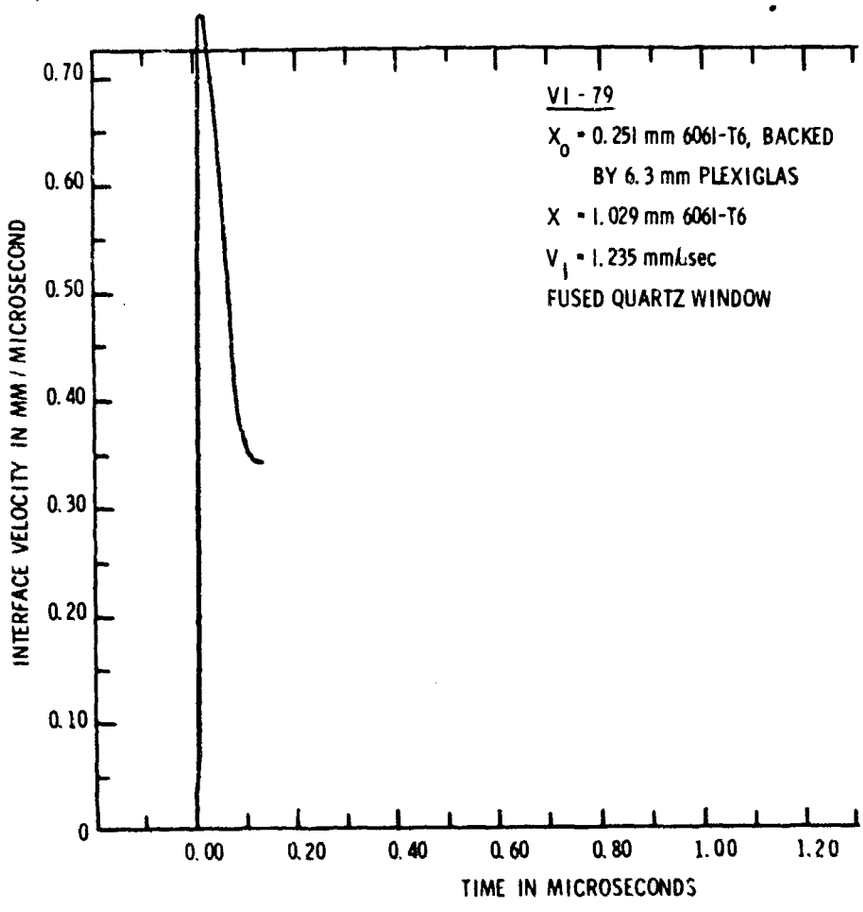
VI - 79
X_0 = 0.251 mm 6061-T6, BACKED BY 6.3 mm PLEXIGLAS
X = 1.029 mm 6061-T6
V_I = 1.235 mm/μsec
FUSED QUARTZ WINDOW
INTERFACE VELOCITY IN MM / MICROSECOND
0.70
0.60
0.50
0.40
0.30
0.20
0.10
0
0.00
0.20
0.40
0.60
0.80
1.00
1.20
TIME IN MICROSECONDS

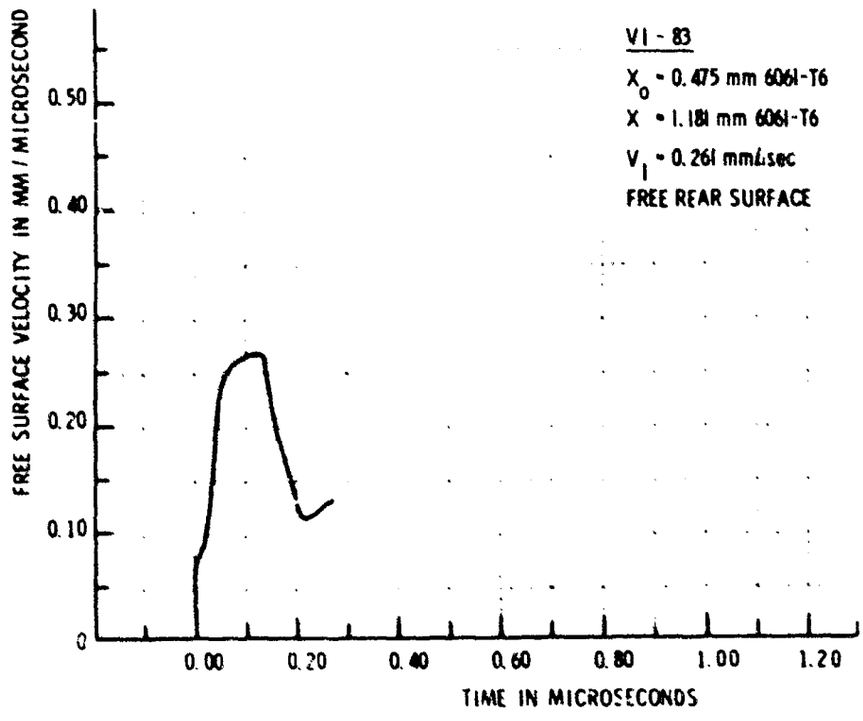
VI - 83
X_0 = 0.475 mm 6061-T6
X = 1.181 mm 6061-T6
V_I = 0.261 mm/μsec
FREE REAR SURFACE
FREE SURFACE VELOCITY IN MM / MICROSECOND
0.50
0.40
0.30
0.20
0.10
0
0.00
0.20
0.40
0.60
0.80
1.00
1.20
TIME IN MICROSECONDS

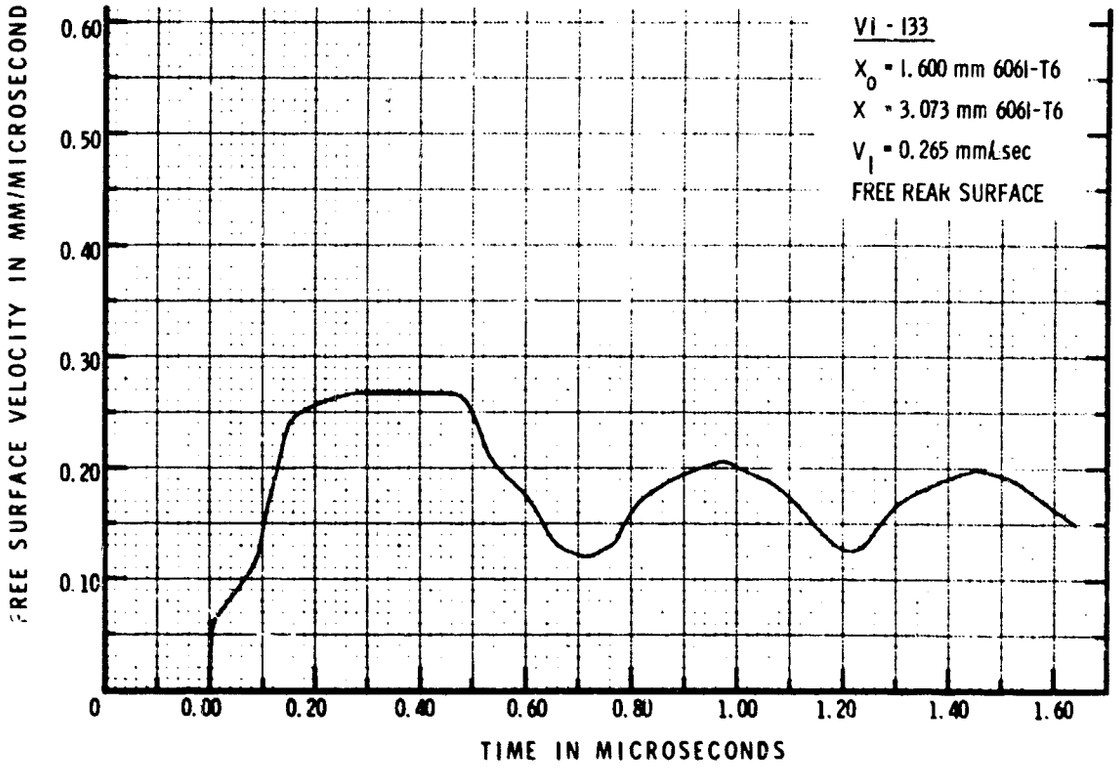
VI - 133
X_0 = 1.600 mm 6061-T6
X = 3.073 mm 6061-T6
V_1 = 0.265 mm/μsec
FREE REAR SURFACE
FREE SURFACE VELOCITY IN MM/MICROSECOND
0.60
0.50
0.40
0.30
0.20
0.10
0
0.00
0.20
0.40
0.60
0.80
1.00
1.20
1.40
1.60
TIME IN MICROSECONDS

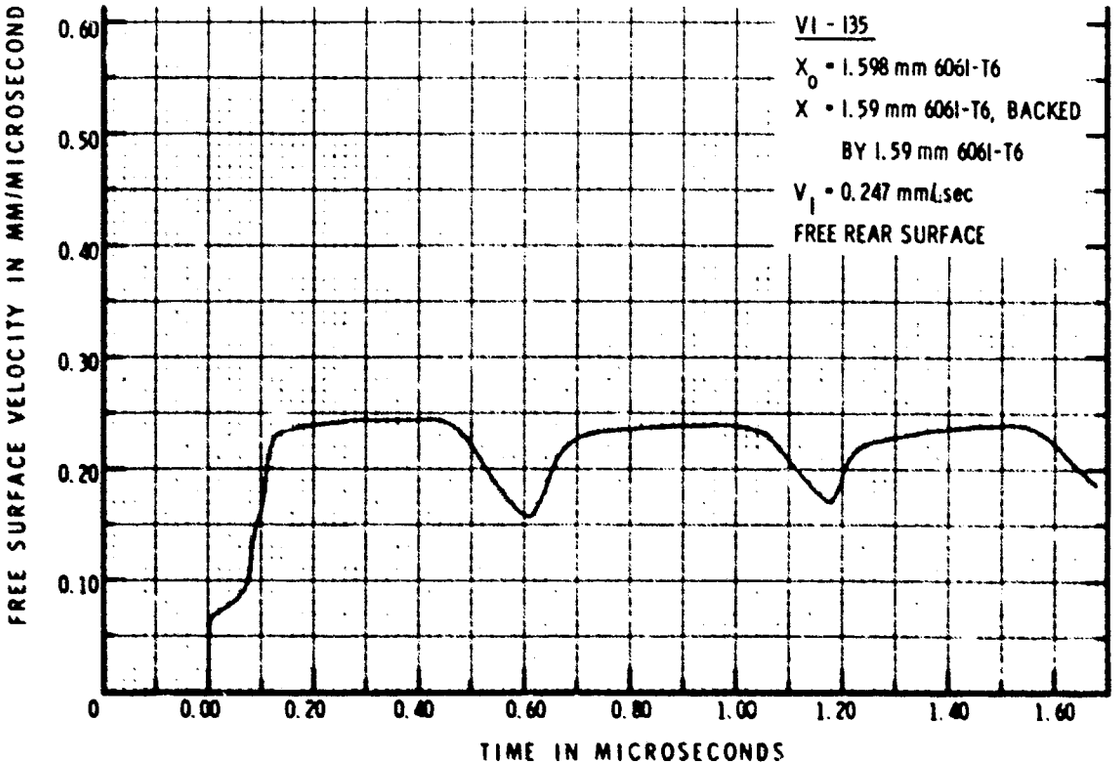
VI - 135
X_0 = 1.598 mm 6061-T6
X = 1.59 mm 6061-T6, BACKED BY 1.59 mm 6061-T6
V_1 = 0.247 mm/μsec
FREE REAR SURFACE
FREE SURFACE VELOCITY IN MM/MICROSECOND
0.60
0.50
0.40
0.30
0.20
0.10
0
0.00
0.20
0.40
0.60
0.80
1.00
1.20
1.40
1.60
TIME IN MICROSECONDS

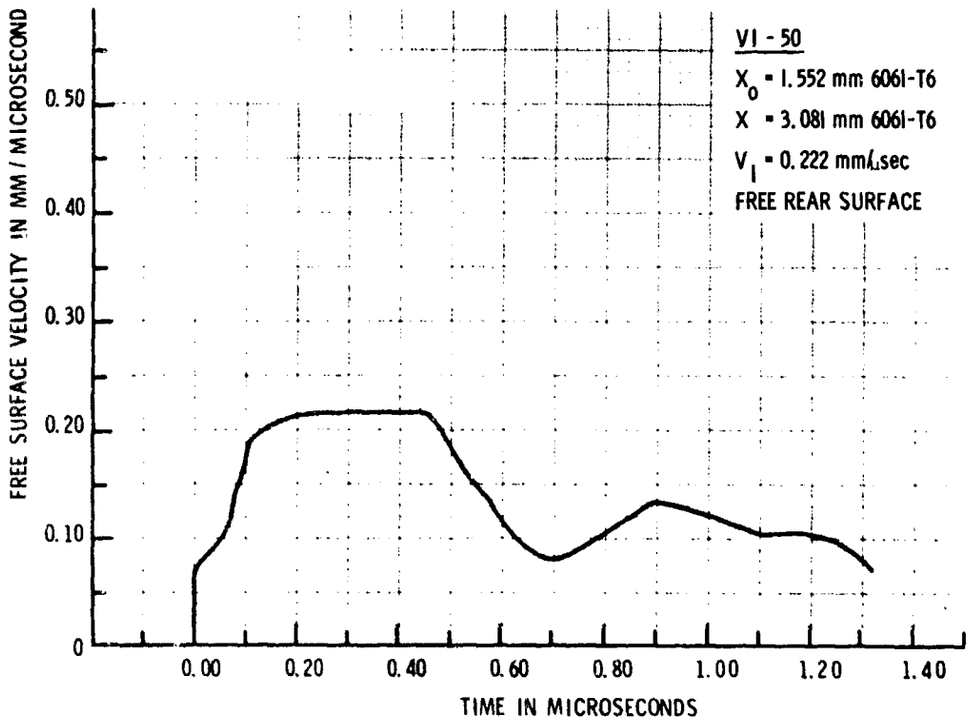
VI - 50
X_0 = 1.552 mm 6061-T6
X = 3.081 mm 6061-T6
V_I = 0.222 mm/μsec
FREE REAR SURFACE
FREE SURFACE VELOCITY IN MM / MICROSECOND
0.50
0.40
0.30
0.20
0.10
0
0.00
0.20
0.40
0.60
0.80
1.00
1.20
1.40
TIME IN MICROSECONDS

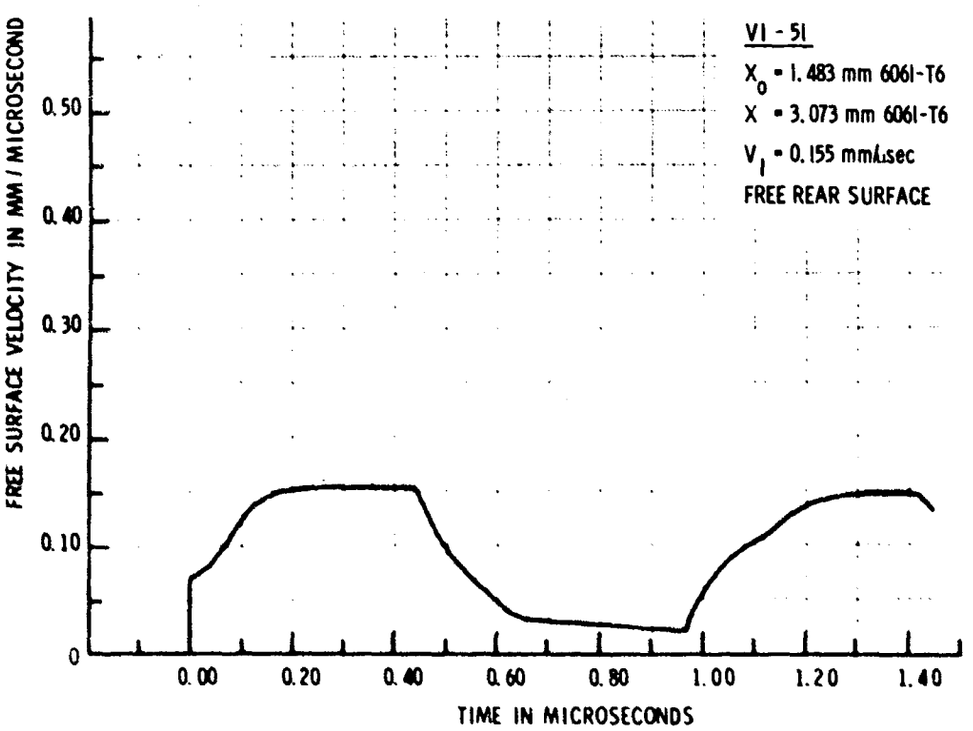
VI - 51
X_0 = 1.483 mm 6061-T6
X = 3.073 mm 6061-T6
V_I = 0.155 mm/μsec
FREE REAR SURFACE
FREE SURFACE VELOCITY IN MM / MICROSECOND
0.50
0.40
0.30
0.20
0.10
0
0.00
0.20
0.40
0.60
0.80
1.00
1.20
1.40
TIME IN MICROSECONDS

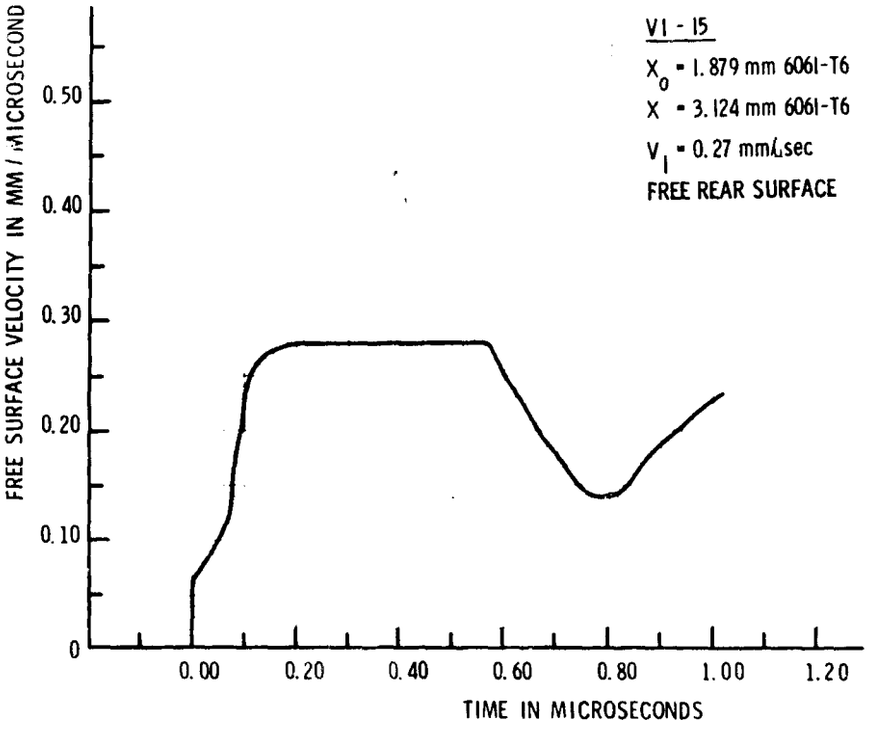
VI - 15
X_0 = 1.879 mm 6061-T6
X = 3.124 mm 6061-T6
V_1 = 0.27 mm/μsec
FREE REAR SURFACE
FREE SURFACE VELOCITY IN MM / MICROSECOND
0.50
0.40
0.30
0.20
0.10
0
0.00
0.20
0.40
0.60
0.80
1.00
1.20
TIME IN MICROSECONDS

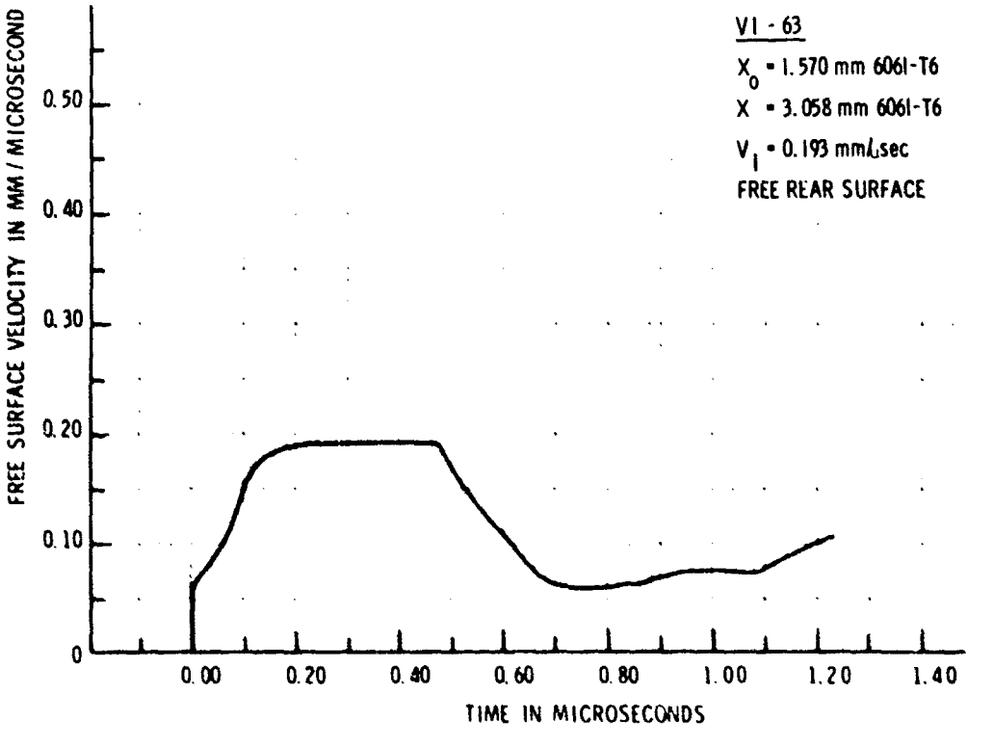
VI - 63
X_0 = 1.570 mm 6061-T6
X = 3.058 mm 6061-T6
V_1 = 0.193 mm/μsec
FREE REAR SURFACE
FREE SURFACE VELOCITY IN MM / MICROSECOND
0.50
0.40
0.30
0.20
0.10
0
0.00
0.20
0.40
0.60
0.80
1.00
1.20
1.40
TIME IN MICROSECONDS

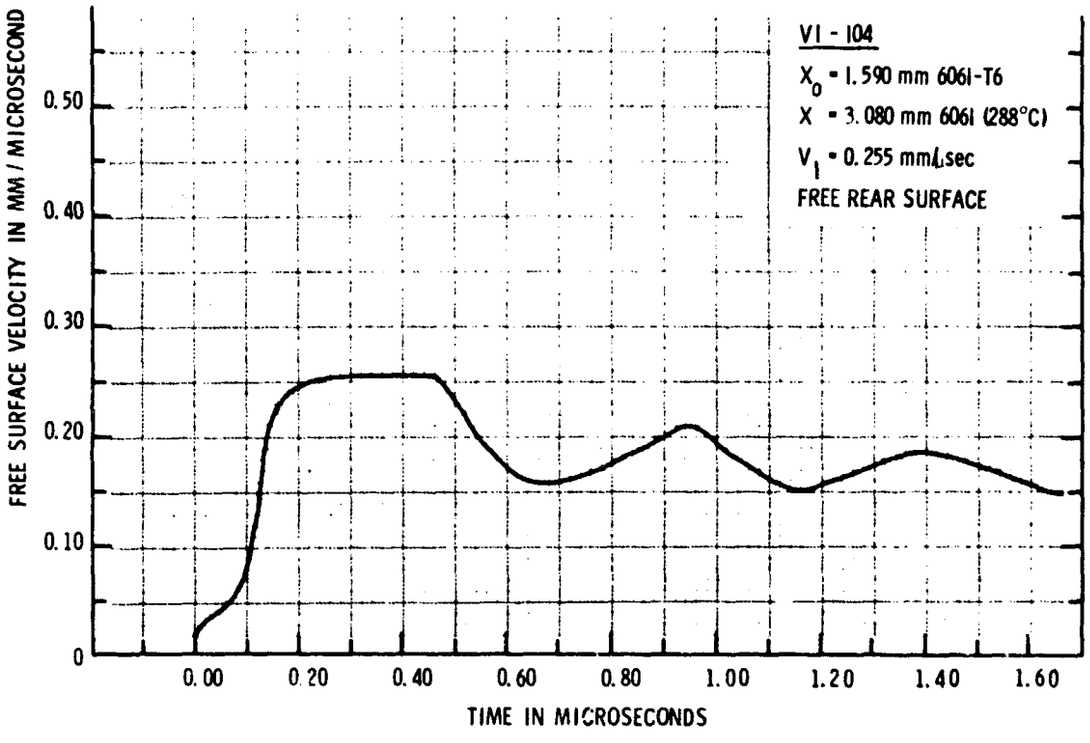
VI - 104
X_0 = 1.590 mm 6061-T6
X = 3.080 mm 6061 (288°C)
V_1 = 0.255 mm/μsec
FREE REAR SURFACE
FREE SURFACE VELOCITY IN MM / MICROSECOND
0.50
0.40
0.30
0.20
0.10
0
0.00
0.20
0.40
0.60
0.80
1.00
1.20
1.40
1.60
TIME IN MICROSECONDS

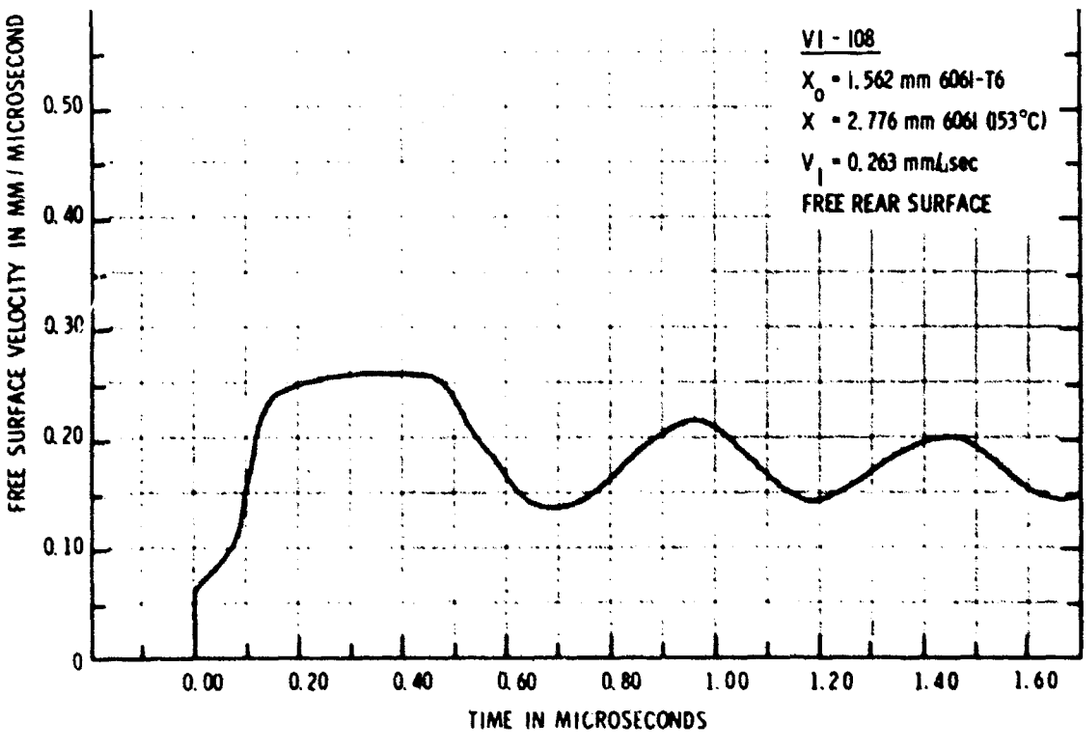
VI - 108
X_0 = 1.562 mm 6061-T6
X = 2.776 mm 6061 (153°C)
V_1 = 0.263 mm/μsec
FREE REAR SURFACE
FREE SURFACE VELOCITY IN MM / MICROSECOND
0.50
0.40
0.30
0.20
0.10
0
0.00
0.20
0.40
0.60
0.80
1.00
1.20
1.40
1.60
TIME IN MICROSECONDS

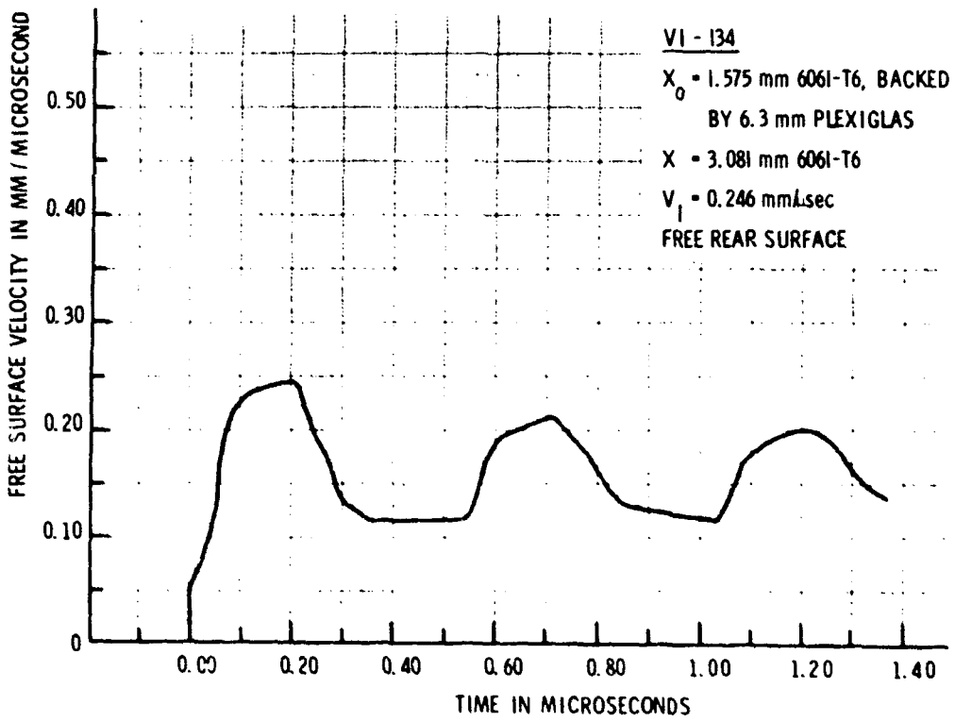
VI - 134
X_0 = 1.575 mm 6061-T6, BACKED BY 6.3 mm PLEXIGLAS
X = 3.081 mm 6061-T6
V_1 = 0.246 mm/μsec
FREE REAR SURFACE
FREE SURFACE VELOCITY IN MM / MICROSECOND
0.50
0.40
0.30
0.20
0.10
0
0.00
0.20
0.40
0.60
0.80
1.00
1.20
1.40
TIME IN MICROSECONDS

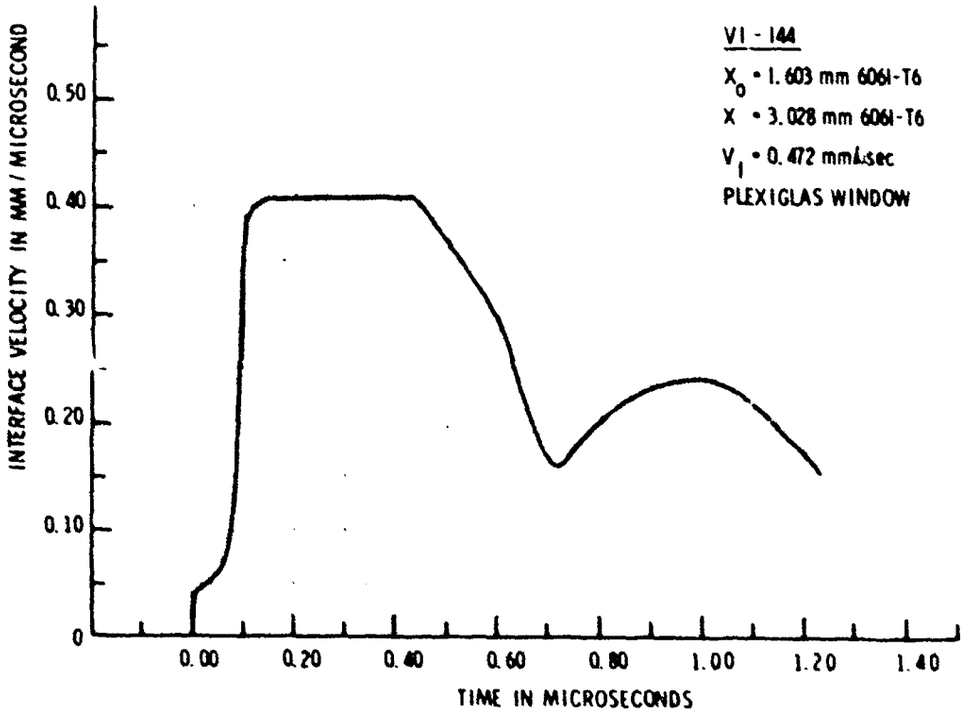
VI - 144
X_0 = 1.603 mm 6061-T6
X = 3.028 mm 6061-T6
V_1 = 0.472 mm/μsec
PLEXIGLAS WINDOW
INTERFACE VELOCITY IN MM / MICROSECOND
0.50
0.40
0.30
0.20
0.10
0
0.00
0.20
0.40
0.60
0.80
1.00
1.20
1.40
TIME IN MICROSECONDS

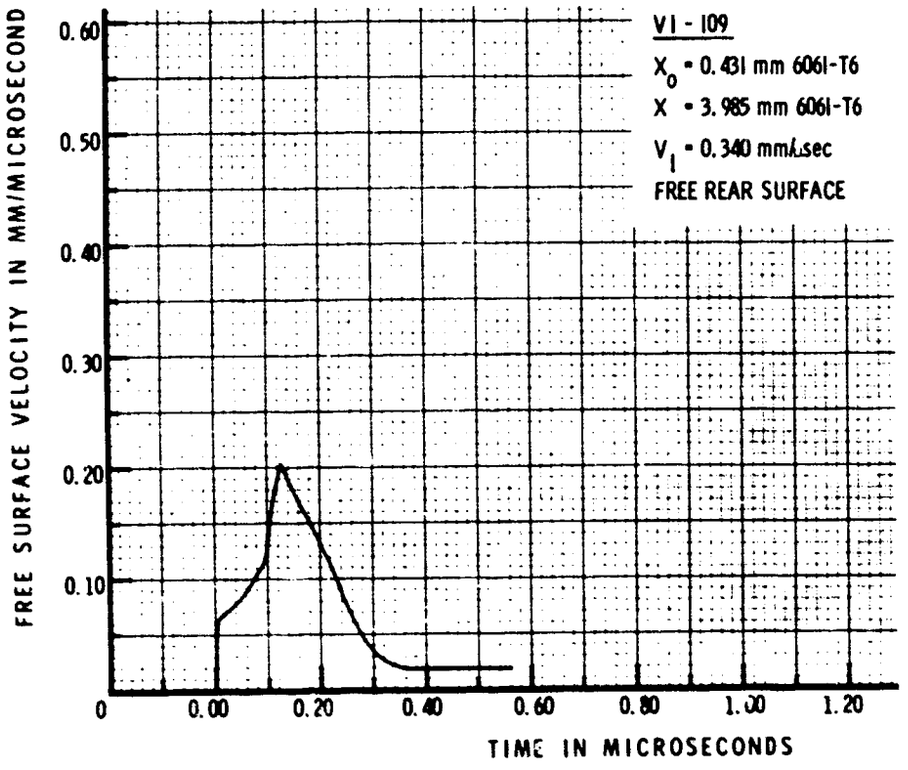
VI - 109
X_0 = 0.431 mm 6061-T6
X = 3.985 mm 6061-T6
V_1 = 0.340 mm/μsec
FREE REAR SURFACE
FREE SURFACE VELOCITY IN MM/MICROSECOND
0.60
0.50
0.40
0.30
0.20
0.10
0
0.00
0.20
0.40
0.60
0.80
1.00
1.20
TIME IN MICROSECONDS

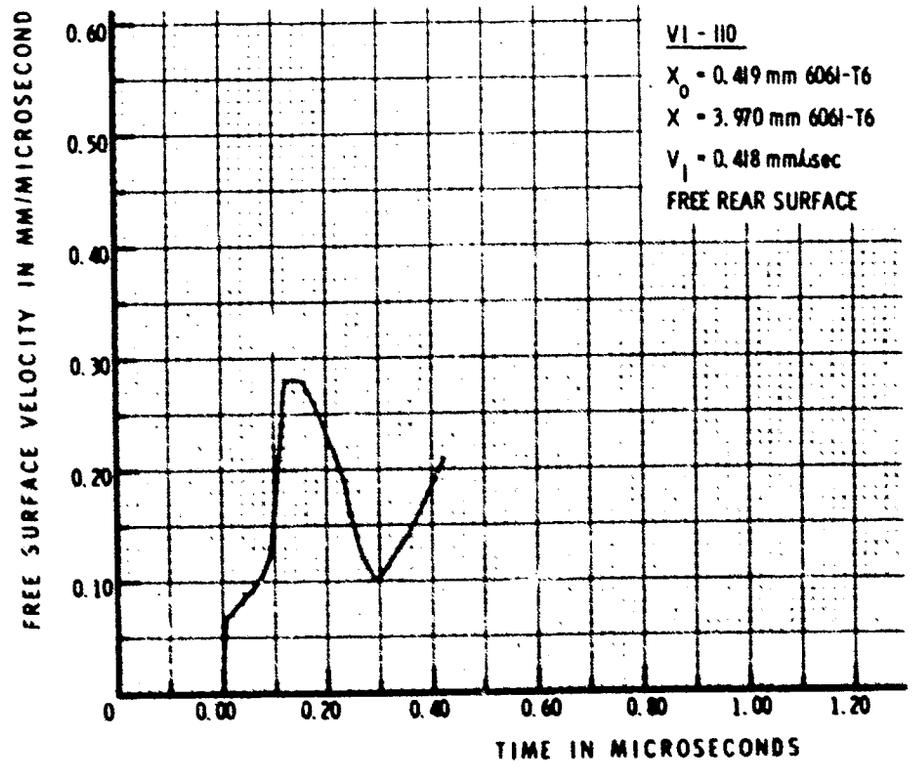
VI - 110
X_0 = 0.419 mm 6061-T6
X = 3.970 mm 6061-T6
V_1 = 0.418 mm/μsec
FREE REAR SURFACE
FREE SURFACE VELOCITY IN MM/MICROSECOND
0.60
0.50
0.40
0.30
0.20
0.10
0
0.00
0.20
0.40
0.60
0.80
1.00
1.20
TIME IN MICROSECONDS

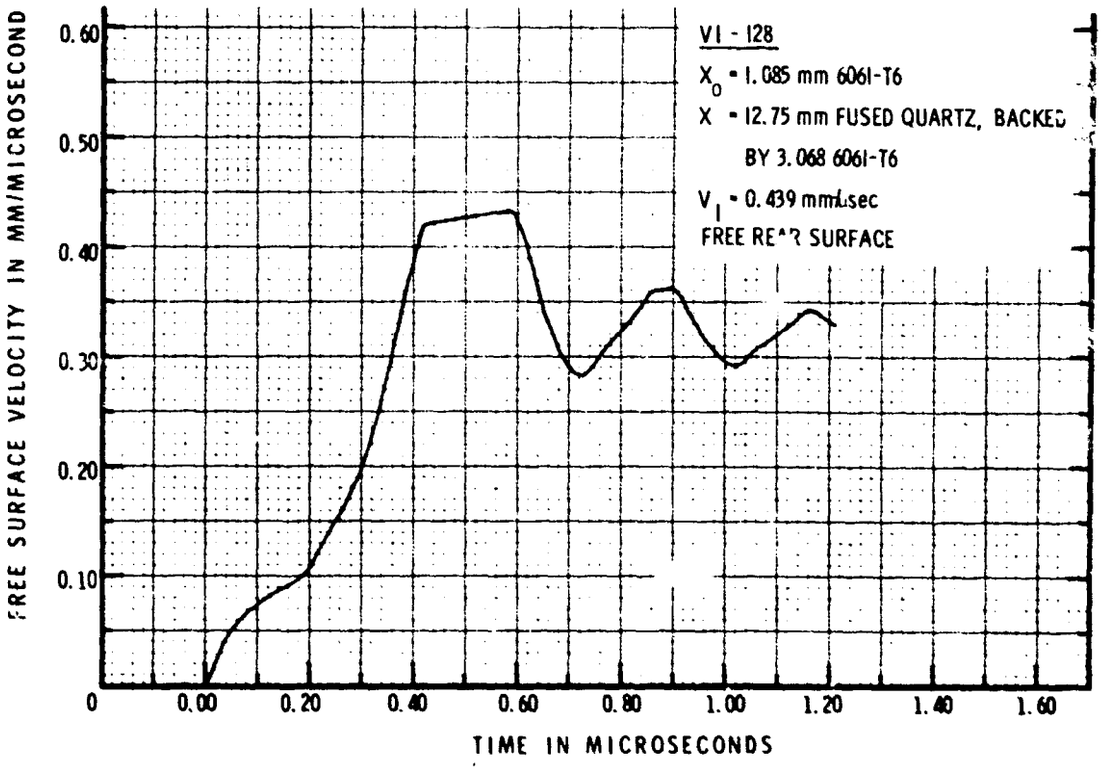
VI - 128
X_0 = 1.085 mm 6061-T6
X = 12.75 mm FUSED QUARTZ, BACKED BY 3.068 6061-T6
V_I = 0.439 mm/μsec
FREE REAR SURFACE
FREE SURFACE VELOCITY IN MM/MICROSECOND
0.60
0.50
0.40
0.30
0.20
0.10
0
0.00
0.20
0.40
0.60
0.80
1.00
1.20
1.40
1.60
TIME IN MICROSECONDS

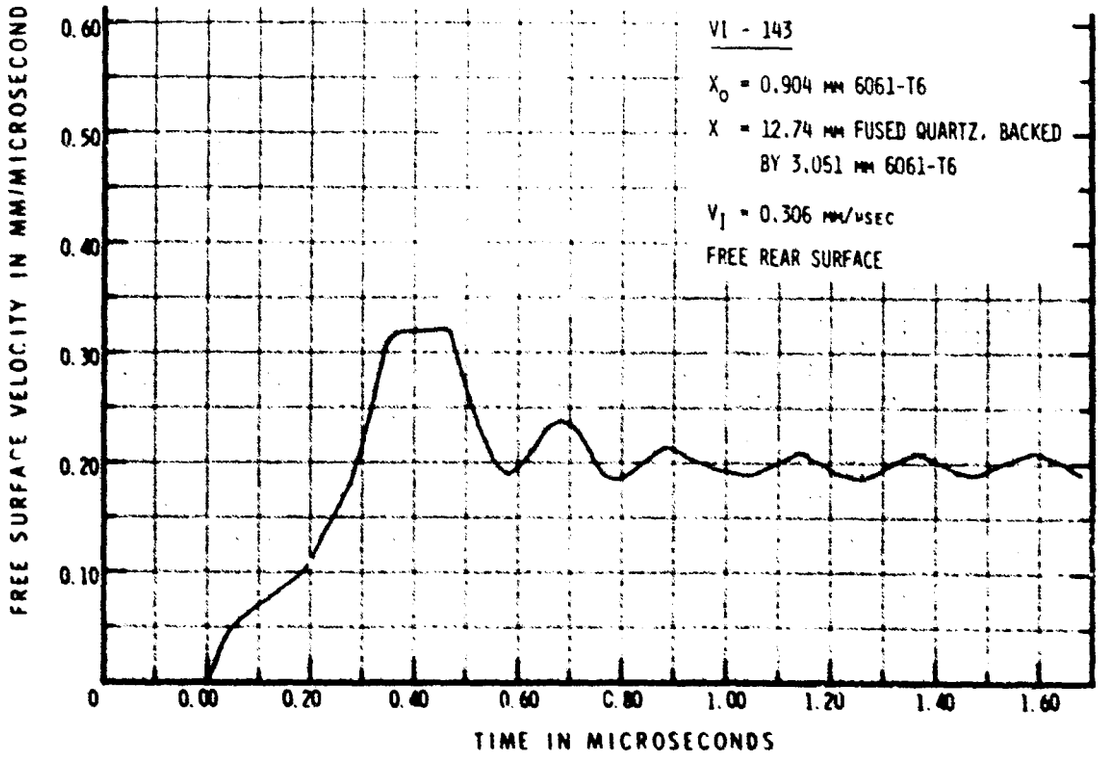
VI - 143
X_0 = 0.904 MM 6061-T6
X = 12.74 MM FUSED QUARTZ, BACKED BY 3.051 MM 6061-T6
V_I = 0.306 MM/μSEC
FREE REAR SURFACE
FREE SURFACE VELOCITY IN MM/MICROSECOND
0.60
0.50
0.40
0.30
0.20
0.10
0
0.00
0.20
0.40
0.60
0.80
1.00
1.20
1.40
1.60
TIME IN MICROSECONDS